ADVANCED SENSITIVITY ANALYSIS TECHNIQUES FOR ATMOSPHERIC CHEMISTRY MODELS: DEVELOPMENT AND APPLICATION

A Dissertation
Presented to
The Academic Faculty

by

Shannon L. Capps

In Partial Fulfillment
of the Requirements for the Degree
Doctor of Philosophy in the
School of Chemical & Biomolecular Engineering

Georgia Institute of Technology
December 2012

ADVANCED SENSITIVITY ANALYSIS TECHNIQUES FOR ATMOSPHERIC CHEMISTRY MODELS: DEVELOPMENT AND APPLICATION

Approved by:

Professor Athanasios Nenes, Advisor
School of Chemical & Biomolecular Engineering and School of Earth & Atmospheric Sciences
Georgia Institute of Technology

Professor Armistead G. Russell
School of Civil & Environmental Engineering
Georgia Institute of Technology

Professor Nga L. Ng
School of Chemical & Biomolecular Engineering and School of Earth & Atmospheric Sciences
Georgia Institute of Technology

Professor Yoshiaki Kawajiri
School of Chemical & Biomolecular Engineering
Georgia Institute of Technology

Professor Yuhang Wang
School of Earth & Atmospheric Sciences
Georgia Institute of Technology

Date Approved: 12 December 2012

Glory to God

Gratitude to many

including but not limited to...

my beloved parents who have always helped me ask the next question

for supporting this effort in more ways than could be told.

Greg Frost who first told me the story of atmospheric science and societal change

for continually helping me believe that I could be a small part of this plot.

Daven Henze who never refused to help guide me with making or using adjoints

for his inimitable yet contagious manner of delighting in scientific advancement.

ACKNOWLEDGEMENTS

Solvent Paper:

The ACC's Solvent Industry Group supported this work with funding and perspective. Bill Carter of the University of California-Riverside provided insight for the chemical mechanism modifications. Rosemary Zaleski of Exxon and ACC was particularly helpful in determining appropriate surrogate compounds. This material is based on work supported under a National Science Foundation Graduate Research Fellowship to Shannon Capps.

ANISORROPIA Paper:

SLC was supported by an NSF Graduate Research Fellowship, a Georgia Tech Institute Fellowship, and an Eastman Chemical Summer Graduate Fellowship. DKH acknowledges support from NASA Applied Sciences Program. AH acknowledges support from the National Sciences and Engineering Research Council of Canada. This work was partially funded by ConocoPhillips Company, the American Petroleum Institute, and US EPA STAR Grant RD-833866. Its contents are solely the responsibility of the grantee and do not necessarily represent the official views of the US EPA. Further, US EPA does not endorse the purchase of any commercial products or services mentioned in the publication.

DP Adjoint Paper:

We acknowledge support from NASA-ACMAP and NOAA. SLC gratefully acknowledges the NSF GRF and NASA ESSF. DKH acknowledges support from a NASA New Investigator grant. We also thank two anonymous reviewers for comments that improved the manuscript.

GEOS-Chem Paper:

SLC was supported by a NASA Earth Systems Science Fellowship.

TABLE OF CONTENTS

LIST OF TABLES

LIST OF FIGURES

SUMMARY

Atmospheric aerosols and certain gases negatively affect human health and shape the Earths climate. Characterization of ambient changes due to anthropogenic emissions and realization of societal benefits from policy actions require unraveling the complex interactions of humans and the Earth system. Chemical transport models have proven very useful for assessing action plans and understanding the complex processes of the atmosphere. Augmenting these models with advanced sensitivity analysis techniques transforms them into far more effective investigative tools by increasing computation efficiency and even enabling unique probing of a problem. Specifically, the application of adjoints provides insights akin to reversing the model in time and space to understand the influence of model parameters on an outcome.

Traditional sensitivity analysis as well as the Decoupled Direct Method (*Dunker*, 1984) to understand the extent to which incorporating chemical information in regulatory decisions would affect the ozone concentrations locally and downwind in the Northeastern US.

Development of the adjoint of ISORROPIA, an inorganic aerosol thermodynamic equilibrium model (*Nenes et al.*, 1998), follows; incorporation of this adjoint into global and regional scale chemical transport model adjoints often provides the same specificity in the sensitivity analysis or inverse modeling application commensurate with the physics of the forward model.

The adjoint of GEOS-Chem (*Henze et al.*, 2007) together with the adjoint of the *Kumar et al.* (2009) parameterization (*Karydis et al.*, 2012) clarifies the inorganic aerosol precursor emissions that lead to formation of clouds in specific regions of the northern hemisphere. The integration of the adjoint of ISORROPIA with that of GEOS-Chem has made the treatment of gradients of the ammonium-sulfate-nitrate aerosol system commensurate with the

representation of this system in the GEOS-Chem model, which will serve future sensitivity analysis or inverse modeling efforts with this adjoint modeling framework or another that incorporates it.

CHAPTER I

INTRODUCTION

Atmospheric gases and aerosols significantly influence the quality of life today and have the potential to shape the evolution of Earthś climate. Certain gases and aerosols, which are solid or liquid particles suspended in the air, alter the radiative heat balance of Earth (*Forster et al.*, 2007) and affect human health upon inhalation (*US Environmental Protection Agency*, 2004; *Agency*, 2008). In an effort to understand mechanisms of climate change and to optimize methods of improving air quality, atmospheric models have been developed to elucidate the effects of natural and anthropogenic emissions of chemicals and particles into the atmosphere. Atmospheric chemistry modeling couples meteorological dynamics with chemical transformation through mathematical frameworks to predict the behavior and fate of atmospheric species. These tools quantitatively express our understanding of atmospheric composition and are key for effective public policy decisions.

Significant progress in the development of these tools has enabled scientists to quantify air quality regionally and to predict climate change globally with varying degrees of uncertainty. Deciphering the source of an aerosol particle after it has traveled through various meteorological and chemical conditions requires complex analysis due to the nature of the modeling systems. Sensitivity analysis techniques such as adjoint models advance the capabilities of modelers beyond simply executing the model which altered parameters to assess their impact by allowing insights oriented around model output not before possible and more efficiently than ever. Across the broad spectrum of climate and health effects, inquiries impossible to make via observation or experiment due to the relevant time scale or spatial range are becoming feasible with the application of advanced sensitivity analysis techniques in chemical transport models (CTMs) as investigative tools.

1.1 Transformation of Atmospheric Constituents

Atmospheric chemistry is increasingly well understood. Evidence of this knowledge is that ozone, a poorly-characterized gas formed from the precursor species oxides of nitrogen (NO_x) and volatile organic compounds (VOCs), plagued cities a generation ago but can now be fairly accurately predicted by regional CTMs. The development of knowledge, assessment tools, and pollution prevention strategies has been a joint effort of academia, regulatory agencies, and industry. The opportunities to tune concentrations of ambient ozone to levels desired are now ubiquitous because of the excellent understanding of this non-linear system cultivated over the last half of the twentieth century.

Aerosols and their interaction with water are not as easily described at this point in time (*Forster et al.*, 2007). Although these species have also been of interest for quite some time because of visibility impairment, health effects, and climatological impacts, the complexity of describing even aerosol concentrations accurately is magnified by the challenge of describing populations of solid or liquid particles with capability of partitioning into the gas phase. The most inroads have been made with the inorganic species most abundant in the atmosphere including Na^+, K^+, NH_4^+, Ca^{2+}, Mg^{2+}, SO_4^{2-}, Cl^-, and NO_3^- as these species are fairy accurately described by thermodynamic equilibrium at relevant atmospheric time scales (*Fountoukis and Nenes*, 2007). Organic species currently provide more open-ended questions with regard to aerosol composition and population evolution (*Jimenez et al.*, 2009). Nevertheless, advanced techniques for atmospheric aerosols that serve to formulate emission control scenarios to serve society are still in development and are not widely used by environmental decision makers.

Finally, the condensation of water upon aerosol can create droplets, which make up clouds. Since aerosol act as cloud condensation nuclei (CCN), the radiative and precipitative properties of clouds can be affected by emissions of gaseous species that are precursors to aerosol (*Twomey*, 1974). This complex process is important to represent accurately in CTMs or climate models in order to provide similar societal opportunities that have been

enjoyed with ozone; elucidating the relationships between emissions of specific species, aerosol populations, and cloud droplet formation would represent a first step in this direction. Nonetheless, clouds are an integral part of a complex water cycle that could not be fully captured without, at least, meteorology being conducted in real time although an integrated atmospheric-terrestrial-hydrological model would better represent this system comprehensively.

1.2 Advanced Sensitivity Analysis Techniques

Understanding the relationship between model parameters or input and the results of a modeling effort is often called sensitivity analysis. Given a CTM, the simplest approach to determine the significance of particular parameter is to tweak it slightly and compare the results before and after the change. Often termed brute force analysis, this finite difference-based approach can be found in almost any area of study. The advantage is that no additional model development is necessary, but the savings of capital resources lead to heavy computational costs in any sensitivity analysis study. Furthermore, CTMs were never designed to represent differences accurately, only concentrations, which often leads to significant numerical error when conducting finite difference-based sensitivity analysis.

An alternative approach is to employ the derivative of the numerical steps that translate model input and parameters into results. Two techniques for doing so have emerged in the atmospheric chemistry field, which are complementary to one another. Formulation of the tangent linear model has often been called the Decoupled Direct Method (*Dunker*, 1984); this forward sensitivity analysis technique efficiently calculates the sensitivity of a single input parameter to the entire result field without changing the output field in any way. This advanced sensitivity analysis technique is gaining traction with environmental decision makers, who are using it to inform decisions about emissions controls for ozone. A complementary technique is adjoint-based sensitivity analysis, which efficiently calculates the sensitivity of a specific output with respect to many (thousands to millions) of input

parameters without altering the model output or parameters (*Menut et al.*, 2000). The advantage of this technique is that it enables inverse modeling in a four-dimension variational data assimilation framework; however, the negative aspect is the burdensome development process. Long employed by meteorologists (*Sasaki*, 1958), the inverse modeling capabilities provided by the adjoint approach are promising particularly as satellite observations of atmospherically-relevant trace gases and aerosol increase.

1.3 Thesis Outline

The goal of this thesis is to develop and apply sensitivity analysis techniques to atmospheric ozone, inorganic aerosol, and cloud droplets to better understand relationships of emissions to ambient outcomes through chemical transport modeling. Chapter 2 describes the potential local and downwind concentration changes from using chemical information about solvents to change emissions regulations; this approach employs the regulatory Community Multiscale Air Quality Model (CMAQ) with both the finite difference sensitivity analysis approach and the Decoupled Direct Method (*Cohan et al.*, 2005; *Dunker et al.*, 2002) of sensitivity analysis. Chapter 3 describes the development of ANISORROPIA (the adjoint of ISORROPIA, a widely used inorganic aerosol thermodynamic equilibrium model (*Nenes et al.*, 1998, 1999)) and its application to atmospherically relevant inorganic species as well as observations from field campaigns. In Chapter 4, the adjoint of the global chemical transport model GEOS-Chem (*Henze et al.*, 2007) in tandem with a cloud droplet activation parameterization adjoint (*Karydis et al.*, 2012) is used to investigate the footprint of emissions contributing to cloud formation currently as well as changes in these values projected in the future. In Chapter 5, the integration of ANISORROPIA with the adjoint of GEOS-Chem provides an opportunity to examine the effects of inorganic aerosol thermodynamic models in sensitivity relationships as well as concentrations. Finally, Chapter 6 discusses future directions for adjoint-based sensitivity analysis in chemical transport and climate modeling.

CHAPTER II

LOCAL AND DOWNWIND IMPACTS OF REACTIVITY-BASED SUBSTITUTIONS

Three-dimensional chemical transport modeling of six different solvent substitution test scenarios was used to investigate possible transport effects of using volatile organic compound (VOC) reactivity scales for air quality management purposes with a particular focus on the northeastern United States. The primary issues analyzed are whether uses of reactivity-based substitutions adversely affect ozone concentrations downwind of the area in which they are applied and which reactivity scales appear most appropriate for areas where ozone transport between multiple cities is significant. VOC substitution scenarios were designed to assess biases in ozone metrics associated with substituting relatively highly reactive VOCs (as defined by the Maximum Incremental Reactivity (MIR) scale) associated with solvent use with less reactive VOCs that might be considered as possible substitutes. Aiming to balance industrially realistic and scientifically relevant constraints, the set of solvent emissions to be substituted included toluene, isomers of xylene, 2-butoxyethanol by the surrogate, and lower reactivity compounds 2-methylheptane and n-butyl acetate. For a 14-day episode in August 2002, seven scenarios were modeled including base-case emissions, removal of the selected higher reactivity solvent compounds, and substitution tests using the equivalent mass or equivalent reactivity-adjusted emissions based on the MIR and Maximum Ozone Incremental Reactivity (MOIR) reactivity scales.

This chapter published as: Capps, S. L., Y. Hu, and A. G. Russell (2010), Assessing near-field and downwind impacts of reactivity-based substitutions, Journal of the Air & Waste Management Association, 60, 316-327, doi:10.3155/1047-3289.60.3.316. .

Results show that downwind increases in ozone concentrations are noticeable for the MIR-based substitution test scenarios although sensitivities demonstrate that these could be used to complement oxides of nitrogen (NO_x) controls. However, using the MOIR-scaled substitution test scenario led to results that were less biased, and the population-weighted metric showed little bias compared with the base case. Temporally and spatially extensive decreases are evident with the solvent mass substitution and the selected emissions removal test scenarios, supporting the conclusion that reactivity-based control can be used to regionally reduce ozone.

2.1 Introduction

The formation of the ozone from emissions of volatile organic compounds (VOCs) and nitrogen oxides (NO_x) has led policy-makers to regulate anthropogenic VOC emissions (*Seinfeld and Pandis*, 2006a). The traditional approach to VOC control has been to reduce the total mass of VOC emissions; however, control strategies that take into account the differing chemical behavior of VOCs would likely be more efficient and effective in areas with persistent nonattainment problems and urban centers (*Russell et al.*, 1995; *McBride et al.*, 1997; Ano, 2005a). The extent to which VOCs vary in their propensity to form ozone (also referred to as reactivity) becomes evident upon comparing two simple organic compounds, ethane (C_2H_6) and ethene (C_2H_4). Calculations find that ethene will produce approximately fourteen times more ozone than would ethane on a mass basis in an urban area (*Carter*, 1994; *Finlayson-Pitts and Pitts*, 1997). Some VOCs even reduce ozone formation (*Carter and Atkinson*, 1989). As studies have documented, emissions regulations accounting for the orders of magnitude differences in reactivity of various VOCs have the potential to reduce ozone-pollution control costs by targeting controls on those compounds that most efficiently form ozone (*Avery*, 2006; *Croes et al.*, 1992; *Dimitriades*, 1996; *Luecken and Mebust*, 2008; *Bergin et al.*, 1995). Further, pursuing an approach based purely on reducing the mass of VOC emissions could lead to a product reformulation that uses higher reactivity VOCs, which could cause ozone increases (*California Air Resources Board*, 2009). Recognizing such issues, the states of California and Texas as well as the federal Environmental Protection Agency (EPA) have implemented policies that directly account for the ozone-forming potential of specific VOCs by including reactivity-based emissions regulation for specific areas (e.g., the Houston-Galveston-Brazoria nonattainment area, the State of California) or specific VOC source categories (e.g., aerosol coatings products) (Ano, 2005a; *Wang et al.*, 2007; Ano, 2005b).

Throughout the development of reactivity-based regulations, the method of quantifying the ozone impact of each VOC has been an important question (*Carter*, 1994). To regulate

various sources of emissions, a system able to quantify ozone-impacts of VOC emissions is required. Two scales formulated from box-model calculations are the Maximum Incremental Reactivity (MIR) and Maximum Ozone Incremental Reactivity (MOIR) scales (*Carter*, 1994).

Incremental reactivity is the incremental change (Δ O_3) in ozone formed due to a small increase in a VOC of interest (Δ VOC_i):

$$\mathrm{IR} = lim\left(\frac{\Delta O_3}{\Delta VOC_i} = \frac{\partial O_3}{\partial VOC_i}\right) \tag{2.1}$$

Using this approach, the reactivity of a number of species can be found, and from that, a reactivity scale developed. This quantity, however, depends upon the conditions at which the incremental reactivity is calculated. Carter addressed this point by using a set of atmospheric box model calculations, in which the amount of NO_x added was adjusted (*Carter*, 1994). This work led to the identification of multiple incremental reactivity scales. The two most widely cited scales are the MIR and MOIR scales. The MIR scale quantifies the IR of a specific VOC at the concentration of NO_x that maximizes the incremental reactivity of the base VOC mixture:

$$\mathrm{MIR}_i\left(\frac{\mathrm{g}O_3}{\mathrm{gVOC}_i}\right) = \left(\frac{\Delta[O_3]}{\Delta[\mathrm{VOC}_i]}\right)\Big|_{\max\left(\frac{\Delta[O_3]}{\Delta[VOC_{mix}]}\right)} \tag{2.2}$$

Alternately, the IRs for the MOIR scale are calculated when the ozone levels are greatest:

$$\mathrm{MOIR}_i\left(\mathrm{g}O_3\mathrm{gVOC}_i\right) = \left(\frac{\Delta[O_3]}{\Delta[\mathrm{VOC}_i]}\right)|_{max([O_3])} \tag{2.3}$$

Further explanation can be found in *Carter* (1994).

The MIR scale might be appropriate in regions with relatively higher levels of fresh NO_x emissions and relatively little biogenic VOC input (e.g., cities like Los Angeles with substantial traffic NO_x emissions) and is used in California. The MOIR scale represents conditions that have a higher VOC/NO_x ratio, as would be found in areas that have more

VOC emissions (e.g., areas with substantial biogenic or industrial VOC emissions). The approach used to find the MIR and MOIR scales, however, does not treat multiday transport, transport between cities, or capture what would happen to air masses advected a significant distance from the downtown part of a major city. Given the relatively short lifetime of NO_x, as compared to a majority of the VOCs, transport leads to an increasing VOC/NO_x ratio as the NO_x is oxidized. This effect would suggest that the MIR scale becomes less appropriate in areas that are influenced by significant transport, as well as areas with higher VOC emissions. Such concerns led to a series of studies using three-dimensional chemical transport models from the Reactivity Research Working Group, a consortium of scientists and policy analysts working to provide an improved scientific basis for reactivity-related regulatory policies (*Arunachalam et al.*, 2003; *Carter*, 2005; *Carter et al.*, 2003; *Hakami et al.*, 2004a,b; *Hales*, 2007).

Interpretation of the results identified a number of questions that remain in the application of reactivity scales for ozone management purposes (*Hales*, 2007). One concern, particularly for policy makers in regions with closely spaced urban centers, is whether regulating emissions on a reactivity basis will increase ozone concentrations downwind of an area where reactivity-based substitutions are implemented, possibly having an impact on downwind non-attainment areas and exposure (*Bergin et al.*, 1995; *Agency*, 2008; *Hakami et al.*, 2004c). This work assesses the near-field and downwind impacts of substituting solvent emissions in the Northeastern U.S. using the Community Multiscale Air Quality (CMAQ) model (*Byun and Schere*, 2006) by simulating replacement of a set of typical solvent VOCs with two lower reactivity VOCs that could be substitutes. Particular attention is paid to downwind effects as well as spatial and population exposure potential metrics.

2.2 Methods

2.2.1 Model Specifications

Air quality modeling is conducted using CMAQ version 4.5 with the SAPRC 99 chemical mechanism (*Carter*, 2000a,b) extended to include more detailed chemical kinetic descriptions of additional species. CMAQ is designed for various applications, including analysis of potential regulations and investigation of complex chemical interactions (*Byun and Schere*, 2006) and has been updated with a mass conservation scheme (*Hu et al.*, 2006) and equipped with the Decoupled Direct Method in Three Dimensions (DDM-3D) (*Cohan et al.*, 2005; *Dunker et al.*, 2002; *Napelenok et al.*, 2006; *Yang et al.*, 1997). SAPRC 99 is a detailed, condensed chemical mechanism suitable for conducting reactivity assessments because it is extensible to new species (`http://www.engr.ucr.edu/~carter/SAPRC/`).

A one-way nested modeling approach is used. The outer domain covers most of North America with 36 km x 36 km horizontal grids and a nested domain covers the northeastern United States and southern Canada with a 12-km horizontal resolution grid (Figure 2.1). Both the coarse and fine grid domains have thirteen vertical layers extending about 15.9 km above ground with 7 layers below 1 km and a thickness of 18 m for the first layer. Boundary conditions for the outer domain are set to the default conditions, and the 36-km domain results set the time- and space-varying boundary conditions for the 12-km domain.

The Fifth-Generation PSU/NCAR Mesoscale Model (MM5) (*Grell et al.*, 1995) is used to develop the meteorological fields and is run with 34 vertical layers using four-dimensional data assimilation (FDDA) techniques and the Pleim-Xiu Land-Surface Model (PX-LSM) (*Pleim and Xiu*, 1995; *Xiu and Pleim*, 2001). The Sparse Matrix Operator Kernel for Emissions (SMOKE) is used for processing emissions to produce gridded, CMAQ-ready emissions (Ano, 2008). Inventories used include the United States National Emissions Inventory of 2002 (`http://www.epa.gov/ttn\discretionary{-}{}{}/chief\discretionary{-}{}{}/net/2002inventory.html`), the Canadian 2000 National Inventory, and Mexicos National Emissions Inventory of 1999 (`http://www.epa.gov/ttn/`

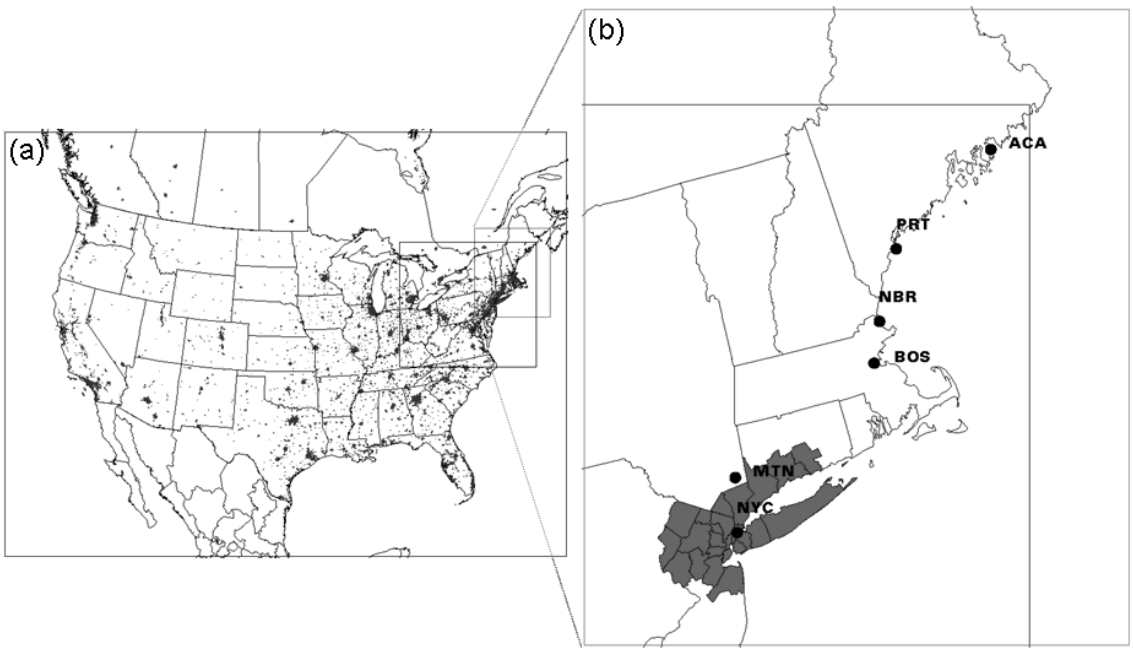

Figure 2.1: (a) Outer and nested domains modeled at a 36- and 12-km resolution, respectively, are given by the black boxes. Urban areas are shown in black. (b) The city-based substitution domain is shown in gray and encompasses the NJ-NY-CT nonattainment area. Ozone monitor location acronyms and type of location: NYC (urban), MTN (suburban), BOS (urban), NBR (suburban), PRT (urban), and ACA (rural).

`chief/eiinformation.html`). The U.S. inventory is further updated with the VISTAS 2002 (*Barnard and Sabo*, 2008) and MANE-VU 2002 (V3) emissions inventory (`http://www.marama.org/technical-center/emissions-inventory/2002-inventory-and-projections/mane-vu-2002-emissions-inventory`). SPECIATE version 3.2 is used for speciation of emissions, necessary for analysis of the solvent emissions inventory (Ano, 2002).

The MM5/SMOKE/CMAQ system is applied to the period of August 5-18, 2002, with the first two days being used for ramp-up to minimize the impacts of initial conditions. This episode was selected because it included multiple observed 8-hour average ozone concentration (from here onward, 8-hour average) exceedances of the National Ambient Air Quality Standards (NAAQS) across the Northeastern part of the U.S., a region potentially susceptible to downwind enhancements of ozone concentrations due to transport when

reactivity-based substitutions are employed. In addition to multiple exceedances (e.g., on August 12), the episode includes days with more typical peak ozone values very similar to current NAAQS standards, providing insight for more commonly occurring ozone concentrations (e.g., August 10).

2.2.2 Chemical Selection

The effects of replacing high reactivity compounds or mixtures with greater or equal amounts of less reactive species are investigated with a focus on the solvent industry sector. The methodology consists of identification of highly reactive solvent compounds and selection of realistic lower reactivity surrogate compounds. Solvent compounds contributing most significantly on the basis of reactivity were identified by analyzing the speciated solvent emissions inventory for the MANE-VU region using SMOKE and Speciate 3.2 VOC source profiles (Figure 2.2). The MIR- and MOIR-weighted contributions of each species to the total reactivity of the mixture were used to identify the species to be replaced (Eq. (2.4), (2.5)).

$$\text{Species } i \text{ Contribution} = \text{SC}_i = (\text{Emis}_i)(\text{MIR}_i) \tag{2.4}$$

$$\text{Fractional Species}i \text{ Contribution} = \frac{\text{Species } i \text{ Contribution}}{\text{Total VOC Production}} = \frac{\text{SC}_i}{\sum_{j=1} \text{SC}_j} \tag{2.5}$$

where $Emis_i$ is the emissions of species i in grams per day over the domain. In an actual airshed no scale is expected to work everywhere, so the above equations provide only an estimate of the fraction of ozone that would be due to the individual VOC species. On an MIR-basis, the three highest contributors to ozone formation were identified as toluene, xylene (including all isomers), and 2-butoxyethanol with (MIR, MOIR) values of (3.97, 1.17), (7.46, 2.37), and (2.93, 1.28), respectively. Of the nearly 2000 tons of solvent-related VOC

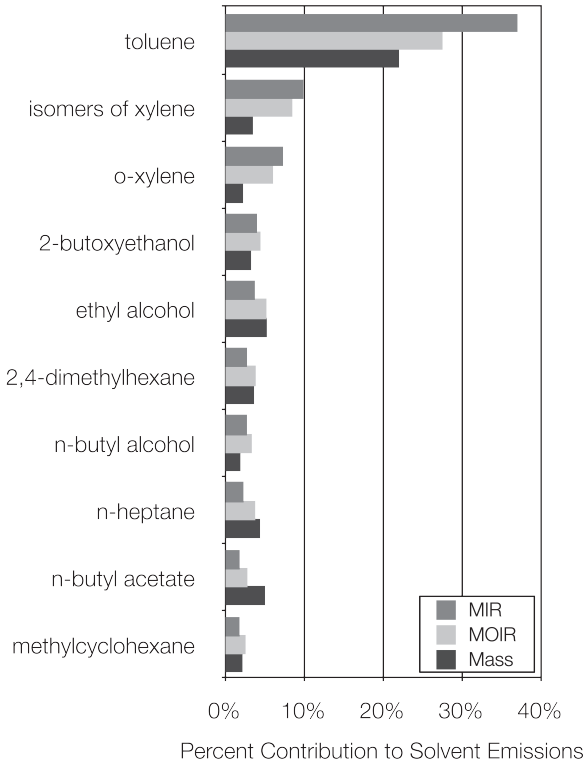

Figure 2.2: Specific chemical emissions for the solvent sector were developed from the Source Characteristic Categories in the MANE-VU region in combination with SPECIATE 3.2; the 10 most significantly emitted chemicals on the basis of MIR-scaled reactivity are shown. Bars representing contribution in terms of MIR, MOIR, and mass quantities demonstrate the significance of regulating based on reactivity rather than mass of emissions because many chemicals would rank differently in percent contribution if the chart were ordered based on mass (n-butyl acetate, ethyl alcohol).

per day emitted in the MANE-VU region, these chemicals contributed 59% of the MIR-weighted and 48% of the MOIR-weighted emissions. Significant portions of these contributions are from domestic use of solvents, coating applications of solvent-based paint, and degreasing. When processed with SMOKE, removal of these species resulted in a 35% reduction in mass of solvent emissions or 7% of anthropogenic emissions of the model species used to represent these compounds. For the domain-wide substitutions, these compounds are replaced throughout the modeling domain with lower reactivity compounds, not solely in the MANE-VU region.

Identification of lower reactivity compounds for use as a surrogate mixture was guided by the California Air Resources Board reactivity-based regulations (Ano, 2005a; *California Air Resources Board*, 2001, 2007) and a recent European evaluation of the impacts of reactivity-based substitution test scenarios (*Bessagnet and Rouïl*, 2006). In addition, consultation with representatives of solvent manufacturers through the American Chemistry Council (*Zaleski*, 2008) led to selection of two potential VOC substitutes, n-butyl acetate and 2-methylheptane as reasonable compounds for assessing the downwind impacts (*Carter*, 2008; *Wang et al.*, 2002). The (MIR, MOIR) of n-butyl acetate and 2-methylheptane are (0.89, 0.54) and (1.34, 0.80), respectively. For comparison, the (MIR,MOIR) for ethane are (0.3, 0.19). VOCs less reactive than ethane are not typically treated as reactive VOCs by the EPA as in the case of aerosol coatings (Ano, 2003). The chemical mechanism in CMAQ was extended to include chemistry explicit to these two species as suggested by *Carter* (2008) by including their reactions with the hydroxyl radical (Eq. (2.6), (2.7)) (*Carter*, 2000b, 2008, 2010).

$$\begin{aligned}\mathrm{BUACET} \ + \ \mathrm{HO} \ &= 0.688\ \mathrm{RO2R} \ + 0.19\ \mathrm{RCO3} \ + 0.122\ \mathrm{RO2N} \ + 0.515\ \mathrm{R2O2} \\ &+ 0.01\ \mathrm{CO} \ + 0.116\ \mathrm{CCHO} \ + 0.173\ \mathrm{RCHO} \ + 0.253\ \mathrm{MEK} \\ &+ 0.262\ \mathrm{PROD2} \ + 0.2\ \mathrm{CCOOH}\end{aligned} \tag{2.6}$$

$$\begin{aligned}\mathrm{MEC7} \ + \ \mathrm{HO} \ &= 0.659\ \mathrm{RO2R} \ + 0.341\ \mathrm{RO2N} \ + 0.881\ \mathrm{R2O2} \ + 0.014\ \mathrm{HCHO} \\ &+ 0.025\ \mathrm{CCHO} \ + 0.149\ \mathrm{RCHO} \ + 0.022\ \mathrm{ACET} \ + 0.549\ \mathrm{PROD2}\end{aligned} \tag{2.7}$$

The reaction rate constants at 298 K are 4.20 x 10^{-12} cm^3 mol$^-$1 s$^-$1 and 8.31 x 10^{-12} cm^3 mol^{-1} s^{-1}, respectively. Equal emissions, on a mass basis, of 2-methylheptane (MEC7) and n-butyl acetate (BUACET) are added in the test scenarios.

Table 2.1: Nomenclature and description of modeling scenarios.

Scenario	Description	VOC Emissions Removed (t/day)			Surrogate Compound Emissions Added (t/day)		Total VOC Emissions (% of mass in base case)
		Toluene	Xylene	2-Butoxyethanol	*n*-Butyl Acetate	2-Methylheptane	
	MIR, MOIR	3.97, 1.17	7.46, 2.37	2.93, 1.28	0.89, 0.54	1.34, 0.80	
Null	Selected VOC removed	483	134	74	0	0	78
Mass	Selected VOC replaced with equal mass surrogate	483	134	74	323	323	99
MIRd	Selected VOC replaced with MIR-based reactivity equivalent domain-wide	483	134	74	1307	1307	162
MIRc	Selected VOC replaced with MIR-based reactivity equivalent within NY-NJ-CT nonattainment area	139	38	22	377	377	118
MOIRd	Selected VOC replaced with MOIR-based reactivity equivalent domain-wide	483	134	74	677	677	121
MOIRc	Selected VOC replaced with MOIR-based reactivity equivalent within NY-NJ-CT nonattainment area	139	38	22	196	196	104

2.2.3 Test Scenarios

Seven emissions test scenarios were crafted to elucidate the effects of reactivity-based substitutions as well as the impact of selecting either the MIR or MOIR scale for regulating the exchange (Table 2.1). A base case included the standard emissions inventory. Secondly, a null case removed the subset of solvent emissions that were to be substituted; that is, the emissions were reduced by the amount of mass of the selected solvents. Thirdly, the selected emissions were substituted on an MIR-scaled equal-reactivity basis throughout the modeled domain, which is referenced as the MIRd case. The substitution maintained the original spatial and temporal distribution of emissions but increased the mass of emissions to the point that the lower reactivity surrogate species contributed the same MIR-based reactivity as the original mixture For the MIRc case, the same MIR-scaled equal-reactivity basis was applied solely to the New York - New Jersey - Connecticut (NY-NJ-CT) 8-hour ozone nonattainment area (Figure 2.1). The MOIRd emissions test scenario considers the MOIR-based equal-reactivity substitution of the selected emissions throughout the domain, much like the MIRd case although the increase in mass was less than that of the MIR test scenario. An MOIRc case was executed analogous to the MIRc test scenario. Finally,

an equivalent mass test scenario replaced domain-wide emissions identified above with an equivalent mass of the surrogate species mixture.

For the null, MIRd, MOIRd, and mass emissions scenarios, the 36-km and 12-km resolution domains were both executed to establish proper initial and boundary conditions, whereas these were given by the base case for the base, MIRc, and MOIRc cases. In addition to the substitution scenarios, DDM-3D was used to calculate the sensitivities of ozone formation to anthropogenic VOC and NO_x base case emissions domain-wide. Sensitivity fields (Figure 2.3) are used to identify the geographical areas that are VOC sensitive and reactivity-based VOC control is expected to be most applicable or where implementing NO_x controls in tandem could be an effective measure.

2.2.4 Analysis Techniques

Three different representations of modeling results facilitate the analysis and inter-comparison of the relevant ozone metrics from test scenarios, including hourly averages and 8-hour maxima. Time series analysis reveals temporal effects; a geographical representation of the differences demonstrates spatial effects at a given time; and scalar values that capture the change from base and null test scenarios provide an integrated measure of the spatial and temporal effects.

To better understand transport effects, six ozone monitors located from New York City (NYC) to Acadia National Park (ACA) in Maine were identified for time series analysis. These include one site directly downwind from NYC (Mt. Ninham: MTN), Boston (BOS), and two coastal sites north of BOS: Newbury (NBR) and Portland (PRT) (Figure 2.1). These sites capture the evolution of the plume from NYC and how additional emissions and reactions impact the use of reactivity adjustment in transport situations. For the grid cell over each of these locations, the difference from base case concentrations for hourly average values (Eq. 2.8) and 8-hour maxima (Eq. 2.9) are compared for each test case.

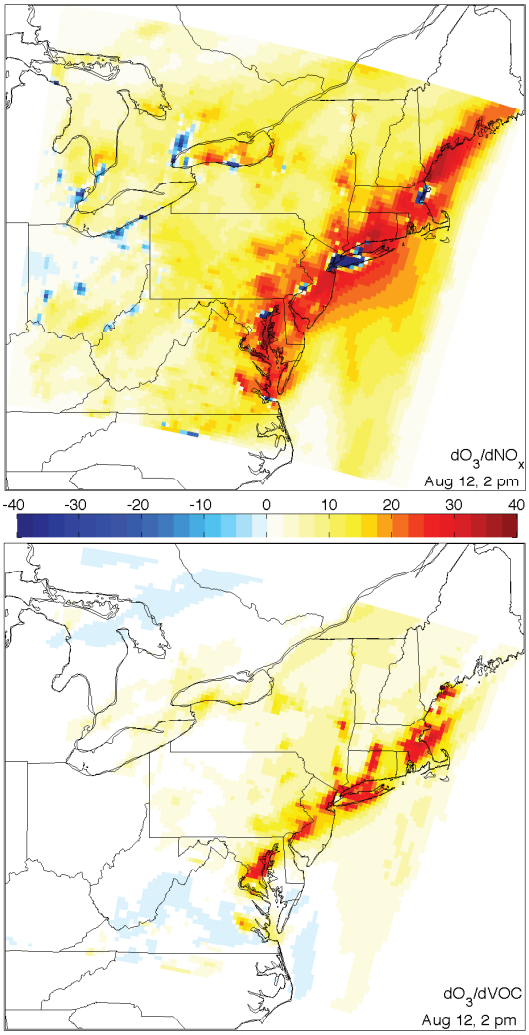

Figure 2.3: Sensitivity of ozone concentration to anthropogenic (a) NO_x and (b) VOCs at 2 pm on August 12, 2002. Units are ppbv per total NO_x (or VOC) emissions.

$$\mathrm{HourlyAverageDifference} \equiv [\mathrm{O_3}]_{\mathrm{1hr,case}} - [\mathrm{O_3}]_{\mathrm{1hr,Base}} \tag{2.8}$$

$$8-\mathrm{hourMaxDifference} \equiv [\mathrm{O_3}]_{\mathrm{8hrmax,case}} - [\mathrm{O_3}]_{\mathrm{8hrmax,Base}} \tag{2.9}$$

Additionally, the spatial patterns of model results are investigated. Spatial plotting of the difference from the base case 8-hour maximum for each scenario on two dissimilar episode days provides insight into the local and downwind behavior of ozone concentration

changes (*Agency*, 2008). Looking solely at the absolute change does not provide a comprehensive picture of the performance of a reactivity scale because the absolute sensitivity of ozone to the VOCs being removed varies spatially.

The fractional bias (FB) describes the relationship of each reactivity-based test scenario to the null and base case scenarios:

$$\mathrm{FB} \equiv \frac{[\mathrm{O_3}]_{\mathrm{8hrmax,case}} - [\mathrm{O_3}]_{\mathrm{8hrmax,Base}}}{\max\left([\mathrm{O_3}]_{\mathrm{8hrmax,Base}} - [\mathrm{O_3}]_{\mathrm{8hrmax,Null}}, 0.75\mathrm{ppb}\right)} \tag{2.10}$$

where $[\mathrm{O_3}]_{\mathrm{8hrmax,case}}$ represents the daily 8-hour maximum calculated for the case of interest, $[\mathrm{O_3}]_{\mathrm{8hrmax,Base}}$ represents the 8-hour maximum for the base scenario, and similarly for the null case representation as defined above. Calculating the fractional bias metric throughout the spatial and temporal extent of the domain provides an assessment of the relative bias, which is more directly comparable between test scenarios and between studies. For example, if one study only used half of the substitution as this one, while the absolute change would be expected to be halved, the fractional bias would be expected to remain about the same. Fractional bias values equal to zero represent exact replication of base level ozone values by the reactivity test scenario; values of -1.0 represent bias levels equivalent to removing the substituted aspects of the solvent inventory entirely. Values greater than zero indicate that the test scenario produced higher ozone concentrations than found in the base scenario at a given location and time.

A final set of metrics provides an assessment of how the test scenarios compare over the entire domain and simulation period. As a means of summarizing in a single scalar value the effects of a test scenario throughout the 12-km resolution domain and entire episode the domain-wide fractional bias (DWFB) is calculated:

$$\mathrm{DWFB_{case}} = \frac{\iiint [\mathrm{O_3}]_{\mathrm{8hrmax,case}} - [\mathrm{O_3}]_{\mathrm{8hrmax,Base}} \mathrm{d}x\ \mathrm{d}y\ \mathrm{d}t}{\iiint \max\left([\mathrm{O_3}]_{\mathrm{8hrmax,Base}} - [\mathrm{O_3}]_{\mathrm{8hrmax,Null}}, 0.75\mathrm{ppb}\right) \mathrm{d}x\ \mathrm{d}y\ \mathrm{d}t} \tag{2.11}$$

where the integration is carried out for both the temporal ($\mathrm{d}t$) and spatial extents ($\mathrm{d}x$, $\mathrm{d}y$)

of the episode resulting in a unitless, scalar factor reflecting the behavior of the MIRd, MOIRd, and Mass equivalent test scenarios in comparison to the ozone change found between the base and null cases. Cells over the Atlantic Ocean or Great Lakes and ones for which the simulated 8-hour maximum does not exceed 50 ppb for the scenario being evaluated are neglected in this calculation. The inclusion of a 0.75 ppb threshold is required to restrict the metric to reasonable values and neglect times or locations where the difference between null and base case ozone concentrations becomes negligible, indicating an area where the VOC reductions are ineffective at reducing ozone. A similar calculation is done to calculate the potential population exposure, i.e., the population-weighted domain-wide fractional bias (PWDWFB):

$$\mathrm{PWDWFB}_{\text{case}} = \frac{\iiint [\mathrm{O_3}]_{\text{8hrmax,case}} - [\mathrm{O_3}]_{\text{8hrmax,Base}} \mathrm{P}(x,y) \mathrm{d}x \; \mathrm{d}y \; \mathrm{d}t}{\iiint \max([\mathrm{O_3}]_{\text{8hrmax,Base}} - [\mathrm{O_3}]_{\text{8hrmax,Null}}, 0.75\mathrm{ppb}) \mathrm{P}(x,y) \mathrm{d}x \; \mathrm{d}y \; \mathrm{d}t} \tag{2.12}$$

where $\mathrm{P}(x,y)$ indicates the population of the cell whose location is given by (x,y) according to the 2000 Census. As with the domain-wide fractional bias metric, the integration is only over cells with base concentrations greater than 50 ppb ozone and cells not entirely over water. By population weighting the fractional bias measure, a single scalar value elucidates the number of people potentially affected by decreases below or increases above the base concentration and to what extent.

2.3 Results and Discussion

2.3.1 Model Evaluation

Simulated surface meteorological fields were examined against hourly surface observations from the U.S. and Canada (Table 2.3) with performance well within the typical range for air quality modeling (*Emery et al.*, 2001; *Hanna and Yang*, 2001). The model reproduced the observed 8-hour averages quite well, surpassing typical benchmarks (Table 2.2, Figure 2.4). Comparison of ozone concentrations resulting from the base and null emissions

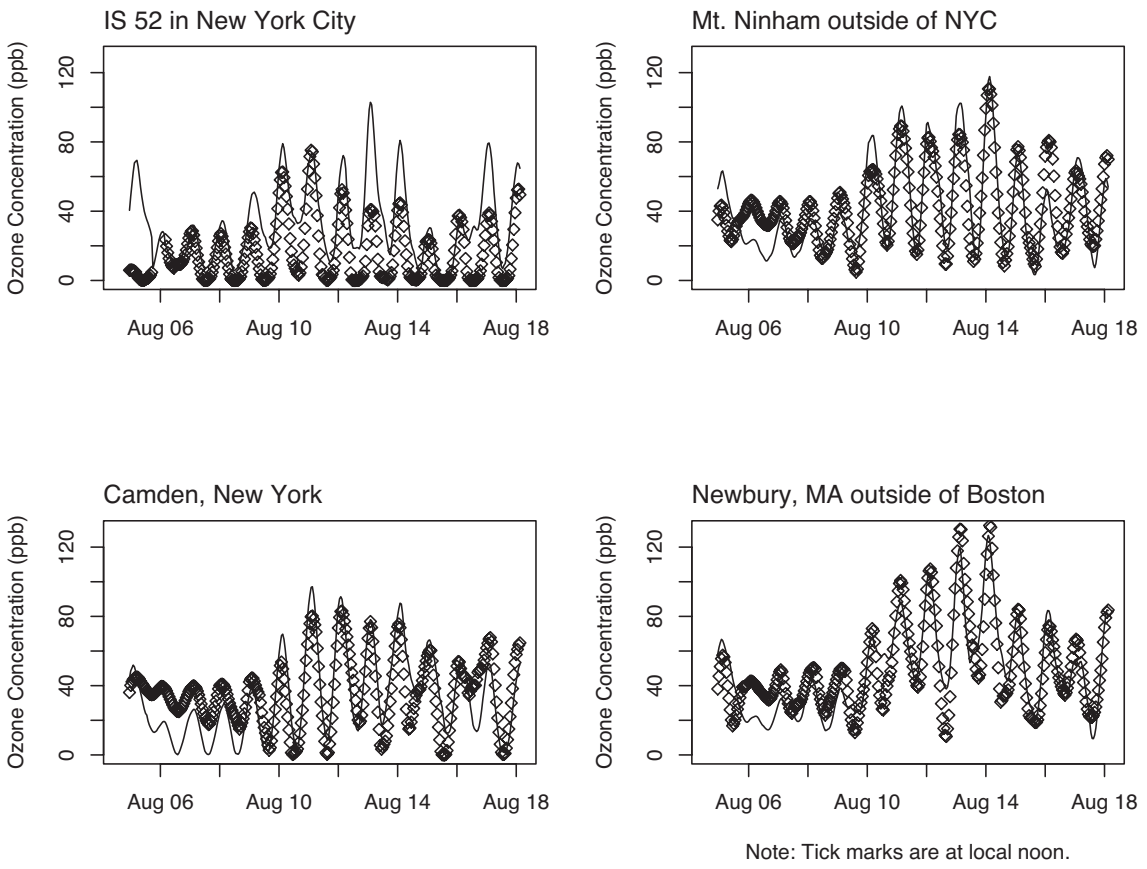

Figure 2.4: Time series analysis of modeled maximum 8 hour average ozone concentrations (black solid line) as compared to observations from individual stations (black open circle markers) at the indicated location throughout the modeled episode. For calculations that depend on the duration of the episode, August 5 and 6 are neglected.

test scenarios provided the opportunity to confirm that the simulated ozone impact of the substitutions should be readily identifiable.

2.3.2 Temporal Analysis

The first effect evident in the time series plots (Figure 2.5) is that substitution test scenarios have the greatest change from base hourly averaged ozone concentrations just before and at the time of peak ozone levels. The greatest differences at the sites analyzed temporally are decreases greater than 6 ppb in the null scenario (NYC, MTN, and NBR) and increases of up to 4.1ppb in the MIRd scenario (NBR) for hourly averages. Examination of the differences in 8-hour maxima from the time series plots shows that the changes were at

Table 2.2: Performance evaluation of meteorological field.

Characteristic	Measure	Average	Benchmark
Wind Speed	Mean Observed (m/s)	2.8	
	Mean Predicted (m/s)	3.3	
	Bias (m/s)	0.5	$\leq \pm 0.5$
	Gross Error (m/s)	1.5	≤ 2
	Index of Agreement	0.7	≥ 0.6
Wind Direction	Mean Observed (deg)	204.8	
	Mean Predicted (deg)	203.3	
	Bias (deg)	-0.3	$\leq \pm 10$
	Gross Error (deg)	28.0	≤ 30
Temperature	Mean Observed (K)	298.0	
	Mean Predicted (K)	297.3	
	Bias (K)	-0.5	$\leq \pm 0.5$
	Gross Error (K)	1.8	≤ 2
	Index of Agreement	0.9	≥ 0.8
Humidity	Mean Observed (g/kg)	13.8	
	Mean Predicted (g/kg)	13.7	
	Bias (g/kg)	0.1	$\leq \pm 1$
	Gross Error (g/kg)	1.4	≤ 2
	Index of Agreement	0.7	≥ 0.6

Table 2.3: CMAQ ozone performance against Aerometric Information Retrieval System surface monitoring stations data for August 7 - 18, 2002.

	Number of Pairs	MOC (ppbv)	MNB (%)	MNE (%)	MMC (ppbv)
Daily peak 1-hr ozone	3272	76.4	−1.2	17.0	71.5
Daily peak 8-hr ozone	3335	68.1	10.2	19.4	71.1

Note: MOC = mean observed concentration, MNB = mean normalized bias, MNE = mean normalized error, MMC = mean modeled concentration, ppbv = parts per billion by volume. EPA suggests that values for MNB and MNE between $\pm$ 15% and $\pm$ 35%, respectively, are acceptable. A 40-ppbv cutoff was used for ozone observations.

most a decrease of 3.4 ppb at the NYC site (Null case) and an increase of 2.5 ppb at the NBR site (MIRd case).

The null and mass test scenarios reveal sizable ozone decreases at the chosen sites. These test scenarios led to maximum decreases of 3 ppb and 2 ppb, respectively, in the 8-hour maxima (NYC site). These decreases support the underlying premise of reactivity-based substitutions by demonstrating that using the same mass amount of lower reactivity compounds (e.g., n-butyl acetate and 2-methylheptane) does decrease ozone concentrations relative to higher reactivity VOCs. Conversely, this shows the potential to increase

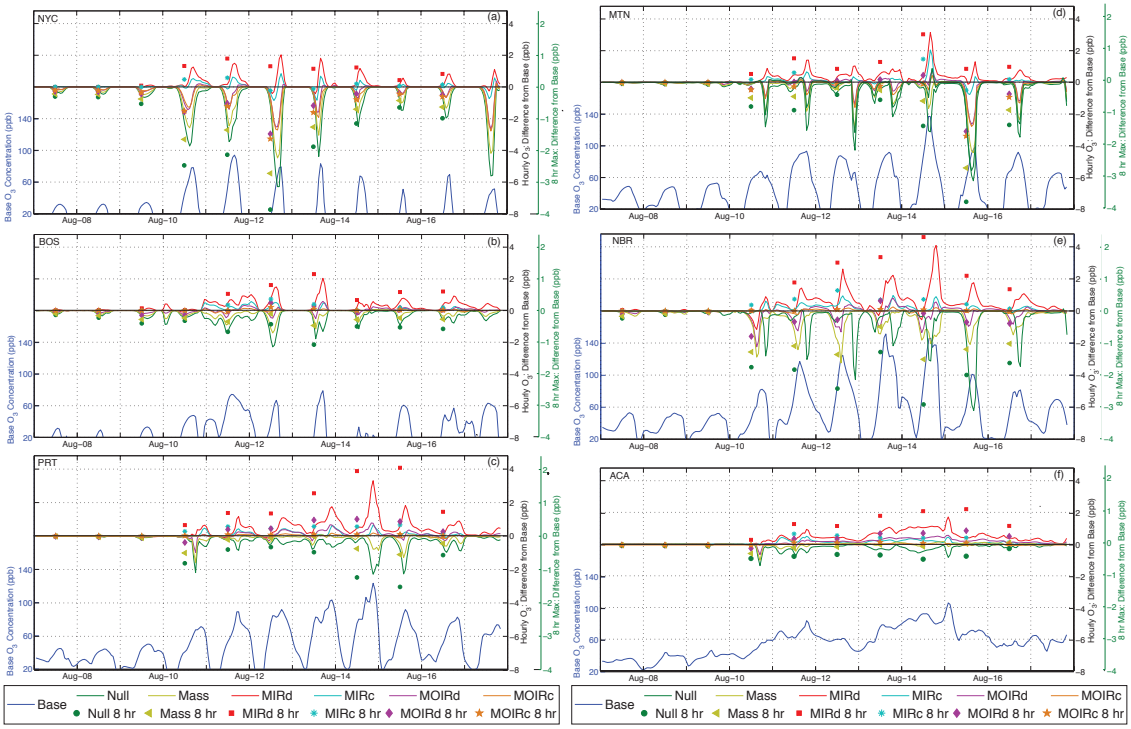

Figure 2.5: Time series analyses at geographical locations often downwind of NYC, including (a) NYC, (b) BOS, (c) PRT, (d) MTN, (e) NBR, and (f) ACA. On the left vertical axis, the base hourly averaged concentrations of ozone are denoted for the blue line. Additional lines represent the hourly average difference from base ozone concentrations, which are measured by the scale on the right vertical axis (ppb of ozone). Finally, the markers represent differences from the base scenario in daily maximum 8-hr average values, and the scale differs from that of the hourly average differences by a factor of 2. See Figure 2.1 for ozone monitor locations.

ozone by using more reactive compounds, even if there were some decrease in total mass. Additionally, the time series analysis effectively demonstrates that the decreases are often greatest in magnitude when the base ozone concentrations are highest.

For the MIR-scaled substitutions, noticeable increases in the hourly average concentrations exist near or just after the peak ozone levels. The MIRd scenario leads to increases in 8-hour averages at each of the selected monitoring locations (up to 2.5 ppb at NBR) though the magnitude of increase varies by day and location. The MIRc scenario results have maximum increases of 1 ppb at the suburban NBR and MTN sites (downwind of the substitution area) with limited effect at the urban BOS and PRT sites and the rural ACA location. Within the domain of substitution, the NYC site shows that for the majority of the

episode, the MIRc test scenario was relatively effective in the near-field (i.e., no significant deviations from base). However, just outside the area of the local substitution, the 8 hour maxima at MTN do occasionally increase due to the localized, nearby substitution.

Finally, the MOIR-based test scenario led to slight positive and more significant negative changes in hourly concentrations at different locations and times during the episode as well as less than 0.5 ppb increases and decreases exceeding 1 ppb in the 8-hr maxima at the urban NYC and BOS sites and suburban MTN location. The suburban NBR site shows mixed behavior with an increase of about 0.5 ppb for August 13, but a nearly 1 ppb decrease for August 10, and slight decreases later in the episode as well. These temporal effects demonstrate that the MOIR-based test scenario, which increased the mass by 20%, was more likely to decrease or maintain ozone concentrations than increase them throughout the duration of the episode.

The base ozone concentration at the Acadia National Park site (ACA) demonstrates different behavior than other sites due to the transport processes that lead to elevated ozone at this rural, coastal site. Throughout the episode, the base levels of ozone increase as it is produced upwind, transported over the water, and pushed downwind to ACA, where limited NO_x is present to consume it. MIR domain-wide substitution increases the 8-hr maximum by more than 1 ppb at ACA. The contribution from the MOIR domain-wide test case or the MIR substitution limited to the NY-NJ-CT nonattainment area is less than 0.5 ppb of the 8 hr max. For the localized MOIR-based substitution, the difference from base case at ACA is negligible. The time series reveals distinct effects of the test cases on downwind concentrations of ozone in a remote location.

2.3.3 Spatial Analysis

The twelve-day episode captured the spatial heterogeneity of reactivity-based substitution effects while different meteorological and ambient ozone concentrations persisted. Two

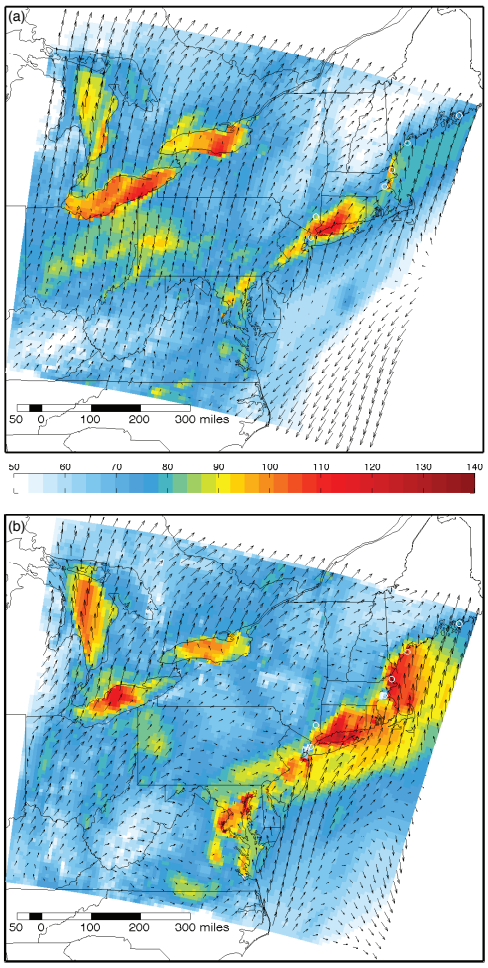

Figure 2.6: Maximum 8-hr average ozone concentration (back- ground color) with average wind fields for (a) August 10 and (b) August 12. Average wind fields represent the relative magnitude and direction of wind between 10:00 a.m. and 6:00 p.m. of the appropriate days. White circles represent the locations of ozone monitoring stations (see Figure 2.1).

days, Saturday, August 10, and Monday, August 12, provide representations of the geographical spread of effects at more typical and higher ozone concentrations, respectively (Figures 2.6, 2.7, and 2.8). The following analysis focuses first on August 12, which had lower wind speeds and higher ozone concentrations; analysis of August 10 follows. Together, these results provide a basis for understanding the spatial effects of reactivity-based substitutions over a range of meteorological and land-use conditions and at ozone concentrations relevant to VOC control measures.

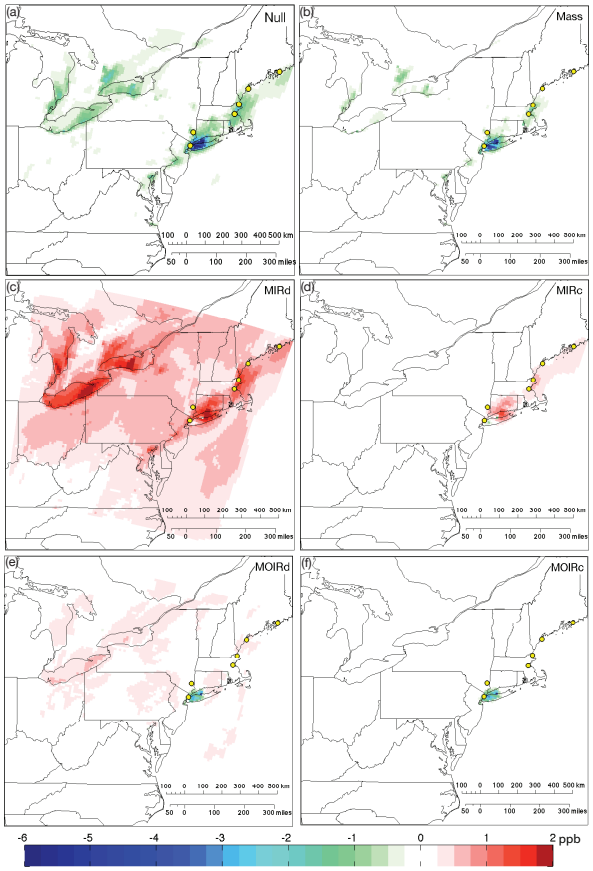

Figure 2.7: The difference in maximum 8-hr average ozone concentrations from the base case as given by null and substitution test case results minus the base case is shown in ppb ozone for August 12: (a) null, (b) mass, (c) MIRd, (d) MIRc, (e) MOIRd, and (f) MOIRc. The minimum and maximum difference values attained are -8.9 ppb from null and 2.4 ppb from MIRd, although the color scheme is chosen to optimize the resolution of differences for both scenario days shown. Yellow points represent the locations of ozone monitoring stations (see Figure 2.1).

2.3.3.1 High Ozone Concentrations

On August 12, winds were conducive to the accumulation of ozone downwind of cities and over coastal locations as relatively calm, southerly winds persisted over land, with stronger winds over the ocean (Figure 2.6b). Wind along the coast and across the Massachusetts peninsula was sufficient to transport both reactants and ozone downwind of NYC and BOS to Maine. When over the ocean where the boundary layer is shallower deposition is lessened and high ozone concentrations at PRT and ACA, even at night, often result.

Within this context, the null difference spatial plot reveals that eliminating the reactive solvents has the greatest effect around New York City, New Jersey, and Connecticut, as the 8-hour maximum is reduced by more than 6 ppb over portions of the region (Figure 2.7). Downwind, around BOS, the reductions are about 2 ppb, and a slight decrease is seen as far downwind as PRT and ACA. This suggests that VOC controls would be most effective in the NYC area, with lessening effectiveness downwind. This is also found when examining the sensitivities to domain-wide VOC and NO_x emissions (Figure 2.3).

The mass equivalent substitution produces similar effects though slightly smaller. The general bias towards lower ozone levels as compared to the base supports the conclusions that replacing highly reactive VOCs with less reactive compounds will effectively reduce ozone throughout the domain and that controlling ozone by reducing reactivity can be effective without leading to downwind ozone increases.

The MIRd and MIRc scenarios indicate a trend toward increased concentrations of ozone downwind of a substitution site with MIR-based equal reactivity substitutions. Increases were as much as 2.6 ppb downwind of where solvent emissions are most significant (e.g., the New York City area). The MIRc substitution reveals some decreases within the substituted domain, but increases of up to 1 ppb ozone in the 8-hour maximum about 150 km downwind and about 0.5 ppb beyond that to 500 km. As the persistent production of ozone is noted over the Atlantic, similar effects are observed over the Great Lakes. Although not a focus of this study, this behavior confirms that large bodies of water create favorable conditions for ozone production. Finally, the MOIRd and MOIRc test scenarios produce decreases of up to 3 ppb in the areas that have significant solvent VOC emissions. Smaller increases are found in regions with lower solvent VOC and NO_x emissions.

2.3.3.2 Moderately High Ozone Concentrations

August 10 was characterized by higher winds than August 12, leading to greater dilution of emissions and, ultimately, lower ozone (Figure 2.6a). For the null test scenario, the

largest difference from the base 8-hour maximum is smaller in magnitude (approximately 6.0 ppb decrease) than on August 12, with similar spatial patterning. Likewise, the mass test scenario produces differences similar to the null test scenario, simply with less of a decrease. The MIR-based test scenarios lead to similar effects on ozone concentration as on August 12; however, the magnitude of increases from the base case is about half of the magnitude of those increases found on August 12 and the decreases are more prevalent. For this day, the MOIRd test scenario produces negligible increases from base for the majority of the domain and decreases of up to 2.8 ppb locally and 1 ppb downwind with MOIRc having similar local effects.

The mass test scenario decreases ozone concentrations both spatially and temporally, which confirms that emissions of a set of VOCs with an equal mass of lower reactivity compounds can reduce ozone concentrations. Additionally, the spatial and temporal analyses have shown that nominal increases due to downwind transport of ozone and processing in a high VOC/NO_x ratio environment just off of the coast reduces the effectiveness of MIR-based ozone control in the Northeastern U.S.

2.3.4 Aggregate Spatio-temporal and Exposure Analysis

Comparison of the DWFB values reveals that the more detailed three-dimensional chemical transport modeling reproduces the relative behavior expected of the MIR and MOIR reactivity-based emissions scenarios as well as the equivalent-mass test scenario. These exhibit progressively more conservative results in that order (Figure 2.9). The entire interquartile ranges position above zero for the MIRd fractional bias values demonstrates the widespread tendency for this scale to increase ozone concentrations. The DWFB of 0.39 indicates that ozone levels would generally increase if VOC controls were designed to maintain constant total reactivity as given by the MIR scale (mass times MIR value), resulting in an increase in mass-based emissions. Additionally, the increases above base concentrations are amplified when population-weighted (0.45), which indicates that increases

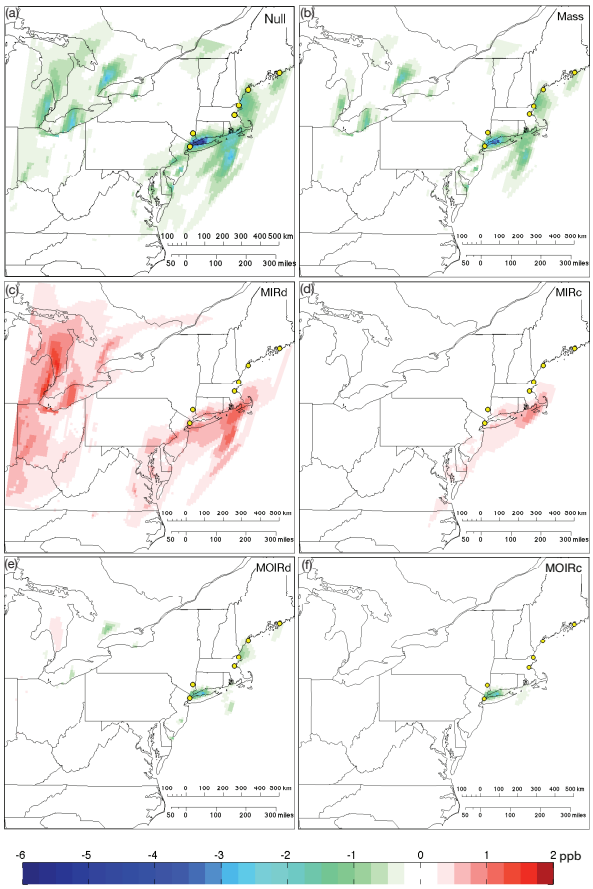

Figure 2.8: The difference in maximum 8-hr average ozone concentrations from the base case as given by null and substitution test case results minus the base case is shown in ppb O3 for August 10: (a) null, (b) mass, (c) MIRd, (d) MIRc, (e) MOIRd, and (f) MOIRc. The minimum and maximum difference values attained for are -6 ppb from null and 1.6 ppb from MIRd. Yellow points represent the locations of ozone monitoring stations (see Figure 2.1).

occurred in more populated locations, often the coastal areas, and would have the potential to increase exposure.

The DWFB for the MOIRd test scenario of 0.12 is significantly closer to zero than the MIR-scaled results, suggesting that use of this metric provides ozone control that is much more likely to produce an equal ozone result. Further, with the inter-quartile range below 0.25, the MOIRd test scenario demonstrates a tendency to under-correct ozone production

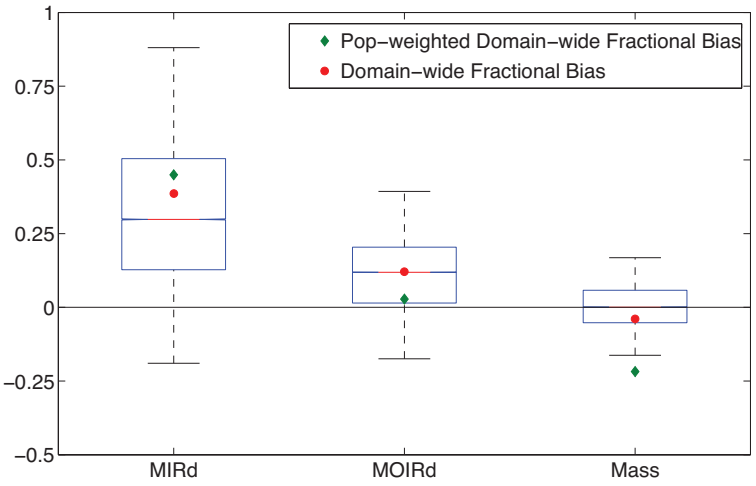

Figure 2.9: FB statistics from the entire episode compare the effec- tiveness of each reactivity-based substitution to the null and base cases. The diamond and circle represent the DWFB (Eq. 2.11) and PWDWFB (Eq. 2.12), respectively. Statistics are given for the difference of a case from base divided by the negative difference of the null case from base for every cell not entirely over water at each time the base concentration is greater than 50 ppb ozone (Eq. 2.8). The line at the box center represents the median value, the edges of the box the IQR, and the whiskers the extreme values within 1.5 times the IQR. Interpretation of the values is delineated in Section 3.2.

much more slightly than the MIRd test scenario. For the MOIRd test case, the population-weighted domain-wide fractional bias is very close to zero (0.03), exhibiting that potential population exposure is hardly increased above that in the base case even though a substantial increase in emissions has occurred in terms of mass. Together, these results suggest that the MOIR scale is more appropriate than the MIR scale for this domain and episode.

The mass-equivalent test scenario has a slightly negative domain-wide fractional bias of -0.04, which supports the conclusion that equivalent mass of less reactive substances produces lower ozone concentrations than more highly reactive substances. The population-weighted DWFB for the mass substitution is -0.22, which shows that replacing highly reactive VOCs with less reactive VOCs generally leads to ozone reductions, particularly in populated regions.

Comparison of the regions where ozone may increase when using MIR- or MOIR-based substitutions reveals that these regions are most sensitive to NO_x controls, and, conversely,

areas where reactivity based substitutions lead to ozone reductions or little change is where NO_x reductions can lead to ozone increases (Figure 2.3, 2.7). This result suggests that reactivity-based controls complement NO_x controls.

2.4 Conclusions

To investigate important questions regarding the application of reactivity scales for ozone management purposes, three-dimensional chemical transport modeling of six different solvent test scenarios was executed. Scenarios tested the substitution of the more reactive constituents of solvent emissions (i.e., toluene, xylene, and 2-butoxyethanol) with the much less reactive 2-methylheptane and n-butyl acetate as surrogate compounds. The primary hypotheses examined were whether uses of reactivity-based test scenarios affect the ozone concentration downwind of the area in which they are applied and which reactivity scales are more appropriate in areas where intercity transport is significant. Both near-field and downwind impacts of the substitutions were investigated.

Results of modeling the equal mass test scenario support the conclusion that more reactive compounds will produce greater concentrations of ozone than would an equivalent emission, in terms of mass, of a lower reactivity compound (Figures 2.5, 2.6, 2.7, and 2.8). As such, substituting lower reactivity compounds can provide benefits similar to reducing VOC mass, which forms the basis for using reactivity weighting for regulatory purposes. Additional support for this conclusion is given by the MOIRd test scenario, which showed increased mass of emissions resulting in slight increases and decreases from base concentrations of ozone, with almost negligible change in potential population exposure. This premise is at the core of reactivity-based VOC control and has been supported in the literature.

A variety of reactivity-based scales have been developed to facilitate implementation, and the two scales assessed have demonstrated distinct behavior within the study. The MIRd test scenario increased the emitted mass by more than 60%, but resulted in hourly and

8-hour maximum ozone concentrations greater than the base scenario by as much as 4 ppb and 2.4 ppb, respectively. These increases were even evident downwind of the test scenario in which the MIR-based substitution was executed only in the NY-NJ-CT nonattainment area. Alternately, the MOIRd test replaced the more reactive VOCs with 20% more mass, but hourly and 8-hour maximum ozone deviations from the base case fluctuated between positive and negative. The distinction between these two test scenarios provides reason for reactivity scales to be selected judiciously.

As reductions of population exposure are generally considered a benefit, the argument could be made for requiring a very conservative reactivity scale or refusing reactivity-weighting altogether. Both would lead to taking potentially beneficial, cost effective controls out of consideration. Disregarding reactivity could lead to substitutions that would have a net disbenefit on ozone, particularly in the more urban areas. The ultimate choice of scale should take into account other programs and controls under consideration. As seen here, the MIR test scenarios actually lead to decreases in some urban centers but has more widespread increases. Most of the larger relative increases occur in areas where NO_x controls are most effective as demonstrated for August 12. Using reactivity-based substitutions (e.g., with either the MIR- or MOIR-based scaling) in combination with NO_x controls has the potential to provide regionally lower ozone in a cost effective fashion.

CHAPTER III

ANISORROPIA: THE ADJOINT OF ISORROPIA

This chapter presents the development of ANISORROPIA, the discrete adjoint of the ISORROPIA thermodynamic equilibrium model that treats the Na^+-SO_4^{2-}-HSO_4^--NH_4^+-NO_3^--Cl^--H_2O aerosol system, and we demonstrate its sensitivity analysis capabilities. ANISORROPIA calculates sensitivities of an inorganic species in aerosol or gas phase with respect to the total concentrations of each species present with less than a two-fold increase in computational time over the concentration calculations. Due to the highly nonlinear and discontinuous solution surface of ISORROPIA, evaluation of the adjoint required a new, complex-variable version of the model, which determines first-order sensitivities with machine precision and avoids cancellation errors arising from finite difference calculations. The adjoint is verified over an atmospherically relevant range of concentrations, temperature, and relative humidity. We apply ANISORROPIA to recent field campaign results from Atlanta, GA, USA, and Mexico City, Mexico, to characterize the inorganic aerosol sensitivities of these distinct urban air masses. The variability in the relationship between $PM_{2.5}$ mass and precursor concentrations shown has important implications for air quality and climate.

This chapter published as: Capps, S. L., D. K. Henze, A. Hakami, A. G. Russell, and A. Nenes (2011), ANISORROPIA: the adjoint of the aerosol thermodynamic model ISORROPIA, Atmospheric Chemistry and Physics, 12, 21789-21834, doi:10.5194/acp-12-527-2012.

3.1 Introduction

Atmospheric chemical transport models (CTMs) are used for many purposes including assessment of radiative climate forcing of aerosol (*Forster et al.*, 2007) and evaluation of the effectiveness of emissions control strategies designed to reduce exposure of humans to particulates (*US Environmental Protection Agency*, 2004). The accuracy of these estimates is limited by model representations of chemical and physical processes as well as model parameters (e.g., emissions rates). Attributing climate forcing and air quality degradation to sources is challenging with sensitivity analysis techniques based on standard model output (*Shindell et al.*, 2008, 2009). Inorganic species, primarily sulfate ($SO^{2-}_{4(p)}$/$HSO^{-}_{4(p)}$), ammonium ($NH^{+}_{4(p)}$), nitrate ($NO^{-}_{3(p)}$), sodium ($Na^{+}_{(p)}$), and chloride ($Cl^{-}_{(p)}$), constitute a significant fraction of dry aerosol mass (*Heintzenberg*, 1989). The nonlinear formation of inorganic aerosol from gas phase precursors is reasonably well-characterized (*Nenes et al.*, 1999). However, the precision of emissions estimates of aerosol precursors varies widely depending upon source type and region of the world (*Klimont and Streets*, 2007). Adjoint-based sensitivity analysis enhances the ability to assess the relative influence of aerosol precursor emissions on air quality metrics and aerosol radiative forcing of climate as well as providing a means of refining emissions estimates with observations in an inverse modeling framework.

The highly variable sensitivity of fine mode ammonium-sulfate-nitrate aerosol to precursor concentrations (*Ansari and Pandis*, 1998; *West et al.*, 1999) makes the robust assessment of emissions influences challenging. *West et al.* (1998) demonstrated climatic implications of this variability by quantifying the marginal direct radiative forcing of inorganic aerosols. *Vayenas et al.* (2005) explored the relationship of $SO_{2(g)}$ and $NO_{x(g)}$ emissions to SO^{2-}_{4}-HSO^{-}_{4}-NH^{+}_{4}-NO^{-}_{3} aerosol concentrations in an observationally driven Eulerian model over the eastern United States, finding significant variation in effectiveness of controls because of the nonlinear transformation of gaseous precursors to aerosol. *Pinder et al.* (2007) demonstrated the efficiency of reducing $NH_{3(g)}$ emissions relative to

$SO_{2(g)}$ and $NO_{x(g)}$ for air quality objectives with the PM-CAMx CTM (*Gaydos et al.*, 2007) by perturbing emissions of $NH_{3(g)}$, $SO_{2(g)}$, and $NO_{x(g)}$ by fifty percent. Although the finite difference approach employed in this and other studies, sometimes termed "emissions toggling", is the most straightforward sensitivity analysis technique, it is limited in that computational requirements scale with the number of emissions investigated; perturbations to the atmospheric conditions from the changed emissions obscure nonlinear effects; and cancellation errors limit the accuracy of this method. The decoupled direct method (DDM), an implementation of a tangent linear model (TLM), can be used to understand the impact of selected emissions on the field of air quality or health metrics without changing emissions parameters (*Dunker*, 1984; *Napelenok et al.*, 2006; *Koo et al.*, 2007); second-order source-oriented sensitivities of inorganic aerosol can now quantify nonlinear contributions to sensitivity (*Zhang et al.*, 2012b). Establishing the source-receptor relationship of inorganic aerosol by these forward sensitivity analysis methods (i.e., emissions toggling, DDM/TLM) reveals emissions impacts of particular sources on the field of concentrations. Source-oriented sensitivity analysis is less helpful for evaluating relative impacts of emissions, and inverse modeling with source-oriented sensitivities is limited in application due to computational cost, which scales with model parameters assessed (*Mendoza-Dominguez and Russell*, 2001).

The adjoint method complements forward sensitivity approaches by efficiently elucidating the relationship of model output (e.g., specified concentrations, air quality metrics) to the field of model parameters, or input, (e.g., emissions, initial conditions) without perturbing model inputs. Computational requirements for calculation of these receptor-oriented sensitivities are insensitive to the number of model parameters investigated. Thus, adjoints can efficiently calculate sensitivities of air quality or climate-forcing metrics with respect to a vast number of parameters (e.g., 10^5) in accordance with model chemistry and physics. This receptor-oriented approach facilitates optimization of model parameters in accordance with observations in a 4-dimensional variational (4D-Var) data assimilation framework.

Meteorologists have exploited adjoints for optimization of initial conditions and other parameters for decades (*Sasaki*, 1958; *Marchuk*, 1974; *Lamb et al.*, 1975; *Talagrand*, 1981; *Talagrand and Courtier*, 1987). CTM adjoints have been used to explore relationships of concentrations of gaseous species and emissions (*Menut et al.*, 2000; *Vukićević and Hess*, 2000; *Sandu et al.*, 2005a; *Hakami et al.*, 2006; *Martien and Harley*, 2006) and to refine estimates of trace gases in the atmosphere (*Fisher and Lary*, 1995; *Elbern et al.*, 1997; *Kaminski et al.*, 1999; *Elbern et al.*, 2000; *Muller and Stavrakou*, 2005; *Zhang et al.*, 2008; *Kopacz et al.*, 2009). Gas phase 4D-Var data assimilation has been employed to improve agreement of model predictions with in situ observations (e.g., *Chai et al.*, 2006) or remote sensing (e.g., *Resler et al.*, 2010). *Kukkonen et al.* (2011) anticipate the utility of 4D-Var data assimilation of trace gas observations within a coupled meteorological-chemical forecasting model framework for real-time improvement of air quality forecasting.

Application of adjoint methods to study aerosols is relatively new, likely due, in part, to the difficulty of developing adjoints of aerosol models as well as recent attention to refining aerosol concentration estimates in CTMs. *Henze et al.* (2004) and *Sandu et al.* (2005b) demonstrated the feasibility of developing an adjoint for the coagulation and growth of a multi-component aerosol population in a 0-D model. *Hakami et al.* (2005) first optimized initial and boundary conditions as well as emissions rates of non-reactive black carbon (BC) aerosol using an adjoint of the STEM-2k1 model (*Carmichael et al.*, 2003; *Sandu et al.*, 2005a) to assimilate in situ observations from ACE-Asia (*Heubert et al.*, 2003; *Seinfeld et al.*, 2004). The adjoint of GOCART, a global aerosol transport model, demonstrated the utility of satellite-based aerosol observations for constraining highly uncertain aerosol emissions parameters (*Dubovik et al.*, 2008). The distribution and long-range transport of Asian dust have been investigated with a 4D-Var data assimilation version of a regional dust transport model (RC4) with both in situ and remotely sensed observations (*Yumimoto et al.*, 2007, 2008; *Uno et al.*, 2008; *Sekiyama et al.*, 2010). The direct and albedo forcings of black carbon deposited on the Tibetan Plateau were characterized by *Kopacz et al.* (2011)

with the adjoint of GEOS-Chem. *Henze et al.* (2007) first included secondary formation of inorganic aerosol in the adjoint of GEOS-Chem using MARS-A, a thermodynamic model of the SO_4^{2-}-HSO_4^--NH_4^+-NO_3^--H_2O aerosol system (*Binkowski and Roselle*, 2003). With this framework, *Henze et al.* (2009) conducted inverse modeling of inorganic fine mode aerosol observations from the IMPROVE network (*Malm et al.*, 1994) to identify influences of aerosol precursor emissions on US air quality.

Many regional and global CTMs employ ISORROPIA/ISORROPIA-II (*Nenes et al.*, 1998, 1999; *Fountoukis and Nenes*, 2007), a thermodynamic equilibrium model. ISORROPIA treats the Na^+-SO_4^{2-}-HSO_4^--NH_4^+-NO_3^--Cl^--H_2O aerosol system by efficiently and accurately calculating the partitioning of precursor gases and water vapor to aerosol at a specified temperature and relative humidity (RH). ISORROPIA simulates secondary inorganic aerosol formation in CHIMERE (*Schmidt et al.*, 2001; *Bessagnet et al.*, 2004), Community Multiscale Air Quality model (CMAQ) (*Byun and Schere*, 2006), Comprehensive Air Quality Model with Extensions (CAMx) (*ENVIRON*, 1997, 2010), COSMO-ART (*Vogel et al.*, 2009), GEOS-Chem (`http://geos-chem.org/`) (*Bey et al.*, 2001; *Pye et al.*, 2009), LOng Term Ozone Simulation–EURopean Operational Smog model (LOTOS-EUROS) (*Schaap et al.*, 2008), and the Sulfur Transport dEposition Model (STEM-2k1) (*Carmichael et al.*, 2003). Although ISORROPIA is capable of treating the entire water uptake curve, CTMs neglect the formation of solid phases and assume aerosol exist in a metastable state.

Receptor-oriented sensitivity analysis and inverse modeling have been limited to gaseous species or inert aerosol for CTMs that employ ISORROPIA due to the absence of its adjoint, which this work addresses. We present the development of ANISORROPIA (AdjoiNt of ISORROPIA) (Section 3.2), demonstrate its accuracy at atmospherically relevant conditions (Section 3.3), and apply it to examine observed aerosol mixture responses (Section 3.4). Finally, the utility of ANISORROPIA within adjoints of CTMs is anticipated (Section 3.5).

3.2 Methods

The adjoint of a CTM determines sensitivities of a metric of specified output parameters (e.g., air quality attainment metric) with respect to a wide array of input parameters (i.e., emissions rates). Conceptually, an infinitesimal variation in a single output variable evolves backwards through modeled processes, indicating the corresponding perturbations of input parameters required to effect the infinitesimal change in output. Realizing this capability in a CTM with an online simulation of aerosol involves considerable methodological and coding development. Outlined in the following sections are the role of ISORROPIA in CTMs (Section 3.2.1), the framework for adjoint-based sensitivity analysis (Section 3.2.2), and the specific tactics employed to develop ANISORROPIA (Section 3.2.3).

3.2.1 The ISORROPIA model

Key components of fine mode aerosol are water, inorganic salts, crustal minerals, organics, and trace metals (*Seinfeld and Pandis*, 2006b). Inorganic species constitute about 25–50 % of the dry mass of a typical continental particle, the most abundant being sulfate ($SO^{2-}_{4(p)}$/$HSO^{-}_{4(p)}$), ammonium ($NH^{+}_{4(p)}$), and nitrate ($NO^{-}_{3(p)}$). Sodium ($Na^{+}_{(p)}$) and chloride ($Cl^{-}_{(p)}$) ions contribute significantly in environments with marine character or near dry lake beds (*Heintzenberg*, 1989). CTMs often treat fine mode particles as existing in thermodynamic equilibrium with the surrounding gases based on the short equilibration time scales for these particles (*Ansari and Pandis*, 1999a; *Dassios and Pandis*, 1999; *Fountoukis et al.*, 2009).

A number of thermodynamic models have been developed to model aerosol thermodynamic equilibrium with varying degrees of comprehensiveness, accuracy, and efficiency (e.g., AIM (*Clegg et al.*, 1998); GFEMIN (*Ansari and Pandis*, 1999b); EQSAM3 (*Metzger et al.*, 2006; *Metzger and Lelieveld*, 2007); EQUISOLV II (*Jacobson and Tabazadeh*, 1996; *Jacobson*, 1999); ISORROPIA and ISORROPIA II (*Nenes et al.*, 1998, 1999; *Fountoukis and Nenes*, 2007); MARS-A (*Saxena et al.*, 1986; *Binkowski and Roselle*, 2003); MESA

(*Zaveri et al.*, 2005); SCAPE2 (*Kim et al.*, 1993a,b; *Meng and Seinfeld*, 1996); UHAERO (*Amundson et al.*, 2006)).

Until now, the adjoint of one thermodynamic equilibrium model has been developed: RPMARES, an implementation of the MARS-A model for GEOS-Chem (*Binkowski and Roselle*, 2003; *Park et al.*, 2004; *Henze et al.*, 2007). RPMARES treats the ammonium-sulfate-nitrate aerosol system with temperature-independent activity coefficients based on the Pitzer model for binary coefficients. ISORROPIA treats two additional species, sodium and chloride, and includes temperature dependence when calculating activity coefficients by the Kusik-Meissner (K-M) method. K-M compares well with experimental results as does Pitzer but also continues to produce physically reasonable results at higher ionic strengths (i.e., greater than 30 molar) (*Harvie et al.*, 1984; *Cohen et al.*, 1987; *Kim et al.*, 1993b). In ISORROPIA, water uptake is calculated in accordance with AIM Model III (`http://www.aim.env.uea.ac.uk/aim/aim.php`) rather than older data sets (*Binkowski and Roselle*, 2003; *Fountoukis and Nenes*, 2007). Inclusion of additional species, increased accuracy compared to RPMARES, and widespread utilization of ISORROPIA in CTMs motivated development of ANISORROPIA.

ISORROPIA solves the aerosol-gas partitioning problem in two different modes: forward and reverse. Model input for the forward mode is the total amount of species present in the gas and aerosol; it outputs the gas phase and aerosol concentrations of each of the species. The reverse mode requires the concentration of species in the aerosol and calculates gas phase concentrations of species in equilibrium. The focus of the current work is the forward mode as it is more widely employed. The reverse mode is useful for aerosol dynamics codes with active mass transfer of aerosol species (e.g., *Capaldo et al.*, 2000; *Pilinis et al.*, 2000; *Kelly et al.*, 2010).

ISORROPIA uses ten distinct algorithms to determine equilibrium based on the relative

abundance of negatively and positively charged ionic species for the NH_4^+-SO_4^{2-}-HSO_4^--NO_3^--Na^+-Cl^--H_2O aerosol system. The sulfate ratio, $R_S = \frac{[\text{Total NH}_3]+[\text{Total Na}]}{[\text{Total H}_2\text{SO}_4]}$, determines which solution branch is employed. For $R_S \geq 2$, the neutralized solution regime is accessed since sufficient ammonium and sodium are present to neutralize the aerosol sulfate. $R_S<2$ invokes one of the seven acidic solution algorithms. Discretization of the solution space reduces the computational complexity and increases efficiency of determining equilibrium of a multicomponent system; therefore, ANISORROPIA was designed to be congruent with the underlying model.

3.2.2 Mathematical background

Adjoint-based sensitivity analysis complements the direct decoupled method of sensitivity analysis more often employed in three-dimensional CTMs. Because of the relatively novel application of adjoint methods to CTMs and their internal models, the mathematical basis for the discrete adjoint of the forward mode of ISORROPIA is given. A comprehensive description of the mathematical framework for discrete and continuous adjoints of CTMs can be found in *Sandu et al.* (2005a).

Forward mode ISORROPIA partitions concentrations of inorganic species summed over solid, liquid, and gas phases into the appropriate concentration in each phase at thermodynamic equilibrium. ISORROPIA can be represented as a function, F, that propagates the total concentration, c_i^t, to the appropriate phase concentrations, c_i^p, for each species, i (Eq. 3.1). The vectors $\vec{c^p}$ and $\vec{c^t}$ represent all species.

$$\vec{c^p} = F(\vec{c^t}) \tag{3.1}$$

A scalar response function, $\mathcal{J}$, of the model is given by

$$\mathcal{J}(\vec{c^t}) = g(\vec{c^p}) \tag{3.2}$$

The derivatives of the response function, $\mathcal{J}$, with respect to the total concentrations, $\vec{c^t}$, are desired. A infinitesimal perturbation, $\delta\vec{c^t}$, in $\vec{c^t}$ propagates to $\delta\vec{c^p}$ by the tangent linear

model (Eq. 3.3).

$$\delta\vec{c^p} = F' \circ \delta\vec{c^t} \tag{3.3}$$

An adjoint operator, denoted by F'^* here, corresponds to the tangent linear operator such that

$$\vec{\lambda^t} = F'^* \circ \vec{\lambda^p} + \phi. \tag{3.4}$$

Thus, adjoint vectors, $\boldsymbol{\lambda^p}$, corresponding to $\boldsymbol{c^p}$, and a forcing function, ϕ, are propagated to $\boldsymbol{\lambda^t}$. Appropriate selection of the values of $\vec{\lambda^p}$ and ϕ allow the desired result,

$$\lambda_i^t = \frac{\partial[\mathcal{J}(\vec{c^t})]}{\partial c_i^t} = \frac{\partial[g(\vec{c^p})]}{\partial c_i^t} \tag{3.5}$$

The discrete adjoint model, F'^*, which is ANISORROPIA, maintains the algorithmic structure of the original function, F, or ISORROPIA. ANISORROPIA can produce the derivatives of interest independently, as demonstrated in this work. It could also be integrated into the adjoint of a CTM to propagate adjoint vectors through the processes described by ISORROPIA. Branching and discontinuity (not unique to ISORROPIA, as theoretically any code containing "GO TO", "IF", "MAX/MIN", "ABS" and other similar functions introduce branching and discontinuities), does not prohibit the development of a (discrete) adjoint, because a continuous set of solutions and derivatives can be derived for each subdomain of the code. This is not the case for sensitivities evaluated with other methods (e.g., finite differences), as they can frequently involve function evaluations across solution regimes and thus provide fundamentally inaccurate values.

3.2.3 Development of ANISORROPIA

Accumulation of adjoint sensitivities occurs through a set of calculations which parallel the original model; a model adjoint can be formed in one of two ways. If the governing equations are differentiated and then transformed into a numerical algorithm, the adjoint is termed a continuous adjoint; the algorithmic treatment of a continuous adjoint model may differ significantly from the original model. Conversely, a discrete adjoint is formed by

the differentiation of the forward model in accordance with the original model algorithm. Automatic differentiation (AD) tools, which apply the chain rule of derivative calculus line by line, can be efficiently employed as aids to discrete adjoint development (`http://www.autodiff.org/`); alternately, the discrete adjoint can be developed by manually processing the code line by line.

A discrete adjoint is developed to maintain consistency with ISORROPIA and to retain the efficiency of ISORROPIA, which largely arises from the discretization of the solution space. ANISORROPIA has been developed for each of the ten solution regimes involved in the forward mode for the deliquesced NH_4^+-SO_4^{2-}-HSO_4^--NO_3^--Na^+-Cl^--H_2O aerosol system. The appropriate solution regime is accessed according to the relative abundance of total species present. An internal driver calls the appropriate adjoint routine based on the acidity of the aerosol, which is consistent with that executed by the forward model. ANISORROPIA does not checkpoint, or store to a file, the solution regime called during the forward execution of ISORROPIA because a simple arithmetic calculation from input to ANISORROPIA is sufficient to select the appropriate solution pathway.

Within each of the ten solution pathways, ISORROPIA remains sufficiently complex that writing the adjoint of this FORTRAN code by hand would be very challenging. The high degree of interdependence in addition to the length of the code ($\sim$10 000 lines) made employing an AD tool an attractive alternative. TAPENADE, an AD tool for FORTRAN and C programs (*Hascoët and Pascual*, 2004), was used to apply the chain rule of derivative calculus line by line such that derivatives of dependent variables with respect to intermediate variables can accumulate through this adjoint model in accordance with an adjoint forcing vector to produce the sensitivity of a dependent-variable with respect to independent variables (`http://www.autodiff.org/`). ISORROPIA originally calculated activity coefficients to single-precision; development of ANISORROPIA required conversion of all variables to double-precision to accumulate sensitivities through this aspect of the model accurately.

ANISORROPIA input includes total concentrations, temperature, and RH as well as the adjoint forcing vector, the elements of which correspond exactly to the output arrays of ISORROPIA (i.e., aqueous and gaseous partitioned-species concentrations). In ANISORROPIA execution, branches and iterations are noted with inexpensive variable accumulation, and variable values are temporarily stored in memory during the forward calculations (Fig. 3.1, blue lines); then, the same procedures are executed in reverse order while accumulating gradients in corresponding sensitivity calculations driven by the forcing vector (Fig. 3.1, orange lines). Thus, ANISORROPIA produces partial derivatives of the output species indicated in the forcing vector with respect to each input concentration (i.e., sum of aqueous and gaseous species concentration). If the adjoint forcing vector is null except for a single element equal to unity, ANISORROPIA produces the row of the Jacobian of ISORROPIA corresponding to the element equal to unity; for instance, if the element of the adjoint forcing vector corresponding to $[\mathrm{NH}^+_{4(\mathrm{aq})}]$ is unity and all others zero, ANISORROPIA produces the array $\frac{\partial[\mathrm{NH}^+_{4(\mathrm{aq})}]}{\partial[\mathbf{X}]}$, where $[X]$ is the array of concentrations of the sum of the aqueous and gaseous forms of species X, one of the total species tracked by ISORROPIA. Forward sensitivity analysis methods produce the column of the Jacobian corresponding to a selected $[Y]$; hence, a single execution of a forward sensitivity analysis method could yield the array $\frac{\partial[\mathbf{Y}]}{\partial[\mathrm{Total\ H_2SO_4}]}$, where $[\mathbf{Y}]$ is the array of concentrations of partitioned species, Y. In this way, the Jacobian produced by ANISORROPIA is compared directly to that determined by a forward sensitivity analysis method for model evaluation (Section 3.3.2).

For acidic cases (i.e., $R_S<2$), ISORROPIA iteratively resolves activity coefficients to convergence. The iterative nature of the forward solution is maintained in the adjoint of the acidic cases (Fig. 3.1a). Straightforward manipulation of ISORROPIA code was required to indicate which sensitivities should be traced by TAPENADE. The only modification to the forward solution is to increase the precision with which activity coefficients are calculated by default so that accurate sensitivity calculations can be obtained.

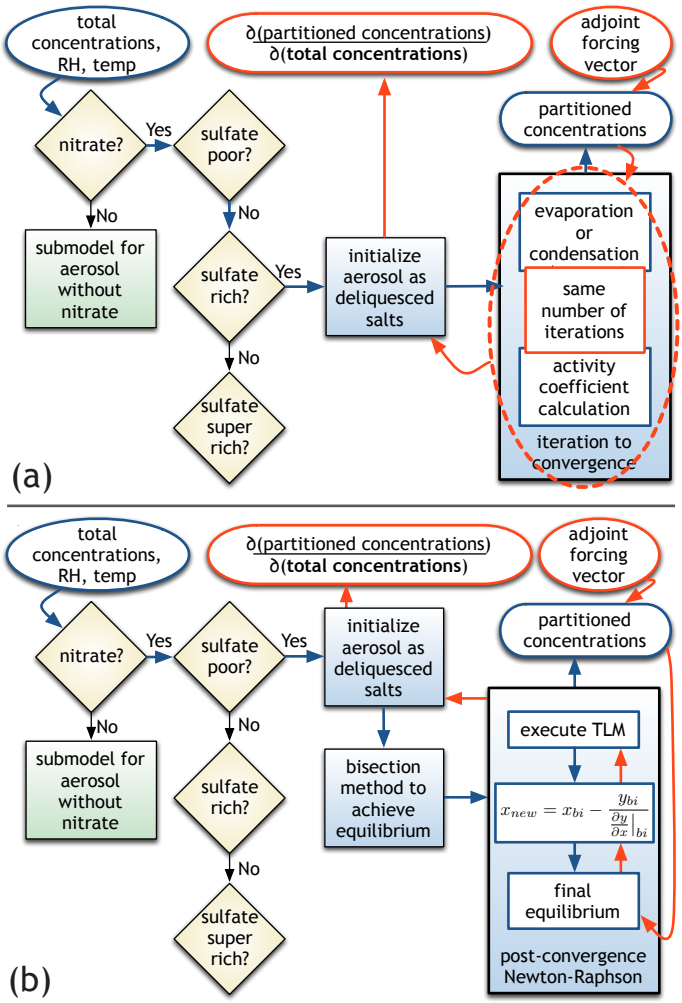

Figure 3.1: Algorithmic flowchart of ISORROPIA forward (blue) and adjoint (orange) calculations. **(a)** The acidic aerosol solution algorithm is given for the cases where the molar ratio of positive ions (i.e., total ammonia and sodium) to total sulfate is less than two (R_S<2); **(b)** for $R_S \geq 2$, the neutralized aerosol solution algorithm is shown.

In the case of neutralized aerosol (i.e., $R_S \geq 2$), ISORROPIA evaluates whether equilibrium has been achieved by a selected saturation ratio. For instance, in the NH_4^+-SO_4^{2-}-HSO_4^--NO_3^--H_2O aerosol system, all equations are solved successively so that only one equilibrium needs to be numerically solved, namely $NH_{3(g)}$+$H_2O_{(aq)} \rightleftharpoons NH^+_{4(aq)}$+$OH^-_{(aq)}$; therefore, satisfactory equilibrium is achieved when $\frac{[NH^+_{4(aq)}][OH^-_{(aq)}]}{K[NH_{3(g)}]} = 1$, where, for example, $[NH^+_{4(aq)}]$ denotes the concentration of ammonium in mol m^{-3} and K denotes the relevant equilibrium constant. Across the range of potential partitioned concentrations, the

saturation ratio closely approximates the behavior of a step function owing to the very large change in species partitioning with small shifts in pH. The stability of the bisection method ensures convergence to the root of $\frac{[\mathrm{NH}^+_{4(\mathrm{aq})}][\mathrm{OH}^-_{(\mathrm{aq})}]}{K[\mathrm{NH}_{3(\mathrm{g})}]} = 1$ in ISORROPIA. The discontinuous nature of this algorithm required modification of the underlying model in order for sensitivities to be traced through the solution. For $R_S \geq 2$ in the NH_4^+-SO_4^{2-}-HSO_4^--H_2O aerosol system, a stable method of iterating to convergence of activity coefficients, as employed for $R_S < 2$ cases, was developed. For the neutralized cases in the NH_4^+-SO_4^{2-}-HSO_4^--NO_3^- and NH_4^+-SO_4^{2-}-HSO_4^--NO_3^--Na^+-Cl^--H_2O aerosol systems, the post-convergence Newton-Raphson (N-R) method was implemented (*Bartholomew-Biggs*, 1998) (Fig. 3.1b). Gradients required by N-R are calculated with TAPENADE-produced TLMs of the function being treated by bisection; that is, the chain rule is applied line-by-line to produce the sensitivity of the equilibrium equation of interest (e.g., $\frac{[\mathrm{NH}^+_{4(\mathrm{aq})}][\mathrm{OH}^-_{(\mathrm{aq})}]}{K[\mathrm{NH}_{3(\mathrm{g})}]} = 1$) with respect to its input (e.g., moles of $NH_{3(g)}$ partitioning to the aerosol). The result of bisection serves as the initial guess of one iteration of the N-R method. By adding a differentiable calculation subsequent to the original algorithm, the stability of the bisection algorithm is maintained while providing the functionality necessary for adjoint calculations. It is sufficient to take the adjoint of this single step (*Bartholomew-Biggs*, 1998). The error system of ISORROPIA is augmented to note when the N-R calculation causes significant deviation from the bisection result. The forward and adjoint codes return this flag to the host model so that the thermodynamic partitioning of the select time step and grid cell can be consistently dismissed in concentration and sensitivity calculations.

3.3 Evaluation of ANISORROPIA

A two-part evaluation of ANISORROPIA was conducted. First, the partitioned concentrations given by ANISORROPIA were evaluated against ISORROPIA v.2.1 for an atmospherically relevant range of RH (5–95 %), temperature (268–308 K), and total concentrations to ensure that the forward calculations are not altered by the modifications of the code

required to calculate the adjoint derivatives. Total concentrations ranges were 1–50 μg m^{-3} H_2SO_4; 0.2–9 μg m^{-3} NH_3; 0–16 μg m^{-3} HNO_3; 0–18 μg m^{-3} Na; and 0–30 μg m^{-3} HCl. Approximately 65 000 sets of model input were evaluated, and ANISORROPIA processed 90 % without producing an error code (Fig. 3.2). The stiffness of the numerical solution for equilibrium at high ionic concentrations due to the metastable assumption sometimes leads to insufficient convergence for accurate adjoint sensitivity calculation causing an error. Errors can also arise from the post-convergence N-R step altering the equilibrium achieved by bisection. Optimal values for the ionic threshold (increased to 200 from the value of 100 used in ISORROPIA) and acceptable range for N-R deviation (unique to ANISORROPIA) were determined by extensive error assessment. For the convergent cases, ANISORROPIA concentrations are less than 0.1 % different than results of the modified ISORROPIA v2.1 (Fig. 3.2, $R^2 = 1.00$). Having ensured that the sensitivities would be evaluated for nearly identical simulated equilibrium concentrations, the accuracy of the adjoint sensitivities was assessed by comparison to sensitivities calculated using the complex variable method.

3.3.1 The complex variable method

The truncated Taylor series expansion of $F(x)$ about a point (x_0) leads to the central finite difference approximation of $\frac{\partial F}{\partial x}$ with truncation error $O(h^2)$ given by

$$\frac{\partial F}{\partial x} = \lim_{h \to 0} \frac{F(x_0 + \frac{1}{2}h) - F(x_0 - \frac{1}{2}h)}{h} \tag{3.6}$$

where F is a real analytic function and h is a small, real perturbation. *Lyness and Moler* (1967) demonstrated that complex numbers are useful for numerical approximation of derivatives. Computational costs of their approach, which was based on Cauchy's integral theorem, limited application of the technique (*Lantoine et al.*, 2010). *Squire and Trapp* (1998) developed an efficient complex step differentiation method which maintains machine precision in the derivative. For the complex analytic function $G(z)$, where z is a complex argument, an analogous expression for $\frac{\partial G}{\partial z}$ with approximation error $O(h^2)$ arises:

$$\frac{\partial G}{\partial z} = \lim_{h \to 0} \frac{\Im[G(z_0 + ih)]}{h} \tag{3.7}$$

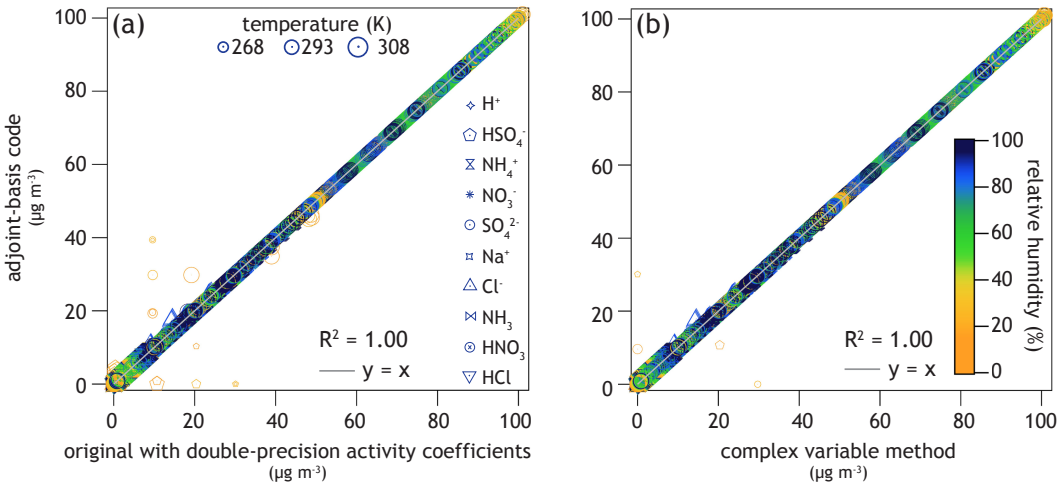

Figure 3.2: Evaluation of concentrations of aqueous species in $\mu g\,m^{-3}$ produced by forward model augmented for adjoint development against **(a)** ISORROPIA v.2.1 with a modified double-precision activity coefficient module and **(b)** the complex variable method version of ISORROPIA v.2.1 with double-precision activity coefficient module. The atmospherically relevant range of concentrations, RH, and temperature evaluated is given in Section 3.3 of the text. In each case, the intercept and slope of the linear regression were negligibly different than 0 and 1, respectively.

where $i = \sqrt{-1}$ and $\Im$ selects the imaginary part of the argument (*Squire and Trapp*, 1998). The complex variable method (CVM) as introduced by *Squire and Trapp* (1998) eliminates subtraction cancellation and numerical round-off errors, the primary difficulties of numerical differentiation (*Lyness and Moler*, 1967).

To implement CVM in a FORTRAN-based numerical model such as ISORROPIA, variables are declared as COMPLEX rather than REAL, and intrinsic functions are modified to treat complex arguments (*Giles and Pierce*, 2000). This conversion is straightforward with the exception of the functions that must be approximated to accept COMPLEX arguments, such as the arccosine function, ACOS. ACOS is called within the analytical solution of the cubic polynomial $x^3 + A_1x^2 + A_2x + A_3 = 0$. CVM maintains the sensitivity information for variables in their imaginary part; thus, complex variables must be altered commensurately in the real and imaginary parts. Setting the total derivative to zero, $df = \frac{\partial f}{\partial x}\Big|_{x=x_0} dx + \sum_{i=1}^{3} \frac{\partial f}{\partial A_i}\Big|_{x=x_0} dA_i = 0$, where x_0 is the desired solution of the cubic polynomial, A_i represents the coefficients of the polynomial, $dx = \Im(x_0)$,

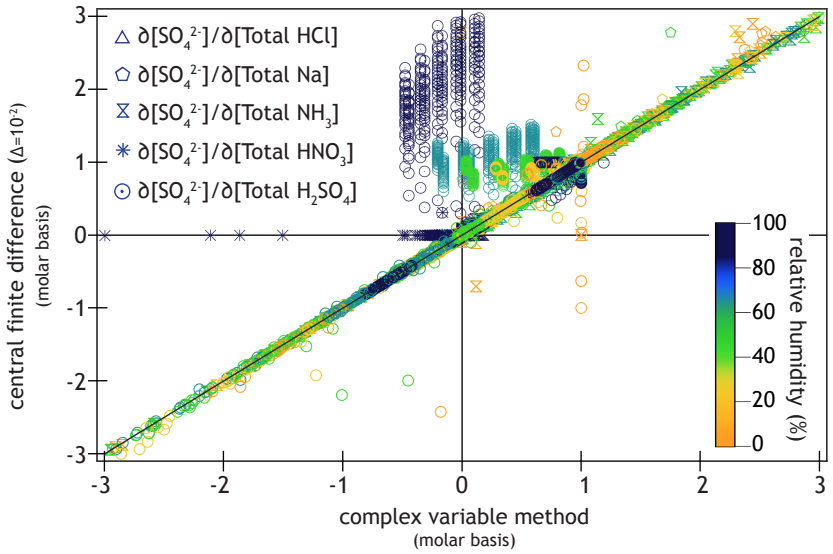

Figure 3.3: Sensitivities from the central finite difference method with a delta value of 10^{-2} compared against sensitivities from the complex variable method with a perturbation of $10^{-18}i$. The line $y = x$ is plotted for reference (solid black). Deviations from stoichiometric expectations in finite difference sensitivities revealed that the finite difference approach would not suffice to evaluate ANISORROPIA sensitivities.

and $dA_i = \Im(A_i)$, yields $\frac{\partial x_0}{\partial A_i} = \frac{\Im(x_0)}{\Im(A_i)}$. Rather than using an alternate analytical solution to avoid calling ACOS, the imaginary part of x_0 was calculated independently. To do so, $\Im(A_i)$ were stored, and the desired real root calculated by the original function operating only on the real parts of A_i. The analytical total derivative of the cubic polynomial gives

$$\Im(x_0) = \frac{-(x_0^2)\Im(A_1) - (x_0)\Im(A_2) - \Im(A_3)}{3x_0^2 + 2A_1x_0 + A_2} \tag{3.8}$$

by which $\Im(x_0)$ is obtained. This strategy is readily applicable in other CVM applications to similar calculations involving functions that must be approximated to treat a complex argument.

3.3.2 Sensitivity comparison

Although the accuracy of finite difference sensitivities is limited by round-off error, nonlinear effects, and solution discontinuities, these provide the most straightforward method of evaluating partial derivatives calculated by adjoints (Giles and Pierce, 2000); therefore, adjoint-based sensitivities are typically compared to those from the central finite difference

method (e.g., *Martien et al.*, 2006; *Henze et al.*, 2007; *Hakami et al.*, 2007). The highly nonlinear, discontinuous solution surface of ISORROPIA and associated subtraction cancellation errors rendered this method ineffective. For example, finite difference sensitivities of aqueous sulfate to total sulfate exceeded stoichiometric expectations for the same input for which the CVM found reasonable sensitivities (Fig. 3.3). To overcome this issue, CVM is used for evaluation of ANISORROPIA sensitivities.

The adjoint sensitivities from ANISORROPIA are compared to those from CVM over the same evaluation range which was employed for the concentrations described in Section 3.3 (Fig. 3.4). Thirty-five sensitivities of the aerosol concentration (model output: $Cl^-_{(aq)}$, $H^+_{(aq)}$, $HSO^-_{4(aq)}$, $Na^+_{(aq)}$, $NH^+_{4(aq)}$, $NO^-_{3(aq)}$, $SO^{2-}_{4(aq)}$) to the sum of gaseous and aerosol concentrations (model input: total chloride, total nitrate, total sulfate, total ammonium, and total sodium) were evaluated for each of the aqueous aerosol species with respect to each aerosol precursor. Testing other sensitivities (e.g., gaseous concentration with respect to total species) is also possible but redundant. The ANISORROPIA-produced sensitivities are compared against CVM results (Fig. 3.4). The black solid line represents $y = x$ and depicts the region of perfect agreement; approximately 10^5 points are represented in each of the six sensitivity comparisons. Despite some deviation at very low relative humidities and lower temperatures, the level of agreement in the results verifies that the adjoint sensitivities are consistent with the model sensitivities for the majority of atmospherically relevant conditions.

3.3.3 Computational efficiency

The computational time required for execution of ANISORROPIA concentration and adjoint sensitivity calculations was assessed by comparing the elapsed CPU time against ISORROPIA v.2.1 with a double-precision activity coefficient module. Both models were executed with the same convergence criteria (e.g., relative difference of activity coefficients from previous iteration $<10^{-10}$). Modeling experiments were designed to examine

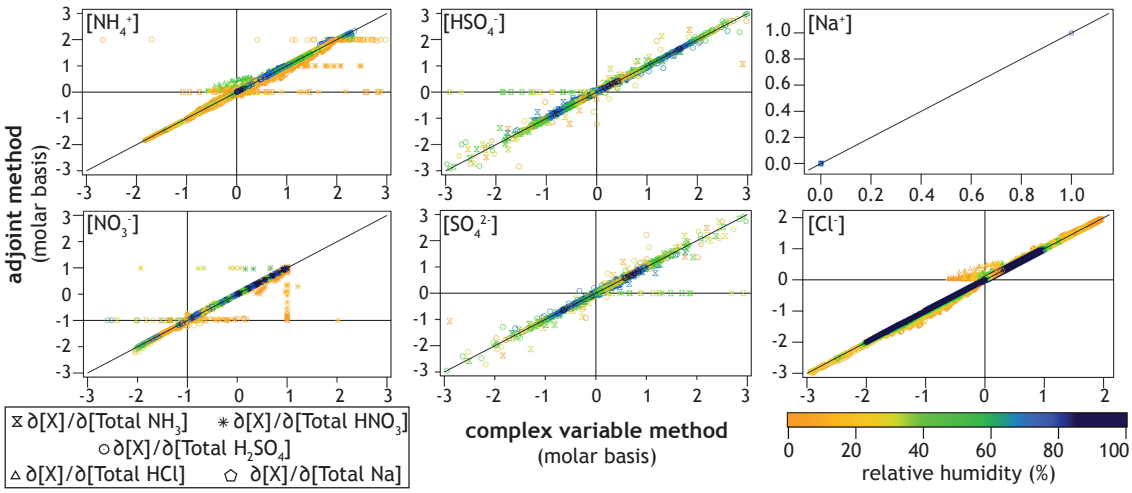

Figure 3.4: The sensitivities of aqueous species with respect to the total amount of each aerosol species on a molar basis from ANISORROPIA are shown against those from CVM for the range of aerosol precursor concentrations, temperature, and RH outlined in the text (Section 3.3).

the three different aerosol systems individually because algorithmic modifications were unique in the three systems. All written output was suppressed so that calculations, not variable writing processes, were evident in the timing comparisons. The assessment was conducted on a 2.93 GHz Intel Core i7 processor running Mac OS X v10.6; source code was compiled with O3 optimization by the Intel Fortran compiler.

The atmospherically relevant evaluation range (Section 3.3) bounded the input for the timing experiments. Only in the NH_4^+-SO_4^{2-}-HSO_4^--H_2O does the adjoint exceed a three-fold increase in computational time over the concentration calculations with the adjoint-based code (Fig. 3.5), which is far less than the theoretical upper limit of a factor of five (*Griewank*, 1989). Even in this case, an algorithmic change to one of the three sub-regimes causes a significant decrease in the concentration calculation cost such that the adjoint sensitivities still require less time than the original model concentration calculations (adjoint/original). The more comprehensive NH_4^+-SO_4^{2-}-HSO_4^--NO_3^--H_2O and NH_4^+-SO_4^{2-}-HSO_4^--NO_3^--Na^+-Cl^--H_2O aerosol systems were less modified, leading to computational costs similar to those of the original model for concentrations (forward/original). The computational efficiency of the post-convergence N-R approach exhibits less than a doubling

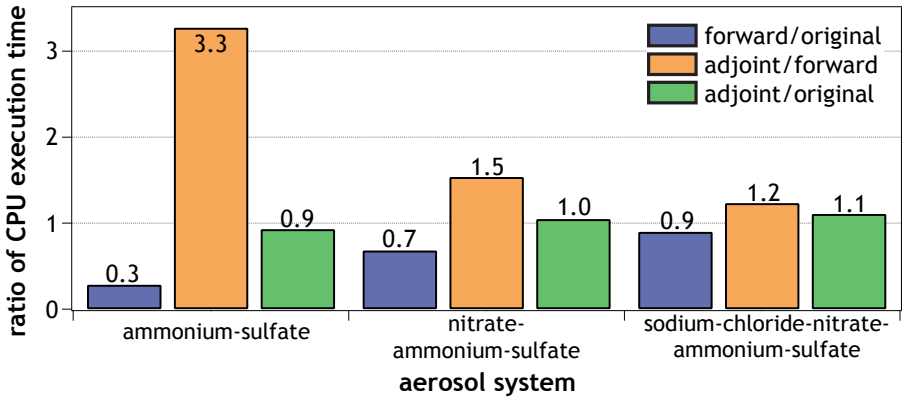

Figure 3.5: The ratios comparing CPU execution time for the calculations of ANISORROPIA forward concentrations (forward), ANISORROPIA adjoint sensitivities (adjoint), and ISORROPIA v.2.1 forward concentrations with double precision activity coefficient calculations (original) are shown. Experiments were designed to elucidate the ratios for each of the aerosol systems treated in ANISORROPIA (SO_4^{2-}-HSO_4^--NH_4^+-H_2O; NO_3^--SO_4^{2-}-HSO_4^--NH_4^+-H_2O; Na^+-Cl^--NO_3^--SO_4^{2-}-HSO_4^--NH_4^+-H_2O). The forward/original comparison reveals the reduced time required because of algorithmic changes required for adjoint development.

of computational time for the adjoint sensitivities over concentrations (adjoint/forward). Convergence criteria optimization through error analysis significantly improved the computational efficiency of ANISORROPIA for both concentration and sensitivity calculations. ANISORROPIA requires similar increases in computational time as the gas-phase adjoint of CMAQ and the adjoint of GEOS-Chem, which are 2 and 1.5 times the original model, respectively (*Hakami et al.*, 2007; *Henze et al.*, 2007). As for memory requirements, the only values necessary from the adjoint forward execution are total species concentrations, RH, and temperature; all values needed for adjoint calculations are recomputed or stored internally in allocatable arrays using the efficient PUSH/POP mechanism of TAPENADE (*Hascoët and Pascual*, 2004).

3.4 Application

ANISORROPIA has been developed for application within the adjoints of CTMs from regional (e.g., Community Multiscale Air Quality model (CMAQ), *Byun and Schere*, 2006) to global scales (e.g., GEOS-Chem, *Henze et al.*, 2007); in these frameworks, its potential

can be fully realized. Nevertheless, applied independently of a CTM, ANISORROPIA provides an efficient, reliable method of determining the sensitivity of dry, inorganic fine mode aerosol to changes in total concentration of sulfate, ammonia, nitrate, sodium, and chloride for deliquesced aerosol. The input required is exactly the same as the forward mode of ISORROPIA (i.e., total concentrations, RH, temperature). ANISORROPIA is used to identify sensitivity regimes over a broad range of atmospherically relevant concentrations (Section 3.4.1). Then, conditions from in situ measurements of the inorganic composition of aerosols and quantities of the gas phase precursors $NH_{3(g)}$, $HNO_{3(g)}$, and $HCl_{(g)}$ from two distinct urban environments (Atlanta, Georgia, USA, and Mexico City, D.F., Mexico) are processed to characterize the urban $PM_{2.5}$ responsiveness to anthropogenically emitted species (Section 3.4.2).

3.4.1 Sensitivity regimes

ANISORROPIA is applied to produce sensitivities for the partitioning of $NH_{3(g)}$ in response to the addition of $H_2SO_{4(g)}$ and then for fine mode, dry aerosol (i.e., $PM_{2.5}$) in response to the same at 300 K (Fig. 3.6). Throughout much of the atmosphere, ammonium contributes a significant fraction of positive ions in aerosol (*Seinfeld and Pandis*, 2006b). The condensation of two moles of $NH_{3(g)}$ for each additional mole of $H_2SO_{4(g)}$ in an air parcel can be expressed as $\frac{\partial[NH^+_{4(aq)}]}{\partial[\text{Total } H_2SO_4]} = 2$ on a molar basis. At 55 % RH, the $\frac{\partial[NH^+_{4(aq)}]}{\partial[\text{Total } H_2SO_4]}$ given by ANISORROPIA demonstrates this behavior when the ratio of total ammonia to sulfate exceeds two (Fig. 3.6b). White space in the ternary diagram denotes occurrence of an error. When the ratio of total ammonia to sulfate is less than two, $\frac{\partial[NH^+_{4(aq)}]}{\partial[\text{Total } H_2SO_4]} = 0$ on a molar basis whether significant water is present (Fig. 3.6a) or not (Fig. 3.6b). In the presence of $HNO_{3(g)}$ and enough water for it to partition significantly to aerosol, $\frac{\partial[NH^+_{4(aq)}]}{\partial[\text{Total } H_2SO_4]}$ ranges between zero and two reflecting the buffering effect of $HNO_{3(g)}$, which evaporates from the aerosol as the $H_2SO_{4(g)}$ condenses (Fig. 3.6a).

ANISORROPIA results elucidate the dry aerosol mass changes due to the addition

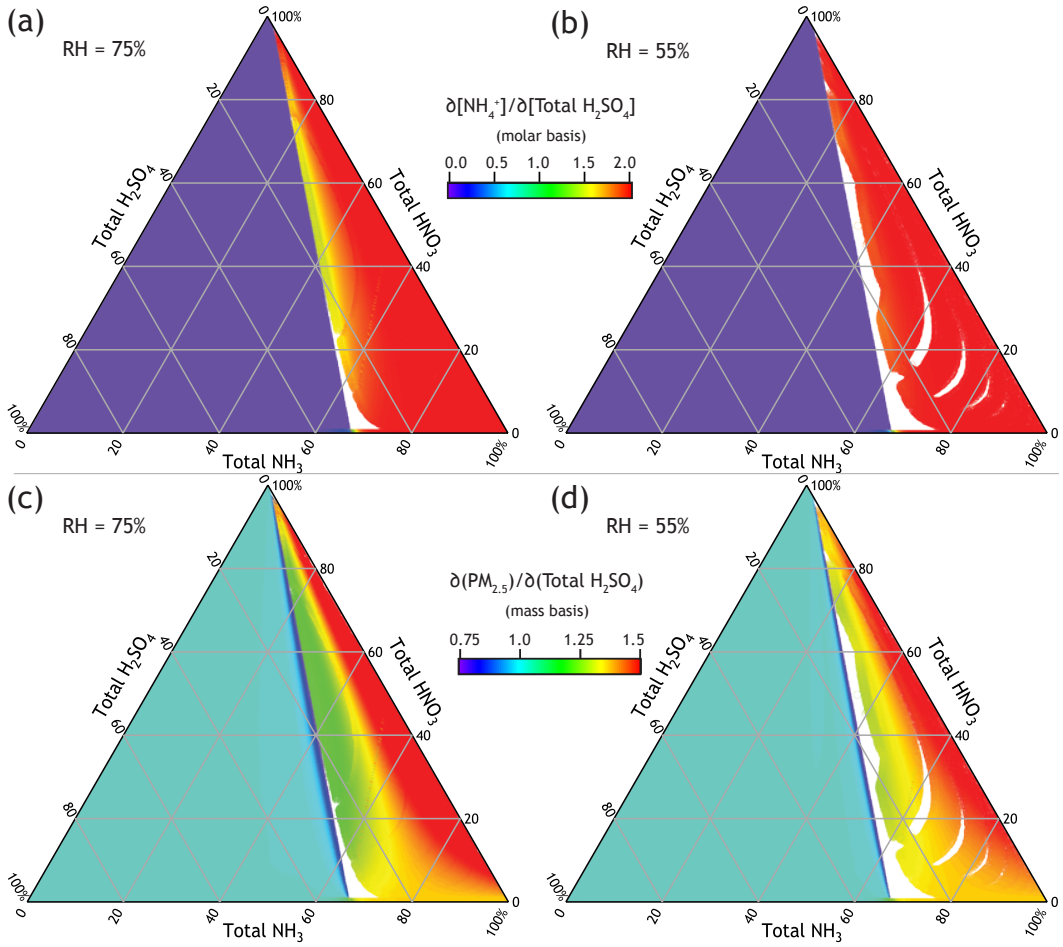

Figure 3.6: ANISORROPIA-produced $\frac{\partial[\mathrm{NH}^+_{4(\mathrm{aq})}]}{\partial[\mathrm{Total\ H_2SO_4}]}$ on a molar basis **(a,b)** and $\frac{\partial(\mathrm{PM}_{2.5,\mathrm{dry}})}{\partial(\mathrm{Total\ H_2SO_4})}$ on a mass basis **(c,d)** for the NH^+_4-SO^{2-}_4-HSO^-_4-NO^-_3-$\mathrm{H_2O}$ aerosol system at RH of 75 % **(a,c)** and 55 % **(b,d)** and a temperature of 300 K. The axes convey the percent a total species (adjacent label) contributes to the molar composition of the system. White space denotes error occurrence.

of 1 μg $\mathrm{H_2SO_{4(g)}}$ at 75 % and 55 % RH and 300 K. $\frac{\partial(\mathrm{PM}_{2.5,\mathrm{dry}})}{\partial(\mathrm{Total\ H_2SO_4})}$, where $(\mathrm{Total\ H_2SO_4})$ is the mass-based concentration of all sulfate in the system, ranges from 0.75 to slightly greater than 1.5 on a mass basis. The molar masses of sulfate (98 g mol^{-1}), ammonium (18 g mol^{-1}), and nitrate (62 g mol^{-1}) are important for understanding these results. Adding one μg of sulfate to a neutralized aerosol should cause an equivalent increase in the dry aerosol mass (Fig. 3.6c, d). Given that acidic aerosol at lower RH has $\frac{\partial[\mathrm{NH}^+_{4(\mathrm{aq})}]}{\partial[\mathrm{Total\ H_2SO_4}]} \simeq 2$ on a molar basis, the condensation of $\mathrm{NH_{3(g)}}$ and $\mathrm{H_2SO_{4(g)}}$ govern the $\frac{\partial(\mathrm{PM}_{2.5,\mathrm{dry}})}{\partial(\mathrm{Total\ H_2SO_4})}$ of 1.37

on a mass basis (Fig. 3.6d). When aerosol nitrate buffers the system by evaporation upon condensation of $H_2SO_{4(g)}$, $\frac{\partial(PM_{2.5,dry})}{\partial(\text{Total } H_2SO_4)}$ drops below 1 on a mass basis, in part due to the higher molar mass of nitrate than ammonium, as shown in a small region of Fig. 3.6c. Low temperatures ($\sim$250 K) and high concentrations of total nitrate relative to total ammonium and sulfate can lead to negative values of $\frac{\partial(PM_{2.5,dry})}{\partial(\text{Total } H_2SO_4)}$, which is caused by the ratio of molar masses of these species and their relative capacity for inducing water uptake (not shown). This variability underscores the importance of sensitivity analysis for air quality.

ANISORROPIA results for the NH_4^+-SO_4^{2-}-HSO_4^--NO_3^--Na^+-Cl^--H_2O aerosol system reveal even more complex sensitivity relationships quite clearly (Fig. 3.7). $\frac{\partial[NH_{4(aq)}^+]}{\partial[\text{Total } H_2SO_4]}$ is shown for a system with 30 μg m^{-3} total HCl and 0.63 μg m^{-3} total HNO_3 at 40 % RH and 300 K. The abscissa corresponds to the sum of the total amounts of the species producing positive ions, Na and NH_3. The ordinate corresponds to the total H_2SO_4 in the system. Differing amounts of sodium in the system define the three regions, which overlap slightly to show the effect of sodium on the sensitivity. Region I (forward-slanted hash marks), where sodium is absent, demonstrates the primary role of $NH_{4(aq)}^+$ in neutralizing sulfate. The sensitivity of 2 on a molar basis for $\frac{\partial[NH_{4(aq)}^+]}{\partial[\text{Total } H_2SO_4]}$ persists when $R_S \geq 2$; however, if R_S<2, $\frac{\partial[NH_{4(aq)}^+]}{\partial[\text{Total } H_2SO_4]} = 0$. This behavior is consistent with that demonstrated in the NH_4^+-SO_4^{2-}-HSO_4^--NO_3^--H_2O system (Fig. 3.6). Region II (vertical hash marks) reveals the system sensitivity when $Na_{(aq)}^+$ contributes to neutralizing sulfate. At the far left edge of Region II, $Na_{(aq)}^+$ constitutes the majority of the positive ions; therefore, the $\frac{\partial[NH_{4(aq)}^+]}{\partial[\text{Total } H_2SO_4]}$ is negligible. Moving to the right across Region II, the concentration of positively charged $Na_{(aq)}^+$ ions is exceeded by $SO_{4(aq)}^{2-}$ ions, and $\frac{\partial[NH_{4(aq)}^+]}{\partial[\text{Total } H_2SO_4]}$ increases correspondingly. Finally, in Region III, the same reduced value of $\frac{\partial[NH_{4(aq)}^+]}{\partial[\text{Total } H_2SO_4]}$ appears with a dampened rate of increase of $NH_{4(aq)}^+$ contribution to positively charged ions due to the large contribution from $Na_{(aq)}^+$ and minor buffering by $NO_{3(aq)}^-$ and $Cl_{(aq)}^-$. ANISORROPIA could also be applied at different RH, temperature, or compositions to reveal similarly meaningful sensitivity regimes.

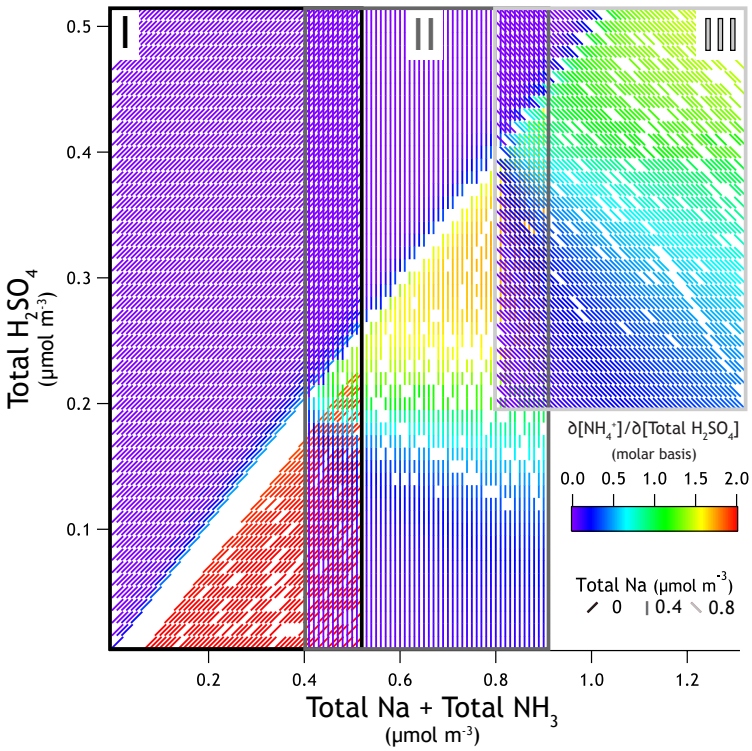

Figure 3.7: ANISORROPIA-produced $\frac{\partial[\mathrm{NH}^+_{4(\mathrm{aq})}]}{\partial[\mathrm{Total\ H_2SO_4}]}$ (molar basis) for the NH^+_4-SO^{2-}_4-HSO^-_4-NO^-_3-Na^+-Cl^--$\mathrm{H_2O}$ aerosol system at a RH of 40 % and a temperature of 300 K. The total HCl is 0.8 μmol m^{-3}, and the total $\mathrm{HNO_3}$ is 0.01 μmol m^{-3}. Region I corresponds to 0 μmol m^{-3} of total Na, region II to 0.4 μmol m^{-3} of total Na, and region III to 0.8 μmol m^{-3} of total Na. Note the transition in sensitivity at a ratio of 2 moles of positive ions (total $\mathrm{NH_3}$ + Na) to 1 mole of total $\mathrm{H_2SO_4}$ ($R_S = 2$). The increasing gradient from left to right in Regions II and III demonstrates the contribution of positive ions from $\mathrm{Na}^+_{(\mathrm{aq})}$ initially balancing $\mathrm{SO}^{2-}_{4(\mathrm{aq})}$ (i.e., low $\frac{\partial[\mathrm{NH}^+_{4(\mathrm{aq})}]}{\partial[\mathrm{Total\ H_2SO_4}]}$) and the increasing contribution of $\mathrm{NH}^+_{4(\mathrm{aq})}$ to the charge balance with more negative ions present.

3.4.2 Observed conditions

3.4.2.1 Atlanta, Georgia, USA

The Atlanta Aerosol Nucleation and Real-Time Characterization Experiment (Atlanta-ANARChE) in July and August of 2002 included measurements of $\mathrm{NH}_{3(\mathrm{g})}$ and $\mathrm{HNO}_{3(\mathrm{g})}$ via two distinct methods of chemical ionization mass spectrometry (*Neuman et al.*, 2003; *Nowak et al.*, 2006). The ground campaign was conducted at Jefferson Street in midtown Atlanta, one of the sites of the ongoing Southeast Aerosol Research and Characterization

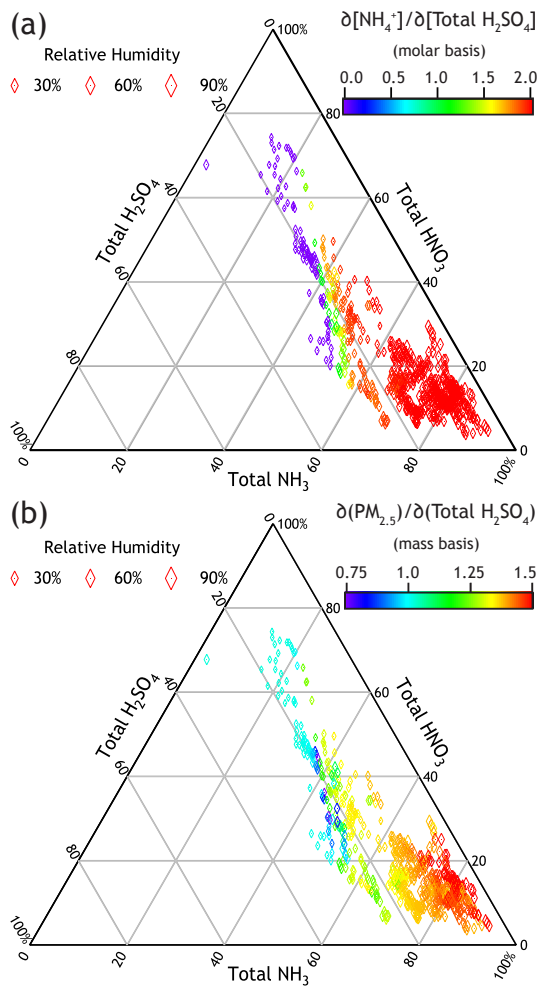

Figure 3.8: ANARChE data processed with ANISORROPIA reveal Atlanta $\frac{\partial[\mathrm{NH}^+_{4(\mathrm{aq})}]}{\partial[\mathrm{Total\ H_2SO_4}]}$ (molar basis) **(a)** and $\frac{\partial(\mathrm{PM}_{2.5,\mathrm{dry}})}{\partial(\mathrm{Total\ H_2SO_4})}$ (mass basis) **(b)** in July–August 2002. RH ranges from 25 %–99 % and temperature from 293 K to 310 K.

(SEARCH) study (*Hansen et al.*, 2003) and the location of the Atlanta Supersite (*Solomon et al.*, 2003). SEARCH instrumentation measured sulfate ($\mathrm{SO}^{2-}_{4(\mathrm{aq})}$), ammonium ($\mathrm{NH}^{+}_{4(\mathrm{aq})}$), and nitrate ($\mathrm{NO}^{-}_{3(\mathrm{aq})}$) concentrations with continuous 1-min resolution coincident with the gas phase measurements (*Edgerton et al.*, 2006). Meteorological data collected include RH and temperature. *Nowak et al.* (2006) demonstrated the level of accuracy of ISORROPIA in predicting the partitioned concentrations, which also governs the accuracy of the aerosol sensitivities of ANISORROPIA.

ANARChE data were collected in the range of 25–99 % RH and 293–310 K. Results

find that $\frac{\partial[\mathrm{NH}^+_{4(\mathrm{aq})}]}{\partial[\mathrm{Total\ H_2SO_4}]} = 2\,\mathrm{mol\,mol}^{-1}$ while the molar composition is 5–20 % total H_2SO_4 and 60–95 % Total HNO_3 (Fig. 3.8a). $\frac{\partial[\mathrm{NH}^+_{4(\mathrm{aq})}]}{\partial[\mathrm{total\ H_2SO_4}]}$ is negligible when total H_2SO_4 makes up 10–20 % and total HNO_3 makes up 20–40 % of the molar composition, which is consistent with sensitivities shown in Fig. 3.6a,b. The calculated $\frac{\partial(\mathrm{PM_{2.5,dry}})}{\partial(\mathrm{Total\ H_2SO_4})}$ typically exceeds 1.3 μg (μg)$^{-1}$ for this time period. Condensation of $NH_{3(g)}$ to neutralize $H_2SO_{4(g)}$ occurs; additionally, sufficient $NH_{3(g)}$ is present with high concentrations of $HNO_{3(g)}$ to allow $\frac{\partial(\mathrm{PM_{2.5,dry}})}{\partial(\mathrm{Total\ H_2SO_4})}$ to exceed 1.37 μg (μg)$^{-1}$ by the formation of deliquesced ammonium nitrate aerosol. When the sulfate is neutralized, $\frac{\partial(\mathrm{PM_{2.5,dry}})}{\partial(\mathrm{Total\ H_2SO_4})}$ decreases to one as the addition of sulfate leads only to its condensation, not that of $NH_{3(g)}$.

3.4.2.2 Mexico City, D.F., Mexico

Comprehensive measurements from the Megacity Initiative: Local and Global Research Observations (MILAGRO) campaign during March of 2006 (*Molina et al.*, 2010) facilitate the characterization of aerosol sensitivities for a very different urban air mass than that found in Atlanta due to the presence of sodium and chloride as well as significantly higher $NH_{3(g)}$ concentrations. The campaign included three ground sites with one in the urban center at the Instituto Mexicano del Petróleo (T0 site), another at the Universidad Tenológica de Tecámac in the state of Mexico (T1 site), and a third site at Rancho La Bisnaga in the state of Hidalgo (T2 site). For this investigation, data are analyzed for the period of 21–30 March 2006, from the T1 site, which is typically downwind of Mexico City. Measurements provide the $PM_{2.5}$ concentrations of $SO_{4(p)^{2-}}$, $NH_{4(p)^+}$, $NO_{3(p)^-}$, $Na_{(p)^+}$, $Cl_{(p)^-}$, $Ca_{(p)^{2+}}$, $K_{(p)^+}$, and $Mg_{(p)^{2+}}$; gaseous concentrations of $NH_{3(g)}$, $HNO_{3(g)}$, and $HCl_{(g)}$; and the ambient RH and temperature (*Fountoukis et al.*, 2009). The $PM_{2.5}$ ionic concentrations were measured by a Particle Into Liquid Sampler (PILS) with a 6-min integrated sampling period and a new chromatogram begun every 17 min (*Orsini et al.*, 2003). Gaseous concentrations of $NH_{3(g)}$ were obtained with a quantum cascade laser (QCL) spectrometer and $HNO_{3(g)}$

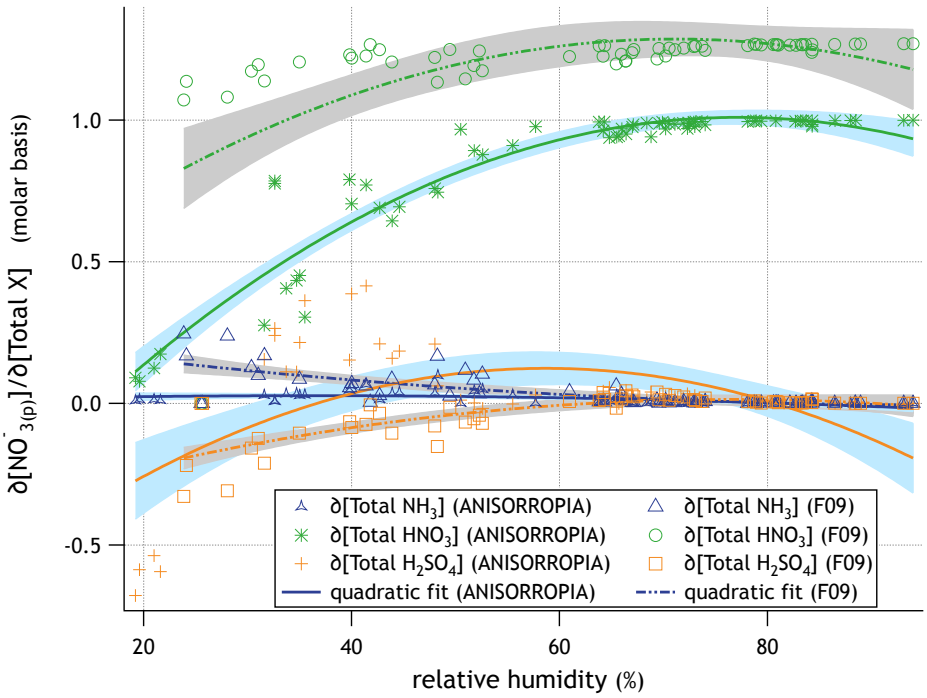

Figure 3.9: The ANISORROPIA-produced $\frac{\partial[\mathrm{NO}^-_{3(\mathrm{aq})}]}{\partial[\mathrm{Total\ HNO_3}]}$, $\frac{\partial \mathrm{NO}^-_{3(\mathrm{aq})}}{\partial[\mathrm{Total\ NH_3}]}$, and $\frac{\partial \mathrm{NO}^-_{3(\mathrm{aq})}}{\partial[\mathrm{Total\ H_2SO_4}]}$ values are plotted alongside backward finite difference sensitivities from *Fountoukis et al.* (2009) (F09) for MILAGRO observations in Mexico City. The quadratic fits to the senstivity data are shown to direct the eye with the 95 % confidence interval given by the shaded bands about the fit lines. Solid lines and light blue shading correspond to ANISORROPIA sensitivities; dashed lines and gray shading correspond to F09 sensitivities. With the exception of the fit about $\frac{\partial \mathrm{NO}^-_{3(\mathrm{aq})}}{\partial[\mathrm{Total\ H_2SO_4}]}$, ANISORROPIA has tighter bands than F09, indicating less scatter in the results due to the direct computation of sensitivity about the desired input. ANISORROPIA characterizes the sensitivity of Mexico City aerosol nitrate similarly to the full forward model employed by F09.

concentrations were deduced from the volatile nitrate (i.e., $\mathrm{HNO_{3(g)}}$+$\mathrm{NH_4NO_{3(p)}}$) concentrations acquired with the thermal dissociation-laser induced fluorescence of nitrogen oxides (TD-LIF) (*Day et al.*, 2002; *Farmer et al.*, 2006). More details regarding data acquisition, uncertainty analysis, and quality assurance are given by *Fountoukis et al.* (2009).

As shown by *Fountoukis et al.* (2009) and since $R_S > 2$, $\frac{\partial[\mathrm{NH}^+_{4(\mathrm{aq})}]}{\partial[\mathrm{Total\ H_2SO_4}]} = 2\,\mathrm{mol\,mol^{-1}}$ except at RH less than the mutual deliquescence RH of $\mathrm{NaNO_{3(s)}}$ and $\mathrm{NH_4NO_{3(s)}}$ (i.e., approximately 50 % RH). To investigate a more variable component of the $\mathrm{NH_4^+}$-$\mathrm{SO_4^{2-}}$-$\mathrm{HSO_4^-}$-$\mathrm{NO_3^-}$-$\mathrm{Na^+}$-$\mathrm{Cl^-}$-$\mathrm{H_2O}$ aerosol system, the sensitivity of aerosol $\mathrm{NO^-_{3(aq)}}$ is explored

as in *Fountoukis et al.* (2009) (Fig. 3.9). The *Fountoukis et al.* (2009) sensitivities are calculated by backward finite difference with explicit treatment of crustal species and the possibility for aerosol species to condense into solid salts. ANISORROPIA evaluates the same input by treating the crustal species $Mg_{(p)^{2+}}$ and $K_{(p)^{+}}$ as equivalent moles of sodium based on ionic charge (*Moya et al.*, 2001) and $Ca_{(p)^{2+}}$ as insoluble $CaSO_{4(s)}$. Additionally, aerosol are assumed to be deliquesced, as is common in CTMs and leads to minor differences (*Fountoukis et al.*, 2009). In an environment with excess $NH_{3(g)}$, $\frac{\partial[NO^{-}_{3(aq)}]}{\partial[\text{Total } HNO_3]}$ is expected to be 1 mol mol^{-1} unless insufficient aerosol water is present to absorb the additional $HNO_{3(g)}$. ANISORROPIA produces this expected sensitivity (Fig. 3.9, green asterisks) and with less scatter than the backward finite difference sensitivities given by *Fountoukis et al.* (2009). The greater scatter about the polynomial fit line for the F09 sensitivities is expected due to the limited accuracy of the finite difference method (Section 3.3.2). Furthermore, backward finite difference sensitivities exceed the expected value of 1 mol mol^{-1} for RH greater than 50 %, which ANISORROPIA more accurately represents. Complementary to this sensitivity are the values of $\frac{\partial[NO^{-}_{3(aq)}]}{\partial[\text{Total } NH_3]}$ and $\frac{\partial[NO^{-}_{3(aq)}]}{\partial[\text{Total } H_2SO_4]}$, which are expected to be zero. Again, reduced scatter above 50 % RH is evident for ANISORROPIA results. The backward finite difference results for $\frac{\partial[NO^{-}_{3(aq)}]}{\partial[\text{Total } NH_3]}$ are significantly different than the central finite difference results with the same perturbation size, which align much more closely with ANISORROPIA $\frac{\partial[NO^{-}_{3(aq)}]}{\partial[\text{Total } NH_3]}$ values for 30–50 % RH (not shown). ANISORROPIA reveals that aerosol nitrate in Mexico City is primarily sensitive to the addition of $HNO_{3(g)}$, a conclusion congruent with the findings of *Fountoukis et al.* (2009).

3.5 Conclusions

The increasing measurements of aerosol composition from field campaigns and observations of aerosol precursor concentrations from satellites provide a substantial opportunity to advance the predictive capabilities of CTMs. One efficient method of gleaning valuable information from these data is to solve the inverse problem by applying the adjoint

method to optimize emissions parameters, initial conditions, or boundary conditions of the CTM. Specifically, with a CTM adjoint, the computational cost of optimization no longer scales with the number of parameters being optimized, which is essential for spatially and temporally variable aerosol precursor emissions. Furthermore, receptor-oriented sensitivity analysis, possible only with a CTM adjoint, elucidates the relative impacts of emissions sources on air quality, human health, and climate metrics with temporal and spatial resolution.

This work presents the development and independent applications of ANISORROPIA, the adjoint of the thermodynamic aerosol model ISORROPIA for the Na^+-SO_4^{2-}-HSO_4^--NH_4^+-NO_3^--Cl^--H_2O aerosol system. Development involved modification of the forward model code and application of the automatic differentiation tool, TAPENADE (*Hascoët and Pascual*, 2004). Verification of ANISORROPIA required development of a complex variable version of ISORROPIA and evaluation against sensitivities produced by it, which are more reliable than the finite difference method. Further development of ANISORROPIA will extend its capacity to treat the crustal species included in ISORROPIA II (Mg^{2+}, Ca^{2+}, and K^+) as well as the reverse mode execution for the purpose of calculating dynamic equilibrium. ANISORROPIA is used to reveal the sensitivity regimes of aerosol ammonium to sulfate and fine mode, dry aerosol mass to sulfate for a wide range of atmospherically relevant conditions. ANISORROPIA is employed to characterize the sensitivity regimes of the distinct urban air masses of Atlanta and Mexico City. Receptor-oriented sensitivity analysis with CTM adjoints including ANISORROPIA shall be useful for investigating the relative contribution of specific emissions sources to radiative forcing and air quality. Within the adjoints of regional and global CTMs, ANISORROPIA can provide the ability to trace the impact of the major components of inorganic aerosol and their precursors back to the emissions source. Finally, ANISORROPIA enables assimilation of observations of inorganic aerosol precursor and aerosol concentrations in an inverse modeling framework.

CHAPTER IV

TRACING CLOUD DROPLET CONCENTRATIONS TO AEROSOL PRECURSOR EMISSIONS WITH ADJOINTS

In this chapter, the adjoints of the GEOS-Chem Chemical Transport Model and a comprehensive cloud droplet parameterization are coupled to study the sensitivity of cloud droplet number concentration (N_d) over US regions and Central Europe to global emissions of anthropogenic fine aerosol precursors. Simulations reveal that the N_d over the midwestern and southeastern US is mostly sensitive to SO_2 emissions during August, and to NH_3 emissions during February. Over the western US, N_d is mostly sensitivity to SO_2 and primary organic aerosol emissions. In Central Europe, N_d is most sensitive to NH_3 and NO_x emissions. As expected, local emissions strongly affect N_d; long-range transport, however, is also important for the western US and Europe. Emissions changes projected for the year 2050 are estimated to have the largest impacts on cloud albedo and N_d over Central Europe during August (42% and 82% change, respectively) and western US during February (12% and 36.5% change, respectively).

This chapter accepted for publication as: Karydis, V. A., S. L. Capps, R. H. Moore, A. G. Russell, D. K. Henze, and A. Nenes (in press), Using a global aerosol model adjoint to unravel the footprint of spatially-distributed emissions on cloud droplet number and cloud albedo, Geopysical Research Letters.

4.1 Introduction

Cloud droplets form upon pre-existing atmospheric aerosols, and their modulation from anthropogenic emissions has profound impacts on cloud radiative properties, the hydrological cycle and climate. The impact of aerosol on regional climate can be even stronger, owing to the variability of aerosol and regional climate sensitivity (*Shindell et al.*, 2009). Attribution of climate forcing from sector-specific emissions is based on sequential perturbation calculations at the cost of a climate run per sector investigated (*Shindell et al.*, 2009). This approach is frequently limited by addressing only one sector (e.g., transport (*Fuglestvedt et al.*, 2008)) or by invoking approximations required to reduce the computational burden (e.g., constant oxidant levels (*Koch et al.*, 2007)). Adjoint modeling provides an efficient sensitivity analysis alternative to brute-force approaches and does not require perturbations in emissions. This is accomplished by propagating a differential variation of a model output (e.g., aerosol concentration) backwards through the model to express its sensitivity with respect to inputs of interest (e.g., emissions) without perturbing the model state.

The GEOS-Chem chemical transport model (CTM) is a widely used global model for studying chemistry-aerosol-climate interactions (*Leibensperger et al.*, 2012a,b). *Henze et al.* (2007) developed the adjoint of the code and since has been used, for example, to study black carbon over the Tibetan Plateau (*Kopacz et al.*, 2011). Here the GEOS-Chem adjoint is coupled together with the adjoint of a comprehensive droplet parameterization (*Karydis et al.*, 2012) to quantify the influences of global emissions of primary organic aerosol (POA) and inorganic aerosol precursors (SO_2, NO_x, and NH_3) on the predicted cloud droplet number concentration (N_d) and cloud albedo (A) within three regions of the continental US and Central Europe during August and February for 2008 and 2050.

4.2 Methods

4.2.1 Model framework description

The GEOS-Chem model (v.9.1.1, `http://geos-chem.org`) is used to simulate the global aerosol distributions during February and August 2008, with 4x5 degree horizontal resolution and 47 pressure levels from the surface to 0.01 hPa. The GEOS-Chem model is driven using assimilated meteorological data from the Goddard Earth Observing System (GEOS-5) of the NASA Global Modeling and Assimilation Office (GMAO) and includes gas-phase chemistry coupled with heterogeneous reactions, inorganic aerosol thermodynamics, and oxidative aging of carbonaceous aerosols (*Bey et al.*, 2001). NH_3 emissions are from the Global Emission Inventory Activity (GEIA) inventory (*Bouwman et al.*, 1997). Biogenic VOCs follow the Model of Emissions of Gases and Aerosols from Nature (MEGAN) inventory (*Guenther et al.*, 2006). NO_x and SO_x emissions are obtained from the Emissions Database for Global Atmospheric Research (EDGAR) inventory (*Olivier and Berdowski*, 2001). These global inventories are overwritten with regional inventories for the US (NEI99), Europe (EMEP), southeast Asia (*Streets et al.*, 2003), and Mexico (BRAVO) (*Kuhns et al.*, 2005). Biomass burning emissions are from *van der Werf et al.* (2006),

The adjoint of the GEOS-Chem model (*Henze et al.*, 2007) computes $\frac{\partial M_{a,tot}}{\partial E_{i,j}}$, the sensitivity of total aerosol mass concentrations, $M_{a,tot}$, to specific emissions, E_i, (where i is the emissions type) for each grid cell j. In this study, $\frac{\partial M_{a,tot}}{\partial E_{i,j}}$ is calculated monthly for $M_{a,tot}$ on the final day of the month.

Aerosol mass concentrations from GEOS-Chem follow a prescribed number size distribution (Table 4.1) according to *Karydis et al.* (2012) and distributed in three externally mixed modes: i) sulfate, ammonium, nitrate, organics, and black carbon from anthropogenic and biomass burning sources (*Chuang and Walton*, 1997; *Radke et al.*), ii) sulfate, nitrate, and sea salt from marine processes (*Lance et al.*, 2004), and, iii) mineral dust (*d'Almeida*, 1987). Sensitivity to secondary organic aerosol (SOA) is not considered, as

Table 4.1: Size distribution parameters applied to aerosol populations from GEOS-Chem model.

Aerosol type	Aerosol components	Density (g cm^{-3})	Median diameter (μm)	Geometric standard deviation	Number fraction	Reference
Anthropogenic, Biomass Burning	Sulfate	1.77	0.1	1.9	1	Chuang et al. [1997]; Radke et al. [1988]
	Nitrate	1.725				
	Ammonium	1.75				
	Organic Carbon	1.2				
	Black Carbon	1.5				
Marine	Sulfate	1.77	0.018	1.4	0.81	Lance et al. [2004]
	Nitrate	1.725	0.075	1.6	0.18	
	Sea Salt	2.2	0.62	2.7	0.01	
Mineral Dust	Mineral Dust	2.6	0.16	2.1	0.93	D'Almeida et al. [1987]
			1.4	1.9	0.07	
			10	1.6	3×10^{-6}	

GEOS-Chem does not produce adjoint sensitivities of SOA mass to volatile organic carbon emissions. Following *Karydis et al.* (2011), the number concentration of each aerosol mode is given by $N_a = \frac{m_{tot}}{V\rho_{tot}}$ where m_{tot} is the total mass concentration of the aerosol mode, V is the volume of the dry aerosol, and ρ_{tot} is the density of the aerosol given by $\rho_{tot} = \frac{m_{tot}}{\sum_{y=1}^{Y} fracm_y\rho_y}$. m_y is the mass concentration of each component within the aerosol mode (e.g. sulfate, nitrate, ammonium, OC, BC), ρ_y is its density, and Y is the number of aerosol components. The hygroscopicity of each aerosol mode is calculated based on the aerosol composition, provided by GEOS-Chem, and is given by $\kappa = \frac{VH_{f,tot}\rho_{tot}V_{f,s}M_w}{M_s\rho_w}$, where $V_{f,s}$ is the soluble volume fraction, M_w and M_s is the molecular weight of water and soluble fraction respectively, ρ_w is the density of water, and $VH_{f,tot}$ is the total Van't Hoff factor of soluble fraction given by $VH_{f,tot} = \frac{\sum_{y=1}^{YS} \frac{m_y VH_{f,y}}{M_y}}{\sum_{y=1}^{YS} \frac{m_y}{M_y}}$, where YS is the number of aerosol soluble components, $VH_{f,y}$ is the Van't Hoff factor of each soluble aerosol component, and M_y is the molecular weight of each soluble aerosol component. Other important parameters for N_d calculations are presented by *Karydis et al.* (2012).

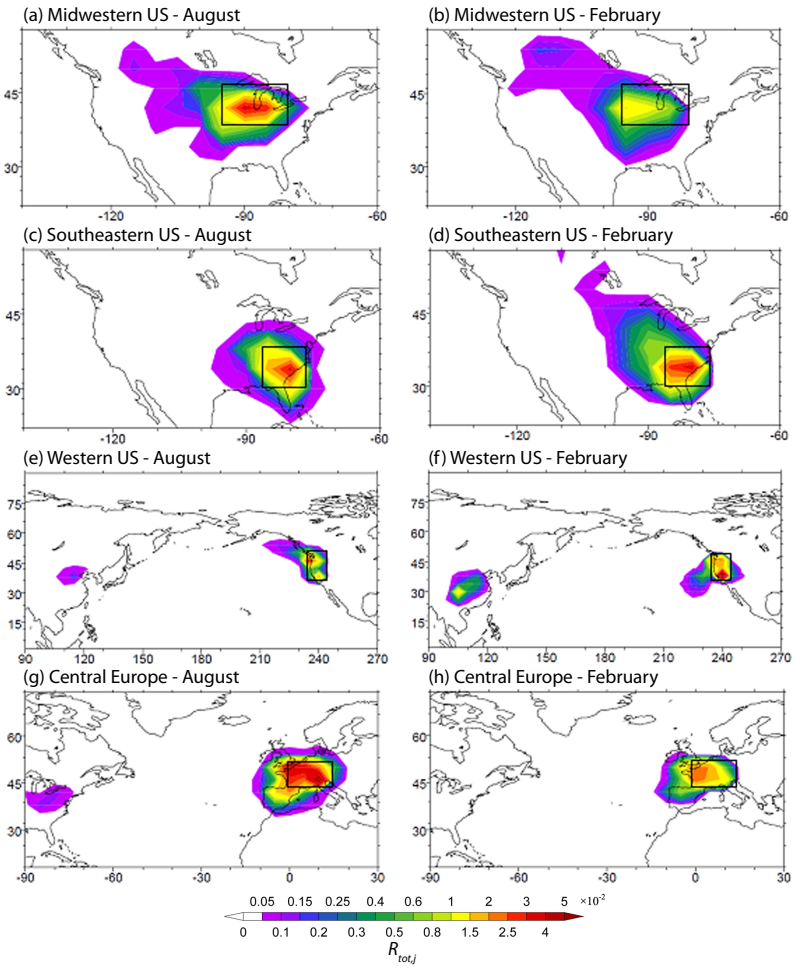

Figure 4.1: Contribution of total anthropogenic emissions to cloud droplet number concentration over Midwest US (a, b), Southeast US (c, d), Western US (e, f), and Central Europe (g, h) during August (left column) and February (right column) of 2008. The regions of study are denoted by the squares.

Calculation of N_d is carried out with the *Kumar et al.* (2009) parameterization; droplets are formed in ascending cloud parcels that contain soluble and insoluble particles competing for water vapor. The N_d adjoint (*Karydis et al.*, 2012) provides the sensitivity of N_d with respect to the parameterization input (updraft velocity, uptake coefficient and the number, hygroscopicity/adsorption parameters of each aerosol lognormal mode). The two adjoint frameworks elucidate the relationship of emissions to N_d by combining the local sensitivity of N_d to aerosol number concentration, $\frac{\partial N_d}{\partial N_a}\Big|_r$ (converted into local sensitivity of N_d to aerosol mass concentration, $\frac{\partial N_d}{\partial M_a}\Big|_r$, following the aerosol mass to number conversion

as presented by *Karydis et al.* (2012), with the sensitivity of total aerosol mass concentrations to anthropogenic emissions from each grid cell of the model, $\frac{\partial M_{a,tot}}{\partial E_{i,j}}$, obtained from the GEOS-Chem adjoint. The result is the footprint (or impacts expressed as the sensitivity) of anthropogenic emissions from each grid cell on the droplet number over the same region, $\frac{\partial N_{d,tot}}{\partial E_{i,j}} = \left(\sum_{r=1}^{R} \frac{\partial N_d}{\partial M_a}\Big|_r\right)\left(\frac{\partial M_{a,tot}}{\partial E_{i,j}}\right)$, where R is the total number of cells in the region. The relative importance of anthropogenic emissions from each grid cell are presented as fully normalized sensitivities, $R_{i,j} = \frac{E_{i,j}}{N_d}\frac{\partial N_d}{\partial E_{i,j}} = \frac{\partial \ln N_d}{\partial \ln E_{i,j}}$, where $E_{i,j}$ is the emission of type i considered for grid cell j and N_d is the droplet concentration over the region of study. $R_{tot,i,j}$ expresses the contribution of total anthropogenic emissions from grid cell j on N_d and $R_{i,tot}$ expresses the total (worldwide) contribution of anthropogenic emissions of type i (NH_3, SO_2, NO_x, or POA) on N_d. A detailed description of the sensitivity calculations follows in Section 4.2.2. The sensitivity results can be used to estimate the change in future N_d and cloud albedo, especially since adjoint sensitivities tend to be more robust than traditional source-receptor relationships determined from perturbing emissions across broad spatial scales (*Turner et al.*, 2012). We consider projected aerosol precursor emissions following the Representative Concentration Pathway 4.5 (RCP4.5, Table 4.1), where total radiative forcing is stabilized before 2100 by employment of a range of technologies and strategies for reducing greenhouse gas emissions (*Clarke et al.*, 2007). Using the projected emissions change between 2010 and 2050, the change in N_d, ΔN_d, for each region is calculated for February and August. The first order change in cloud albedo (ΔA) is calculated from ΔN_d by integrating the susceptibility of A to N_d, $\frac{\partial A}{\partial N_d} = \frac{A(1-A)}{3N_d}$ (*Twomey*, 1991) over each region between 2010 and 2050 values. Cloud albedo at 2050, A_2050, is then given by differencing NASA CERES satellite total sky and clear sky albedos for February and August (*Acker and Leptoukh*, 2007) as described in (*Moore et al.*, 2012). These calculations give an upper limit on albedo change since liquid water feedbacks which mitigate microphysical changes are not considered (*Stevens and Feingold*, 2009). Given the lack of explicit microphysics in this study, a required assumption is that the aerosol number

size distribution shape remains unchanged in the future. This may induce some error in the predicted sensitivity; as differences in aerosol microphysical processes may change the relationship between emissions and CCN concentrations. Toward this, *Manktelow et al.* (2009) found that the aerosol number potential of N. American and Asian emissions was a factor of 3 to 4 times larger than that of European emissions, resulting in a 70% more efficient production of CCN.

4.2.2 Computing sensitivities

Figure 4.1 presents the fully normalized sensitivity (unitless) of regional N_d to anthropogenic emissions from each grid cell as in Equation 4.1.

$$\begin{aligned} R_{i,j} &= \sum_{r=1}^{R}((\frac{N_{a,r}}{N_{d,r}}\frac{\partial N_{d,r}}{\partial N_{a,r}})\sum_{y=1}^{Y}(\frac{M_{a,r,y}}{N_{a,r}}\frac{\partial N_{a,r}}{\partial M_{a,r,y}}))(\frac{E_{i,j}}{\sum_{r,y=[1,1]}^{[R,Y]}M_{a,r,y}}\frac{\partial\sum_{r,y=[1,1]}^{[R,Y]}M_{a,r,y}}{\partial E_{i,j}}) \\ &= \frac{E_{i,j}}{\sum_{r=1}^{R}N_{d,r}}\frac{\partial\sum_{r=1}^{R}N_{d,r}}{\partial E_{i,j}} \\ &= \frac{\partial \ln N_d}{\partial \ln E_{i,j}} \end{aligned} \tag{4.1}$$

, where $E_{i,j}$ is the emission type of i considered for grid cell j, $N_{a,r}$ and $N_{d,r}$ are the aerosol number and droplet number concentrations for regional grid cell r, respectively; $M_{a,r,y}$ is the aerosol mass concentration of species y for regional grid cell r; and N_d is the total droplet number concentration over the region of study. The first term,

$$\sum_{r=1}^{R}\left((\frac{N_{a,r}}{N_{d,r}}\frac{\partial N_{d,r}}{\partial N_{a,r}})\sum_{y=1}^{Y}(\frac{M_{a,r,y}}{N_{a,r}}\frac{\partial N_{a,r}}{\partial M_{a,r,y}})\right) \tag{4.2}$$

is the fully normalized adjoint sensitivity of total droplet number to aerosol mass concentration, over the region of study, from the droplet activation parameterization; the second term, $\left(\frac{E_{i,j}}{\sum_{r,y=[1,1]}^{[R,Y]}M_{a,r,y}}\frac{\partial\sum_{r,y=[1,1]}^{[R,Y]}M_{a,r,y}}{\partial E_{i,j}}\right)$, is the fully normalized adjoint sensitivity of aerosol mass concentration, over the region of study, to anthropogenic emissions of type i considered for grid cell j, calculated by GEOS-Chem adjoint. The above sensitivity calculations

Table 4.2: Fractional emission change (2010-2050) for SO_2, NH_3, NO_x, and primary OC based on RCP4.5 scenario. Negative values correspond to a decrease from 2010 to 2050.

Region	SO_2	NH_3	NO_x	Primary OC
Western Europe, Northern America, Australia, Japan	-0.72	0.06	-0.62	0.02
Eastern Europe, Russia	-0.69	0.03	-0.50	-0.10
Asia	-0.64	0.12	-0.24	-0.52
Middle East, Africa	-0.05	0.20	0.04	0.00
Latin and Central America	-0.49	0.06	-0.23	-0.42

are made only for the aerosol mode containing sulfate, ammonium, nitrate, organics, and black carbon, since currently GEOS-Chem does not produce adjoint sensitivities to sea salt and dust emissions.

Figure 4.2a depicts the total worldwide contribution of anthropogenic emissions to present N_d (unitless): $R_{i,j} = \frac{\partial \ln N_d}{\partial \ln E_{i,j}}$, where i is the emission type and n is the total number of grid cells. Figure 4.2b depicts the total worldwide contribution of anthropogenic emissions to future N_d (unitless), $R_{i,j} = \frac{\partial \ln N_d}{\partial \ln E_{i,j}} \frac{(1+\Delta E_{i,j})}{(1+\Delta N_d)}$, where $\Delta E_{i,j}$ and ΔN_d are the fractional change of emissions $\left(\frac{E_{i,j,2050}-E_{i,j,2010}}{E_{i,j,2010}}\right)$ and droplet number $\left(\frac{N_{d,2050}-N_{d,2010}}{N_{d,2010}}\right)$ from Table 4.2 and Table 4.3, respectively.

Table 4.3 presents the change in N_d (cm^{-3}) due to future emissions changes as Equation 4.3.

$$\left(\frac{\partial N_d}{\partial M_a}\right)\left(E_{i,j}\frac{\partial M_a}{\partial E_{i,j}}\right)\Delta E_{i,j} = \frac{\partial N_d}{\partial E_{i,j}}(E_{i,j,2050} - E_{i,j,2010}) \tag{4.3}$$

The first term, $\left(\frac{\partial N_d}{\partial M_a}\right)$, is the un-normalized adjoint sensitivity of droplet number to aerosol mass concentration, over the region of study, from the droplet activation parameterization, while the second term, $\left(E_{i,j}\frac{\partial M_a}{\partial E_{i,j}}\right)$, is the semi-normalized adjoint sensitivity of aerosol mass concentration, over the region of study, to anthropogenic emissions of type i considered for grid cell j, calculated by GEOS-Chem adjoint. The third term, $\Delta E_{i,j}$, is the

Table 4.3: Change (2010-2050) in droplet number (cm^{-3}) and shortwave cloud albedo from emissions changes based on RCP4.5 scenario. Negative values correspond to a decrease from 2010 to 2050. Numbers in parentheses represent the percentile change (%) of droplet number and cloud albedo.

Region	ΔN_d from SO_2	ΔN_d from NH_3	ΔN_d from NO_x	ΔN_d from primary OC	Total ΔN_d	ΔA from Total ΔN_d ($\times 10^{-3}$)
Midwestern US August	-75.62 (-9.87)	0.34 (0.04)	-26.05 (-3.4)	0.18 (0.03)	-101.15 (-13.2)	4.08 (4.2)
Midwestern US February	2.47 (0.42)	4.64 (0.77)	-7.13 (-1.18)	0.15 (0.02)	0.12 (0.02)	-0.001 (-0.005)
Southeastern US August	-39.02 (-5.92)	0.22 (0.04)	-15.78 (-2.45)	0.24 (0.08)	-53.34 (-8.3)	3.47 (2.5)
Southeastern US February	-57.24 (-9.99)	4.22 (0.74)	-4.37 (-0.77)	0.67 (0.12)	-56.71 (-9.9)	5.12 (2.8)
Western US August	-35.03 (-8.12)	0.24 (0.06)	-18.17 (-4.22)	0.36 (0.09)	-52.59 (-12.2)	2.58 (4.0)
Western US February	-89.64 (-34.99)	1.28 (0.5)	-6.25 (-2.44)	1.08 (0.43)	-93.53 (-36.5)	17.13 (12.3)
Central Europe August	-229.29 (-37)	33.55 (5.42)	-314.99 (50.83)	0.70 (0.11)	-510.03 (-82.3)	31.86 (41.9)
Central Europe February	-9.16 (-1.28)	5.75 (0.8)	-73.54 (-10.24)	0.09 (0.01)	-76.86 (-10.7)	4.21 (3.2)

fractional change of emissions from Table 4.2.

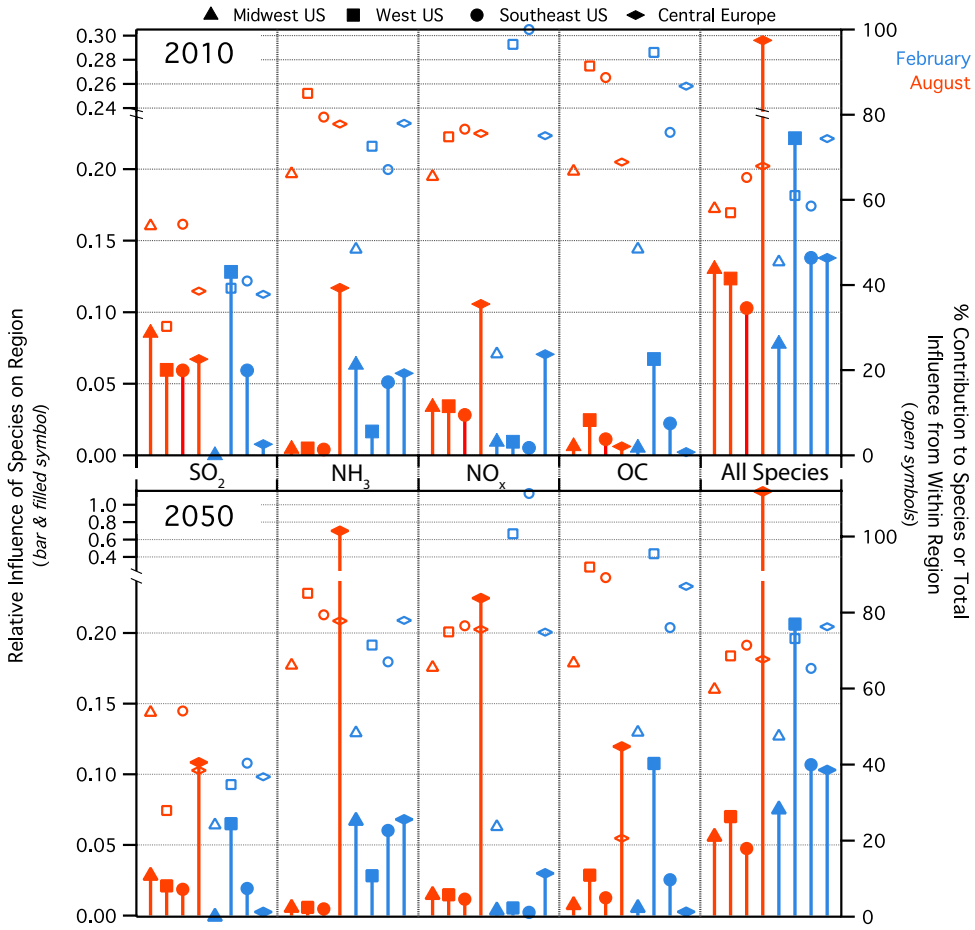

Figure 4.2: Total contribution of anthropogenic SO_2, NO_x, NH_3, and OC emissions to N_d over Midwest US, Southeast US, Western US, and Central Europe during August (orange) and February (blue) of 2010 (top panel) and 2050 (bottom panel). The fractional contribution of anthropogenic emissions from within each region on N_d is also shown (open symbols).

4.3 Results and Discussion

Figure 4.1 presents the fully normalized sensitivity of regional N_d to anthropogenic emissions from each grid cell. Figure 4.2 depicts the total worldwide contribution of anthropogenic emissions on as well as the fractional contribution of these anthropogenic emissions from within each region for present and future (based on RCP4.5 scenario) conditions. An analysis of each region and species follows.

4.3.1 Midwestern US

N_d is mostly sensitive to SO_2 ($R_{SO_2,tot} = 8.6 \times 10^{-2}$) and NO_x ($R_{NO_x,tot} = 3.4 \times 10^{-2}$) during August, and to NH_3 emissions during February ($R_{NH_3,tot} = 6.3 \times 10^{-2}$). Moreover, the high impact of NH_3 emissions on N_d during February together with the low impact of NO_x emissions, confirms that NH_3 is the limiting reactant in the formation of ammonium nitrate during the winter in this area. POA emissions have relatively low impact (approximately 0.5 $\times 10^{-2}$) on N_d, (Figure 4.2) owing to the lower magnitude of the primary organic emissions, compared to inorganic precursors over the midwestern US. The importance of NH_3 emissions in February and SO_2 emissions in August to aerosol formation over the midwestern US was also confirmed by *Tsimpidi et al.* (2007). *Henze et al.* (2009) also predicted similar trends for the sensitivity of inorganic aerosols to NH_3 and SO_2, however, the predicted effect on N_d is less pronounced as only a small fraction of aerosols is activated into droplets (<5%) over the polluted continental environments such as midwestern US. The lower impact of NO_x emissions on N_d during February is in accordance with *Tsimpidi et al.* (2008), who attributed this behavior to the increase of oxidants levels (after a NO_x emission reduction during winter) which promoted secondary aerosol production and compensated for the decrease of nitrates. In August, sulfate is the dominant inorganic aerosol component; therefore, aerosol concentrations are more sensitive to SO_2 emission changes from electricity generating units, followed by NO_x emissions, while NH_3 emissions have little impact (Figure 4.2). N_d is predicted to decrease by 75.62 cm^{-3} (9.87%) and 26.05 cm^{-3} (3.4%) due to SO_2 and NO_x emission changes by 2050, respectively (Table 4.3). During February, SO_2 emission decreases will increase the free NH_3 in the atmosphere, resulting in an increase in ammonium nitrate concentration. Therefore, sulfate is replaced by nitrate in the aerosol phase resulting in a minimal negative response of N_d to SO_2 emission changes ($R_{SO_2,tot} = -0.28 \times 10^{-2}$). The negative sensitivity arises from sufficiently low temperatures and high concentrations of HNO_3 at which the addition of one mole of SO_4^{-2} to the aerosol can actually reduce the total mass by displacing two moles of NO_3^- (*Moya*

et al., 2002; *West et al.*, 1998). Overall, during August, N_d and A are predicted to decrease in 2050 by approximately 100 cm^{-3} (13.2% change from 2010 levels) and approximately 4×10^3 (4.2%), respectively (Table 4.3). During February, ΔA and ΔN_d are predicted to be very low (Table 4.3). In this case, $\mathrm{R}_{\mathrm{SO_2,tot}}$ and $\mathrm{R}_{\mathrm{NO_x,tot}}$ are very small, while $\mathrm{R}_{\mathrm{NH_3,tot}}$ is high (and NH_3 emissions are expected to slightly increase in the future) (Figure 4.2a) so emissions changes have a small impact on N_d and A.

4.3.2 Southeastern US

N_d over the southeastern US is more sensitive to SO_2 electricity generation emissions during both seasons (5.9×10^{-2}) followed by NH_3 emissions from agriculture during February (5.1×10^{-2}) and NO_x emissions from electricity generating units during August (2.8×10^{-2}) (Figure 4.2). Consistent with *Capps et al.* (2012), the low amounts of nitric acid and ammonia not bound to sulfate leads to low levels of aerosol ammonium nitrate. This means that the aerosol cannot buffer SO_2 emissions shifts. N_d is predicted to decrease by 39 cm^{-3} (5.9%) and 57 cm^{-3} (10%) due to SO_2 emission changes by 2050 during August and February, respectively, and by 16 cm^{-3} (2.5%) due to NO_x emissions changes during August (Table 4.3). Anthropogenic POA emissions have an important impact during both February and August ($\mathrm{R}_{\mathrm{NH_3,tot}}$ $=2.2\times10^{-2}$ and 1.1×10^{-2}, respectively). Nevertheless, the predicted change attributed to POA emission changes by 2050 is negligible (less than 0.1%) since the latter is not expected to change significantly over US (Table 4.2). Overall, N_d and A are predicted to decrease in 2050 by 53.3 cm^{-3} (8.3%) and 3.5×10^3 (2.5%), respectively, during August and by 56.7 cm^{-3} (10%) and 5.1×10^3 (2.8%), respectively, during February (Table 4.3).

4.3.3 Western US

Anthropogenic SO_2 emissions are found to be the most important contributor to cloud droplet formation over the western US during both February and August ($\mathrm{R}_{\mathrm{SO_2,tot}}$ = 12.8×10^{-2} and 6×10^{-2}, respectively) (Figure 4.2). SO_2 emissions contribution to N_d over western US

is similar (during August) or even higher (during February) than the corresponding contribution to N_d over midwestern and southeastern US, despite the fact that typically SO_2 emissions are lower in western US. This can be explained by the high sensitivity of N_d to SO_2 from long range transport, especially from eastern China, resulting in a significant decrease of N_d in 2050 (52.6 cm^{-3} or 20.5%) due to changes on SO_2 emissions outside the western US. SO_2 emissions from shipping also contribute significantly to N_d. POA anthropogenic emissions also significantly impact the N_d over the West, especially during February ($\mathrm{R_{POA,tot}}$ = 6.7×10^{-2}). Similarly to southeastern US though, the predicted ΔN_d in 2050 due to POA emission changes is low (Table 4.3). Anthropogenic NH_3 emissions during August and anthropogenic NO_x emissions during February do not impact N_d over the West ($\mathrm{R_{NO_x,tot}} = 0.5\times10^{-2}$ and 1.7×10^{-2}, respectively) (Figure 4.2). Although highly concentrated centers of agricultural or urban activity emit significant amounts of NO_x and NH_3, respectively, pristine surrounding land causes dilution that limits the apparent impact on aerosol formation. Overall, N_d and A are predicted to decrease in 2050 by 52.6 cm^{-3} (12.2%) and 2.6×10^3 (4%), respectively, during August and by 93.5 cm^{-3} (36.5%) and 17.1×10^3 (12.3%), respectively, during February (Table 4.3). The strong effect of long-range transport of pollutants is mostly evident during February where the 57% of the predicted ΔN_d in 2050 is attributed to changes on anthropogenic emissions from outside the western US.

4.3.4 Central Europe

N_d is mostly sensitive to NH_3 ($\mathrm{R_{NH_3,tot}} = 11.7\times10^{-2}$) and NO_x ($\mathrm{R_{NO_x,tot}} = 10.6\times10^{-2}$) emissions during both August and February ($\mathrm{R_{NH_3,tot}} = 5.7\times10^{-2}$ and $\mathrm{R_{NO_x,tot}} = 7.1\times10^{-2}$). POA emissions impact N_d negligibly over Central Europe during both seasons ($\mathrm{R_{POA,tot}}$ as low as 0.2×10^{-2}). These conclusions are consistent with *Megaritis et al.* (2012) who found that NH_3 emissions had the most significant impact on aerosol formation over Europe, while the impact of POA emissions was the smallest. Ammonium nitrate is a major

aerosol component over Europe; therefore, emissions of its gas phase precursors (NH_3 and NO_x) exhibit the strongest impact on the inorganic aerosol population and N_d. However, according to RCP4.5 scenario, emissions of NH_3 over central Europe are not expected to change significantly by 2050 (0.06% increase). On the other hand, changes on NO_x emissions result to significant changes on ΔN_d (315 cm^{-3} or 50% and 74 cm^{-3} or 10% during August and February , respectively). SO_2 also contributes with a similar magnitude to N_d over central Europe during August ($\mathrm{R}_{\mathrm{SO_2,tot}}$ =6.7$\times 10^{-2}$). is predicted to decrease by 230 cm^{-3} (37%) due to SO_2 emission changes by 2050 and is strongly influenced by long-range transport of SO_2 from midwestern and northeastern US. The predicted ΔN_d due to changes of anthropogenic SO_2 emissions from outside the central Europe during August is 230 cm^{-3} (23%). During February, when sulfate levels are lower, N_d is less sensitive to SO_2 emissions ($\mathrm{R}_{\mathrm{SO_2,tot}}$ =0.8$\times 10^{-2}$), likely due to the limited H_2O_2 availability over Europe during this season (*Megaritis et al.*, 2012). Overall, ΔN_d decrease by 510 cm^{-3} (82%) and ΔA by 31.86 $\times 10^3$ (42%) during August. The large $\mathrm{R}_{\mathrm{SO_2,tot}}$ and $\mathrm{R}_{\mathrm{NO_x,tot}}$ predicted over Europe during this season (Figure 4.2), together with the large future reductions of these emissions (e.g., SO_2; Figure 4.1) results in the strong response of N_d and A to future emission changes, which is also influenced by the long-range impact of SO_2 emission reductions from the US (Figure 4.1). During February, ΔN_d and ΔA are predicted to be 77 cm^{-3} (10.7%) and 4.2 $\times 10^3$ (3.2%,), respectively, and are mostly attributed to NO_x emissions (Table 4.3).

4.4 Conclusions

In this work, the adjoints of the GEOS-Chem CTM and *Kumar et al.* (2009) droplet parameterization are used to determine the source region and relative impact of aerosol precursor emissions on N_d and albedo. Assessments are carried out for specific regions in February and August of 2008 and 2050 (using the RCP4.5 scenario). Among all species, the influence of sulfate emissions in August is most similar across regions, comprising at least

50% (20%) of the total influence in the US regions (Central Europe). For each region, the percent contribution from sulfate emissions within the region is the lowest of all the species tracked, which implicates long-range transport of significant sulfate burdens. Central Europe N_d in August is far more influenced by NH_3 and NO_x emissions than any region over the US due to the large contribution of ammonium nitrate aerosol to the regional aerosol. Nevertheless, for all four regions, 65-85% of the influence from NH_3 and NO_x emissions came from within the region in August. In February, the influence of NO_x emissions on Central Europe N_d remains much higher than on the N_d over US regions. However, the impact of NH_3 emissions on N_d, during February, is similar for Central Europe, midwestern, and southeastern US. Additionally, the maximum percent contribution of NO_x emissions within the region (nearly 100%) is attained in the western and southeastern US in February. The strongest internal influence is from POA in both August and February, owing to the shorter lifetime of the species. With the exception of the western US, the relative influence of POA on N_d is minor. The influence of different emissions mixes on N_d is most apparent from the distinction between the US and European response to NO_x and NH_3 emissions. Based on the RCP4.5 scenario and the 2008 adjoint, A in Central Europe during August and in western US during February is most strongly affected by future emission changes, owing to the effects of long-range transport of anthropogenic emissions (mainly SO_2) and NO_x reductions over Central Europe and the western US. The significant decrease of Nd over these regions results in higher anthropogenic emissions contributions to N_d in 2050 as the maximum supersaturation and droplet activation fractions are increased (*Karydis et al.*, 2012). In other regions and seasons, the anthropogenic emissions contributions to N_d are lower in 2050, mainly due to the significant decrease of SO_2 and NO_x emissions over the US and Europe (Figure 4.2). The above results reveal N_d sensitivities that would not have been predicted from earlier forward sensitivity analyses (i.e., the importance of SO_2 long-range transport on N_d over western US or the increasing contribution of SO_2 to N_d over central Europe in the future) and can be used from policy makers to effectively

design future emission control strategies.

Understanding relative impacts in coupled complex models is a challenge. Using the coupled adjoint sensitivity modeling framework developed here has allowed us to quantify the sensitivity of cloud droplet formation and cloud albedo to different aerosol precursor emissions and to unravel the importance of sectoral, spatial, and seasonal emissions.

CHAPTER V

THE SIGNIFICANCE OF INORGANIC THERMODYNAMICS IN A GLOBAL CHEMICAL TRANSPORT MODEL ADJOINT

In this chapter, we employ the recently developed comprehensive inorganic aerosol thermodynamic equilibrium model adjoint, ANISORROPIA, in the global chemical transport model adjoint GEOS-Chem to investigate the influence of inorganic aerosol thermodynamics on aerosol concentrations as well as the sensitivity of aerosol concentrations to emissions. Historically, a simplified thermodynamic equilibrium model representing the SO_4^{2-}-HSO_4^--NH_4^+-NO_3^--H_2O aerosol system was used in GEOS-Chem and then supplanted by ISORROPIA; similarly, the GEOS-Chem adjoint has been using the simplified representation in the absence of an adjoint for ISORROPIA. Now, employing ANISORROPIA in the GEOS-Chem adjoint framework elucidates the influence of inorganic aerosol thermodynamic treatments on aerosol burden as well as sensitivities of aerosol species with respect to emissions. The investigation demonstrates that the treatment selected can alter the concentration of sulfate, nitrate, and ammonium aerosol as well as the influence of emissions sources on this portion of the aerosol burden non-negligibly.

This chapter to be submitted for publication as part of: Capps, S. L., V. Karydis, D. K. Henze, A. G. Russell, and A. Nenes, Investigating responsiveness of cloud droplet concentrations to aerosol precursor emissions with different thermodynamic treatments, at various activation heights, and over multiple time scales.

5.1 Introduction

When aerosols act as sites for droplet formation, they enable emissions of aerosol precursors to shape cloud radiative properties as the number and size of droplets shifts. Often termed the indirect effect of aerosols on climate, this pathway for emissions to influence the radiative balance of the earth has proven challenging to assess in global climate models (GCMs). This effect must be diagnosed through careful establishment of the connection between cloud droplet number concentration and emissions from various sectors and locations. This extremely complex ambient process is challenging to represent accurately and sufficiently precisely in models. Some elements of this transformation are not yet well enough understood for advanced sensitivity analysis techniques to provide insight (e.g., sub-grid scale convective activity). However, in other respects, modeling efforts have matured enough to allow adjoint-based sensitivity analysis to make advances.

In particular, more than three decades of study of the SO_4^{2-}-HSO_4^--NH_4^+-NO_3^--H_2O aerosol system have led to models that can provide fairly robust comparisons between modeled and measured concentrations when emission rates of the aerosol precursors well-represented but still have room for improvement (*Stelson et al.*, 1978; *Appel et al.*, 2008; *Zhang et al.*, 2012a). Additionally, cloud droplet activation parameterizations have largely, though not entirely, converged on a similar representation of the activation process (*Ghan et al.*, 2011). Thus, it has become reasonable to invest development efforts in creating augmented sensitivity analysis tools for these systems to gain the most insight possible through these mathematical representations of physical processes.

To that end, the adjoint of GEOS-Chem was developed (*Henze et al.*, 2007). Initially, the inorganic aerosol thermodynamic module RPMARES (*Park et al.*, 2004), which was an adaptation of MARS (*Binkowski and Roselle*, 2003) for GEOS-Chem, was used. Here, we demonstrate the integration of the GEOS-Chem adjoint and ANISORROPIA , the adjoint of ISORROPIA, which is a more comprehensive and more widely adopted thermodynamic

treatment of inorganic aerosol (*Capps et al.*, 2012). Different results are expected RPMARES treats activity coefficients with the temperature-independent activity coefficients based on the Pitzer model for binary coefficients whereas ISORROPIA determines activity coefficients by the Kusik-Meissner (K-M) method which includes temperature dependence. K-M compares well with experimental results as does Pitzer but also continues to produce physically reasonable results at higher ionic strengths (i.e., greater than 30 molar) (*Harvie et al.*, 1984; *Cohen et al.*, 1987; *Kim et al.*, 1993b). Additionally, ISORROPIA considers the presence of other ions in the partitioning process, treating the whole Na^+-SO_4^{2-}-HSO_4^--NH_4^+-NO_3^--Cl^--H_2O aerosol system rather than only SO_4^{2-}-HSO_4^--NH_4^+-NO_3^--H_2O. The replacement of RPMARES with ANISORROPIA in the GEOS-Chem adjoint framework makes it commensurate with the treatment in the forward model.

With this integrated framework designed for probing the importance of thousands to millions of factors on an outcome of interest (i.e., aerosol mass concentration), we investigate questions that have been inaccessible previously due to the computational cost of the brute force approach. Specifically, we assess the influence of the inorganic thermodynamic equilibrium calculations on the sensitivity of the fine mode aerosol population with respect to emissions sources as well as relevant precursor gas and aerosol species concentrations.

5.2 Methods

To investigate the role of the inorganic aerosol equilibrium thermodynamics in concentrations and sensitivities with respect to emissions of the SO_4^{2-}-HSO_4^--NH_4^+-NO_3^--H_2O aerosol system, the GEOS-Chem adjoint (v.33) framework was developed to differ only in this respect. The models were executed for 13-day episodes in a selected month of each season of 2008 (February, May, August, November). Initial conditions for each simulation were developed with a year of spin up with the model configured with the appropriate aerosol thermodynamic treatment. If started from the same initial condition, the sensitivities would reflect not only the different processes but also the change in state due to a

switch of the thermodynamic module. This approach prevents misrepresentation of the sensitivities differences. Modeled concentrations are compared for these episodes.

Then, the sensitivity of the global burden of aerosol species that would reside in the fine mode with respect to emissions was calculated. In GEOS-Chem, the fine mode aerosol concentration is approximated as the sum of sulfate and nitrate not bound to sea salt; ammonium; and hydrophilic and hydrophobic primary organic aerosol. To assess sensitivity in the adjoint system, the model is executed to the end of the episode, and an infinitesimally small perturbation is propagated backward through the model to emissions to evaluate the contribution of emissions from the whole episode to the average fine mode aerosol concentration during the last day. The result is the sensitivity of the aerosol concentration on the last day of the episode with respect to emissions throughout the nearly two week period.

5.3 Results

The influence of the inorganic aerosol thermodynamic module on the concentration of gaseous precursors and aerosol of the SO_4^{2-}-HSO_4^--NH_4^+-NO_3^--H_2O system is shown to be non-negligible for each species. First, the differences in wintertime (Northern hemisphere) nitrate can be as large as 10 $\mu g\, m^{-3}$, or approximately 25% in areas with high aerosol burdens (Figure 5.1). Wintertime nitrate is likely to be the most significantly impacted by the introduction of the Kusik-Meissner method in exchange for the Pitzer model because of the introduction of temperature-dependence in activity coefficient calculations (*Kim et al.*, 1993b).

Further concentration comparisons can be examined in May, a more temperate month for both hemispheres (Figure 5.2). The concentration of ammonia gas, a neutralizing precursor necessary for formation of ammonium sulfate or ammonium nitrate aerosol, significantly decreases over east and south Asia with the use of ISORROPIA, suggesting that more of the reduced nitrogen resides in the aerosol phase. Some increase is evident in the NH_4^+ concentration changes over east Asia, but the south Asia effect may be too smeared

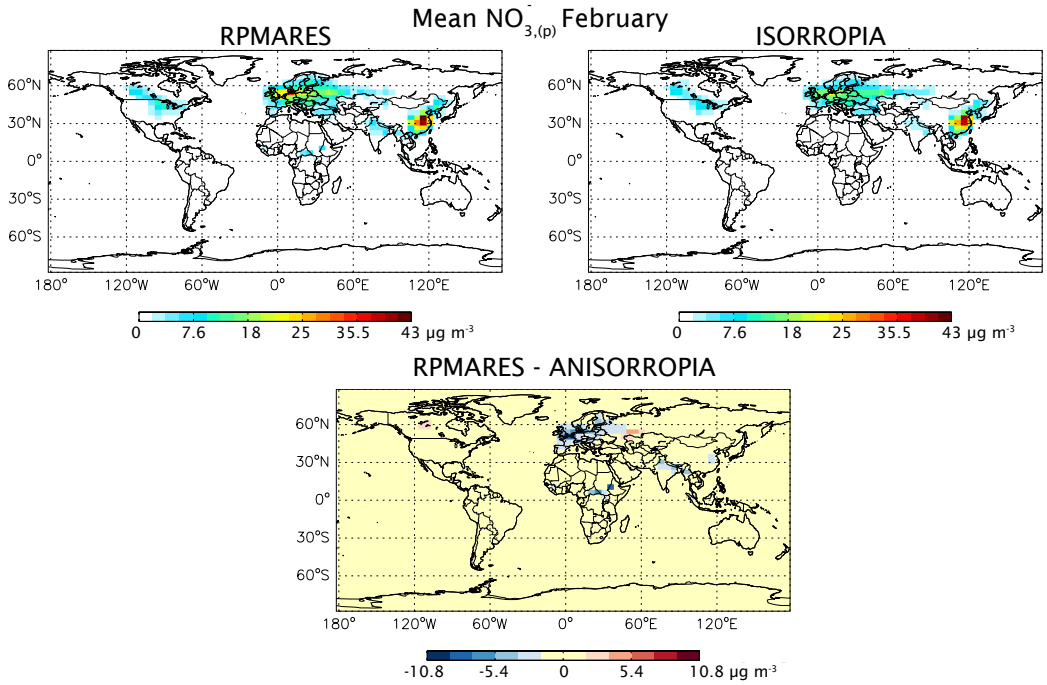

Figure 5.1: Mean concentrations of NO_3^- in $\mu g\ m^{-3}$ from February 1-13, 2008 (top row) with RPMARES (left) and ISORROPIA (right). The difference between the two model results with negatives representing a decrease from RPMARES being replaced with ISORROPIA (bottom).

to be evident with this color scale. The large magnitude is necessary, however, in order to see the significant effect of thermodynamics on the NH_4^+-NO_3^- aerosol over western Europe. The decrease in nitrate concentration leads to an approximately equal decrease in ammonium in this location given the one-to-one charge balance. Finally, the alteration in sulfate concentrations over Europe is comparatively small, but it is nonetheless significant due to the lower initial concentration. Given the decrease in both sulfate and nitrate aerosol, a slight increase in ammonia concentration over western Europe is evident. Given these significant changes in aerosol species and precursor gas concentrations, the effect of thermodynamics on sensitivities is also of interest.

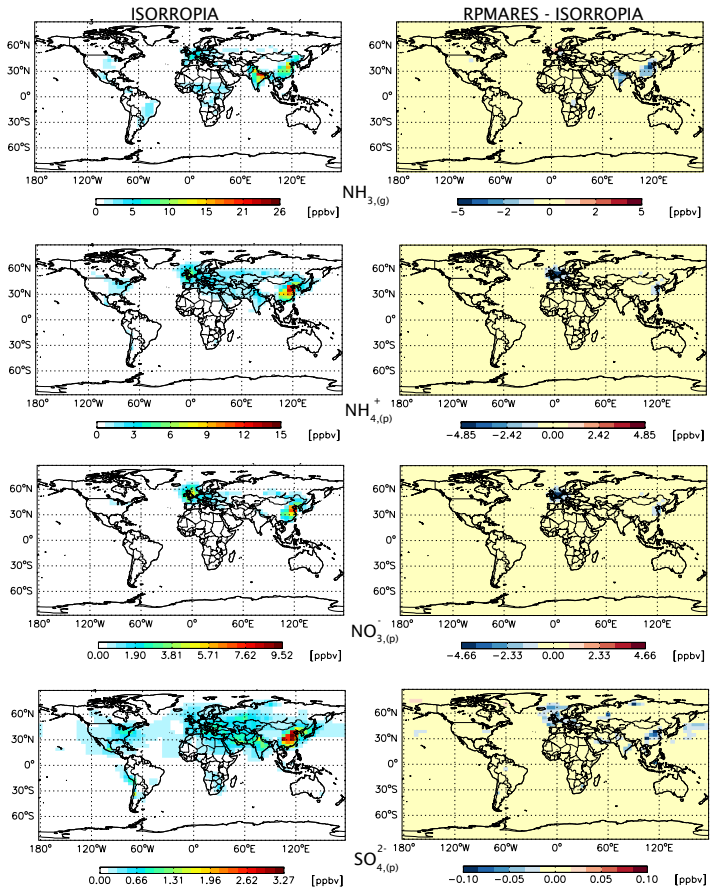

Figure 5.2: Mean concentrations of aerosol or precursor gas species simulated using ISORROPIA during May 1-13, 2008 (left panel) with the difference (right panel) between the two model results with negatives representing a decrease from RPMARES being replaced with ISORROPIA. From top to bottom, the concentrations are of ammonia gas, ammonium aerosol, nitrate aerosol, and sulfate aerosol. Aerosol mass is shown in ppb rather than in μg m^{-3} in order to facilitate consideration of charge balancing.

Again, we start with the wintertime influence of oxidized nitrogen by viewing the influence of anthropogenic NO_x emissions in the February episode. The global aerosol burden of species associated with the fine mode (as described above) are affected by incremental changes in anthropogenic NO_x emissions in each grid cell (Figure 5.3). Notably, the influence of anthropogenic NO_x emissions decreases significantly over western Europe and east Asia where the changes in the nitrate concentrations were also observed (Figure 5.1); however, the slight increases in sensitivity over eastern Europe and central northern America were not as apparent in the concentration comparison. This increase in information

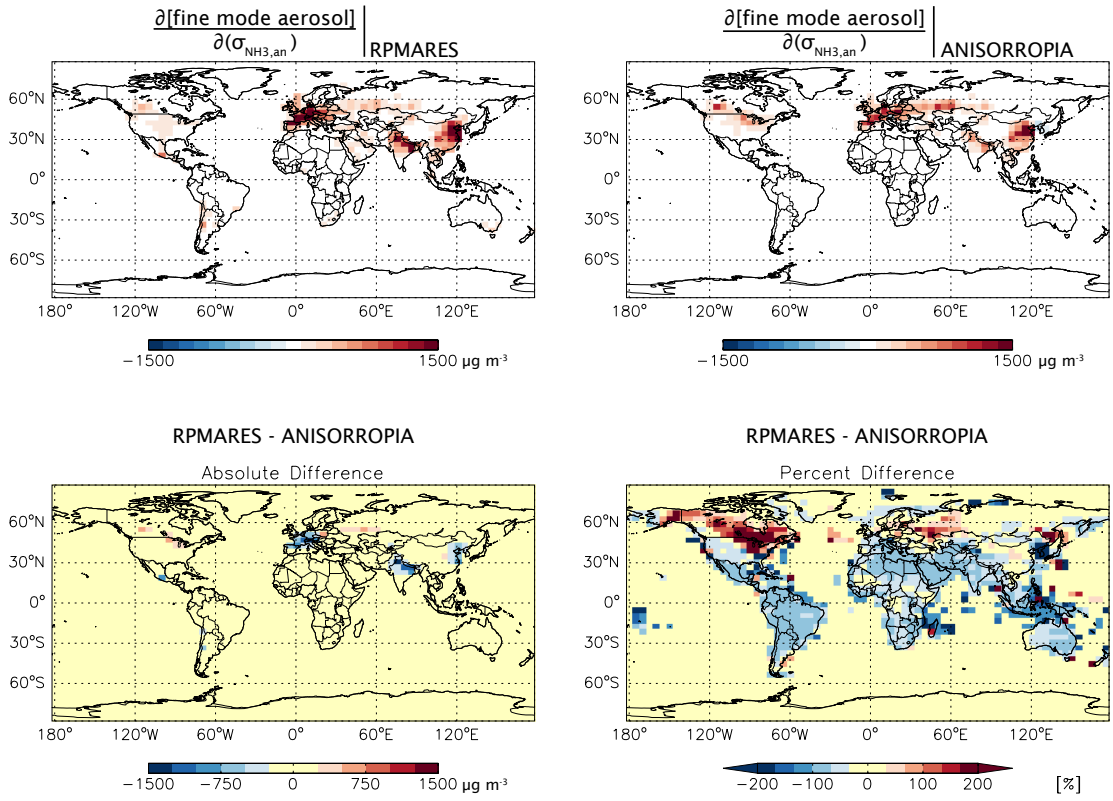

Figure 5.3: Sensitivity of the average fine mode aerosol concentration on February 13 (approximated as the sum of sulfate and nitrate not bound to sea salt; ammonium; and hydrophilic and hydrophobic primary organic aerosol) with respect to anthropogenic emissions of NO_x throughout the episode (top panel). The unit of $\mu g\ m^{-3}$ indicates that for a unit change in emissions a specific grid cell, the global aerosol burden would change by this amount. The difference between the two model results with negatives representing a decrease from the adjoint of RPMARES being replaced with ANISORROPIA (bottom panel) in absolute (left) and percentage units (right).

demonstrates the utility of an adjoint in addition to a forward model for sensitivity analysis. Furthermore, the percentage changes show that the impact of anthropogenic NO_x emissions on global aerosol burden in the wintertime would be quite different assessed with RPMARES than with ANISORROPIA (Figure 5.3, bottom right).

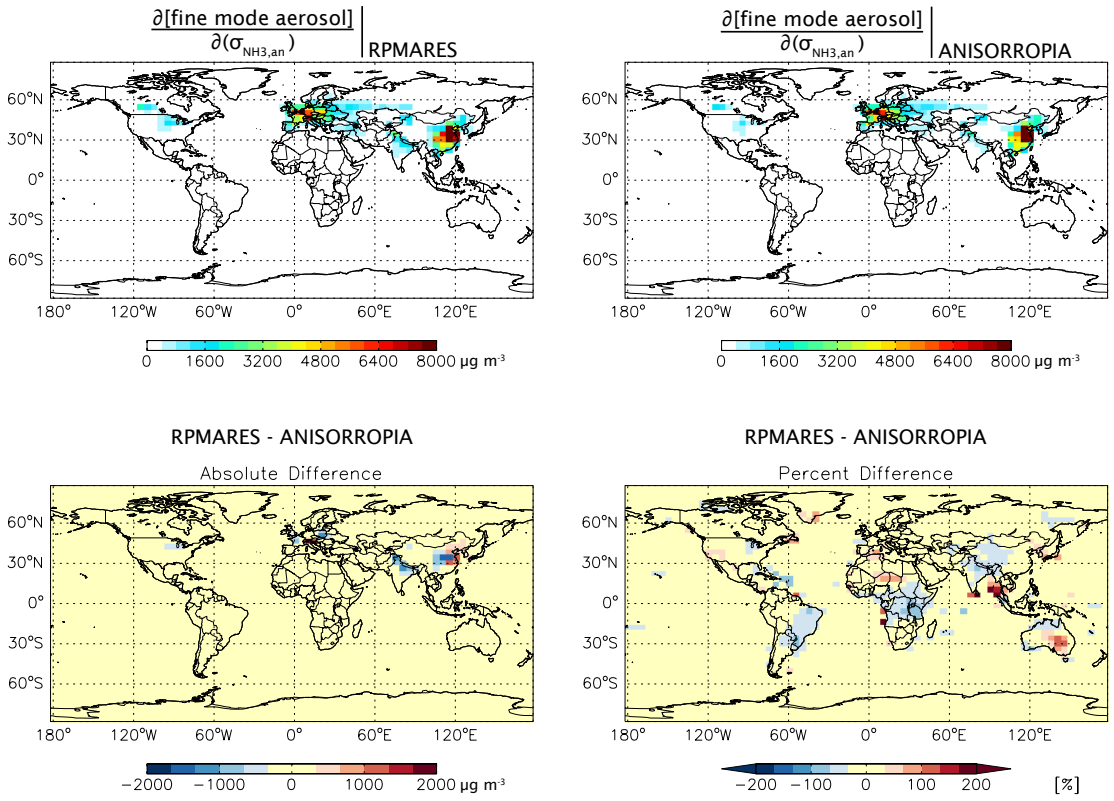

Figure 5.4: Same as Figure 5.3 except this figure is for anthropogenic emissions of NH_3.

Assessing the influence of anthropogenic NH_3 emissions in same February episode shows that this sensitivity changes less but still appreciably with exchange of thermodynamic adjoints (Figure 5.4). The primary effect is to moderate the largest sensitivities (i.e., east Asia, western Europe) (Figure 5.4, bottom left). This shift occurs with the broadening of the footprint, which leads to the small increases in sensitivity beside areas of greatest decrease. Finally, the fact that ANISORROPIA takes into account the concentration of sodium and chloride in the aerosol in order to determine partitioning of sulfate, nitrate, and ammonium may explain some of the higher magnitude, percent changes along the coasts especially in the southern hemisphere (Figure 5.4, bottom right).

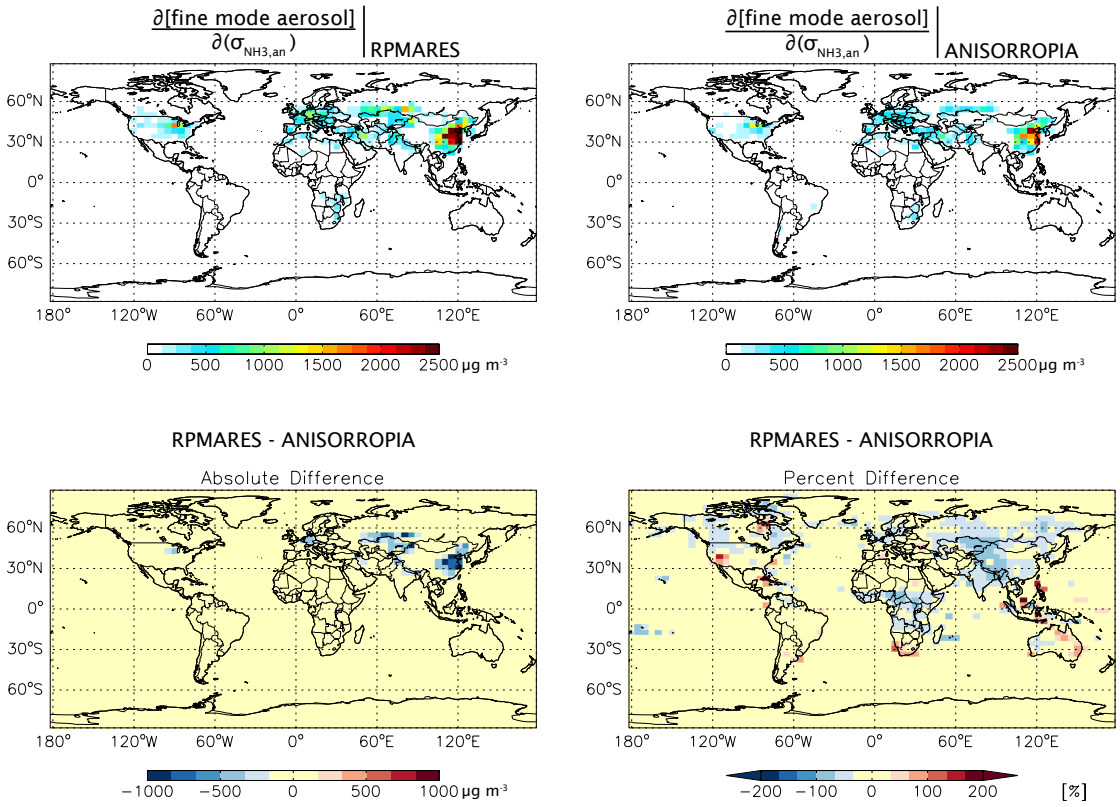

Figure 5.5: Same as Figure 5.4 except this figure is for August 1-13, 2008.

Finally, comparing the sensitivities for anthropogenic NH_3 emissions for the August episode, similar moderation of the largest influences are apparent (Figure 5.5, top row). One difference, however, is that neighboring increases are not observed (Figure 5.5, bottom left). Percent increases in the smaller sensitivities are evident in coastal locations (Figure 5.5, bottom right) reflecting the consideration of sea salt in thermodynamic partitioning of the inorganic species.

5.4 Conclusions

The recently integrated GEOS-Chem adjoint and ANISORROPIA models were used to assess the role of inorganic aerosol thermodynamic equilibrium in predicting aerosol and precursor gas concentrations for the SO_4^{2-}-HSO_4^--NH_4^+-NO_3^--H_2O system and, more uniquely, the sensitivity of fine mode aerosol with respect to emissions. These results indicate that

the differences between RPMARES and ISORROPIA, which seem small computationally, manifest non-negligibly in a global chemical transport model adjoint framework. Given that the forward GEOS-Chem model employs ISORROPIA, this result motivates the adjoint of GEOS-Chem to do likewise.

CHAPTER VI

FUTURE DIRECTIONS

As mentioned in Chapter 1, the development of adjoint-based modeling tools is the primary challenge for this advanced sensitivity analysis technique; thus, the directions that could be taken after this work has been accomplished seem quite expansive. To focus this discussion, I will address one inverse modeling opportunity that is in progress; comment on the status of a regional chemical transport model adjoint currently under development; and suggest an initiative in which the cloud droplet activation adjoint may serve well.

6.1 Inverse Modeling with Ammonia Observations

The GEOS-Chem adjoint is uniquely suited for conducting inverse modeling with satellite observations, which are often on the same scale and have GEOS-Chem-based a priori profiles. Dense observation fields, such as those from the Tropospheric Emissions Spectrometer (TES), are useful in a data assimilation framework for constraining a large number of model parameters. Although a variety of assimilation methods are viable, the adjoint of a model allows efficient minimization of the differences between observations and modeled concentrations by adjustment of many parameters (approximately 10^6) simultaneously. In this technique, the gradients required to obtain the Bayesian maximum a posterior estimate is obtained for the precise conditions at which the model produces output by which the cost function value is determined. During the CalNex field campaign in April - July 2010, TES performed high resolution retrievals of ammonia (NH_3) gas over the U.S., generally, and the Central Valley of California, specifically.

Efforts are currently underway to model this episode at 0.5 degree by 0.666 degree resolution over the continental U.S. and to optimize emissions from various sectors throughout the domain. The inclusion of ANISORROPIA in this investigation is key to its success.

Ammonia emissions are widely understood to be inaccurate over the Central Valley, so this presents a unique opportunity to assimilate satellite observations to optimize emissions parameters and then to assess the quality of the changes with in situ observations of ammonia and inorganic aerosol species.

6.2 Regional CTM Aerosol Adjoint

Although the global CTM aerosol adjoint is tremendously useful, it lacks population dynamics and secondary organic aerosol formation, which are tremendously influential on a regional scale to the concentration of aerosol. The development efforts for an adjoint of the aerosol aspect of the Community Multiscale Air Quality model commenced in 2008 led by Amir Hakami (U. of Carleton), Armistead Russell, Athanasios Nenes, and Daven Henze (U. of Colorado) with the prospects of being the first of its kind. ANISORROPIA will become an integral part of this regional adjoint framework. Currently, the entire adjoint model has been developed in a modular sense by a team as large as fifteen at times; integration of these modules is the final step in the development work. Limited release of the code for testing by beta users should occur in the first half of 2013. With the first adjoint of a regional air quality model including aerosols, opportunities to better understand the nitrogen cycle, depositional processes, and health effects of specific emissions abound.

6.3 Cloud Activation Adjoint in Coupled Framework

Historical model executions that incorporate observations are termed reanalyses and serve the community by providing a benchmark for model evaluation. A significant uncertainty in the reanalysis modeling framework is the absence of aerosol-cloud interactions due to a dearth of assimilation tools capable of representing them. The advent of a coupled chemistry-climate model fully equipped with an adjoint would provide an unprecedented opportunity to assimilate observations of clouds that indirectly contain information about the aerosol burden. Certainly, this is a long-term goal given the scale of such a model and

the need for development of additional adjoint components for a coupled system. Nevertheless, the aim of reducing uncertainty in the radiative forcing of aerosol through cloud interactions predicted by climate models may only be possible if a reanalysis product of this quality were available.

REFERENCES

(2002), *SPECIATE v3.2 Introduction and User's Guide*.

(2003), REQUIREMENTS FOR PREPARATION, ADOPTION, AND SUBMITTAL OF IMPLEMENTATION PLANS, *ecfr.gov*, *2*.

(2005a), Revisions to the CA state implementation plan and revision to the definition of volatile organic compounds (VOC) - Removal of VOC exemptions for CA's aerosol coating products reactivity-based regulation , *Federal Register*, (70), 53,930–53,935.

(2005b), Approval and promulgation of state implementation plans; Texas; Highly reactive volatile organic comopoud emissions cap and trade program for the Houston/Galveston/Brazoria ozone nonattainment area, *Federal Register*, (70), 54,046–54,051.

(2008), *Sparse Matrix Operator Kernel Emissions Modeling System (SMOKE) User's Manual*, Chapel Hill, NC, v2.5 ed.

ACKER, J. G., and G. LEPTOUKH (2007), Online analysis enhances use of NASA Earth science data, *Eos Trans. AGU*, *88*(2), 14–.

AGENCY, U. E. P. (2008), National Ambient Air Quality Standards for Ozone; Final Rule, *Federal Register*.

AMUNDSON, N., A. CABOUSSAT, J. HE, A. MARTYNENKO, V. SAVARIN, J. SEINFELD, and K. YOO (2006), A new inorganic atmospheric aerosol phase equilibrium model (UHAERO), *Atmos. Chem. Phys.*, *6*, 975–992.

ANSARI, A., and S. PANDIS (1998), Response of inorganic PM to precursor concentrations, *Environ. Sci. Technol.*, *32*(18), 2706–2714.

ANSARI, A., and S. PANDIS (1999a), An analysis of four models predicting the partitioning of semivolatile inorganic aerosol components, *Aerosol Sc. & Tech.*, *31*, 129–153.

ANSARI, A., and S. PANDIS (1999b), Prediction of multicomponent inorganic atmospheric aerosol behavior, *Atmos. Environ.*, *33*, 745–757.

APPEL, W. K., P. V. BHAVE, A. B. GILLILAND, G. SARWAR, and S. J. ROSELLE (2008), Evaluation of the community multiscale air quality (CMAQ) model version 4.5: Sensitivities impacting model performance; Part II—particulate matter, *Atmos. Environ.*, *42*(24), 6057–6066.

ARUNACHALAM, S., R. MATHUR, A. HOLLAND, M. R. LEE, D. OLERUD, and H. JEFFRIES (2003), Investigation of VOC Reactivity Assessment with Comprehensive Air Quality Modeling, *Tech. rep.*

AVERY, R. J. (2006), Reactivity-based VOC control for solvent products: More efficient ozone reduction strategies, *Environ. Sci. Technol.*, *40*(16), 4845–4850.

BARNARD, W. R., and E. SABO (2008), Documentation of the Base G2 and Best & Final 2002 Base Year, 2009 and 2018 Emission Inventories for VISTAS, *Tech. rep.*

BARTHOLOMEW-BIGGS, M. (1998), Using Forward Accumulation for Automatic Differentiation of Implicitly-Defined Functions, *Comp. Optim. App.*, *9*(1), 65–84.

BERGIN, M., A. RUSSELL, and J. MILFORD (1995), Quantification of individual VOC reactivity using a chemically detailed, 3-dimensional photochemical model, *Environ. Sci. Technol.*, *29*(12), 3029–3037.

BESSAGNET, B., and L. ROUÏL (2006), Ambient ozone simulations in response to VOC emission control scenarios, p. 36.

BESSAGNET, B., A. HODZIC, R. VAUTARD, M. BEEKMANN, S. CHEINET, C. HONORÉ, C. LIOUSSE, and L. ROUIL (2004), Aerosol modeling with CHIMERE—preliminary evaluation at the continental scale, *Atmos. Environ.*, *38*, 2803–2817.

BEY, I., D. JACOB, R. YANTOSCA, J. LOGAN, B. FIELD, A. FIORE, Q. LI, H. LIU, L. MICKLEY, and M. SCHULTZ (2001), Global modeling of tropospheric chemistry with assimilated meteorology- Model description and evaluation, *J. Geophys. Res.*, *106*(23), 073–23,095.

BINKOWSKI, F., and S. ROSELLE (2003), Models-3 Community Multiscale Air Quality (CMAQ) model aerosol component - 1. Model description, *J. Geophys. Res.*, *108*(D6), 4183.

BOUWMAN, A. F., D. S. LEE, W. A. H. ASMAN, F. J. DENTENER, K. W. VAN DER HOEK, and J. G. J. OLIVIER (1997), A global high-resolution emission inventory for ammonia, *Global Biogeochem. Cycles*, *11*(4), 561.

BYUN, D., and K. SCHERE (2006), Review of the Governing Equations, Computational Algorithms, and Other Components of the Models-3 Community Multiscale Air Quality (CMAQ) Modeling System, *Appl. Mechan. Rev.*, *59*, 51.

CALIFORNIA AIR RESOURCES BOARD (2001), Final Regulation Order for Reducing the Ozone Formed from Aerosol Coating Product Emissions.

CALIFORNIA AIR RESOURCES BOARD (2007), The California Low-Emission Vehicle Regulations.

CALIFORNIA AIR RESOURCES BOARD (2009), Updated Informative Digest Adoption of amendments to the regulation for reducing volatile organic compound emissions from aerosol coating products and tables of maximum incremental reactivity (MIR) values, and adoptiono f amendments to ARB Test Method 310, "Determinations of volatile organic compounds in consumer products", pp. 1–4.

CAPALDO, K., C. PILINIS, and S. PANDIS (2000), A computationally efficient hybrid approach for dynamic gas/aerosol transfer in air quality models, *Atmos. Environ.*, *21*(34), 3617–3627.

CAPPS, S., D. HENZE, A. HAKAMI, A. RUSSELL, and A. NENES (2012), ANISORROPIA: the adjoint of the aerosol thermodynamic model ISORROPIA, *Atmos. Chem. Phys.*, *12*, 527–543.

CARMICHAEL, G., Y. TANG, G. KURATA, I. UNO, D. STREETS, J.-H. WOO, H. HUANG, J. YIENGER, B. LEFER, R. SHETTER, D. BLAKE, E. ATLAS, A. FRIED, E. APEL, F. EISELE, C. CANTRELL, M. AVERY, J. BARRICK, G. SACHSE, W. BRUNE, S. SANDHOLM, Y. KONDO, H. SINGH, R. TALBOT, A. BANDY, D. THORTON, A. CLARKE, and B. HEIKES (2003), Regional-scale chemical transport modeling in support of the analysis of observations obtained during the TRACE-P experiment, *J. Geophys. Res.*, *108*(D21), 8823.

CARTER, W. (1994), Development of ozone reactivity scales for volatile organic compounds, *J. Air Waste Manag. Assoc.*, *44*(7), 881–899.

CARTER, W. (2000a), Implementation of the SAPRC-99 chemical mechanism into the Models-3 framework, *Report to the U.S. EPA*.

CARTER, W. (2008), Personal Communication.

CARTER, W., and R. ATKINSON (1989), COMPUTER MODELING STUDY OF INCREMENTAL HYDROCARBON REACTIVITY, *Environ. Sci. Technol.*, *23*(7), 864–880.

CARTER, W., G. TONNESEN, and G. YARWOOD (2003), Investigation of VOC reactivity effects using existing regional air quality models, *Report to the American Chemistry Council, Contract SC-20.0-UCR-VOC-RRWG*.

CARTER, W. P. L. (2000b), Documentation of the SAPRC-99 chemical mechanism for VOC reactivity assessment , *Tech. Rep. 00-AP-RT17-001-FR*, Riverside, California.

CARTER, W. P. L. (2005), Calculation of Reactivity Scales Using Regional Models, *Tech. rep.*, Riverside, California.

CARTER, W. P. L. (2010), Development of the SAPRC-07 chemical mechanism and updated ozone reactivity scales.

CHAI, T., G. R. CARMICHAEL, A. SANDU, Y. TANG, and D. N. DAESCU (2006), Chemical data assimilation of Transport and Chemical Evolution over the Pacific (TRACE-P) aircraft measurements, *J. Geophys. Res.*, *111*(D2).

CHUANG, C. C. J. E. P. K. E. T. A. S. G., and J. J. WALTON (1997), An assessment of the radiative effects of anthropogenic sulfate, *J. Geophys. Res.*, *102*, 3761–3778.

CLARKE, L., J. EDMONDS, H. JACOBY, H. PITCHER, J. REILLY, and R. RICHELS (2007), Scenarios of Greenhouse Gas Emissions and Atmospheric Concentrations, *Tech. Rep. Rep. 2.1A*.

CLEGG, S., P. BRIMBLECOMBE, and A. WEXLER (1998), Thermodynamic Model of the System H^+ NH_4^+ Na^+ SO_4^2- NO_3^- Cl^- H_2O at 298.15 K, *J. Phys. Chem. A*, *102*(12), 2155–2171.

COHAN, D. S., A. HAKAMI, Y. HU, and A. G. RUSSELL (2005), Nonlinear Response of Ozone to Emissions: Source Apportionment and Sensitivity Analysis, *Environ. Sci. Technol.*, *39*(17), 6739–6748.

COHEN, M. D., R. C. FLAGAN, and J. H. SEINFELD (1987), Studies of concentrated electrolyte solutions using the electrodynamic balance. 2. Water activities for mixed-electrolyte solutions, *J. Phys. Chem.*, *91*(17), 4575–4582.

CROES, B., J. HOLMES, and A. LLOYD (1992), REACTIVITY-BASED HYDROCARBON CONTROLS - SCIENTIFIC ISSUES AND POTENTIAL REGULATORY APPLICATIONS, *J. Air Waste Manag. Assoc.*, *42*(5), 657–661.

D'ALMEIDA, G. A. (1987), On the Variability of Desert Aerosol Radiative Characteristics, *J. Geophys. Res.*, *92*(D3), 3017–3026.

DASSIOS, K., and S. PANDIS (1999), The mass accommodation coefficient of ammonium nitrate aerosol, *Atmos. Environ.*, *33*(18), 2993–3003.

DAY, D. A., P. WOOLDRIDGE, M. DILLON, J. THORNTON, and R. COHEN (2002), A thermal dissociation laser-induced fluorescence instrument for in situ detection of NO_2, peroxy nitrates, alkyl nitrates, and HNO_3, *J. Geophys. Res.*, *107*(D6).

DIMITRIADES, B. (1996), Scientific basis for the VOC reactivity issues raised by Section 183(e) of the Clean Air Act Amendments of 1990, *J. Air Waste Manag. Assoc.*, *46*(10), 963–970.

DUBOVIK, O., T. LAPYONOK, Y. J. KAUFMAN, M. CHIN, P. GINOUX, R. A. KAHN, and A. SINYUK (2008), Retrieving global aerosol sources from satellites using inverse modeling, *Atmos. Chem. Phys.*, *8*, 209.

DUNKER, A., G. YARWOOD, J. ORTMANN, and G. WILSON (2002), Comparison of source apportionment and source sensitivity of ozone in a three-dimensional air quality model, *Environ. Sci. Technol.*, *36*(13), 2953–2964.

DUNKER, A. M. (1984), The decoupled direct method for calculating sensitivity coefficients in chemical kinetics, *J. Chem. Phys.*, *81*(5), 2385.

EDGERTON, E., B. HARTSELL, R. SAYLOR, J. JANSEN, D. HANSEN, and G. HIDY (2006), The Southeastern Aerosol Research and Characterization Study, Part 3: Continuous measurements of fine particulate matter mass and composition, *J. Air Waste Manag. Assoc.*, *56*(9), 1325–1341.

ELBERN, H., H. SCHMIDT, and A. EBEL (1997), Variational data assimilation for tropospheric chemistry modeling, *J. Geophys. Res.*, *102*(D13), 15,967–15,985.

ELBERN, H., H. SCHMIDT, O. TALAGRAND, and A. EBEL (2000), 4D-variational data assimilation with an adjoint air quality model for emission analysis, *Environ. Model. Soft.*, *15*(6-7), 539–548.

EMERY, C., E. TAI, and G. YARWOOD (2001), Enhanced Meteorological Modeling and Performance Evaluation for Two Texas Ozone Episodes, *Final Report for The Texas Natural Resource Conservation Commission*, pp. 1–235.

ENVIRON (1997), *User's Guide to the Comprehensive Air Quality Model with Extensions (CAMx)*, Novato, California, USA, 1.10 ed.

ENVIRON (2010), *Comprehensive Air Quality Model with extensions User's Guide*, Novato, California, USA, 5.3 ed.

FARMER, D., P. WOOLDRIDGE, and R. COHEN (2006), Application of thermal dissociation-laser induced fluorescence (TD-LIF) to measurement of HNO_3, alkyl nitrates, peroxy nitrates, and NO_2 using eddy covariance, *Atmos. Chem. Phys.*, *6*, 3471–3486.

FINLAYSON-PITTS, B., and J. PITTS (1997), Tropospheric air pollution: Ozone, airborne toxics, polycyclic aromatic hydrocarbons, and particles, *Science*, *276*(5315), 1045–1052.

FISHER, M., and D. J. LARY (1995), Lagrangian four-dimensional variational data assimilation of chemical species, *Q J Roy Meteor Soc*, *121*(527), 1681–1704.

FORSTER, P., V. RAMASWAMY, P. ARTAXO, T. BERNTSEN, R. BETTS, D. FAHEY, J. HAYWOOD, J. LEAN, D. LOWE, and G. MYHRE (2007), Climate Change 2007: The Physical Science Basis. Contribution of Working Group I, in *Fourth Assessment Report of the Intergovernmental Panel on Climate Change*, Cambridge University Press.

FOUNTOUKIS, C., and A. NENES (2007), ISORROPIA II: a computationally efficient thermodynamic equilibrium model for K^+-Ca^{+2}-Mg^{+2}-NH_4^+-Na^+-SO_4^{2-}-NO_3^--Cl^--H_2O aerosols, *Atmos. Chem. Phys.*, *7*, 4639–4659.

FOUNTOUKIS, C., A. NENES, A. SULLIVAN, R. WEBER, T. VAN REKEN, M. FISCHER, E. MATIAS, M. MOYA, D. FARMER, and R. COHEN (2009), Thermodynamic characterization of Mexico City aerosol during MILAGRO 2006, *Atmos. Chem. Phys.*, *9*, 2141–2156.

FUGLESTVEDT, J., T. BERNTSEN, G. MYHRE, K. RYPDAL, and R. B. SKEIE (2008), Climate forcing from the transport sectors, *Proceedings of the National Academy of Sciences*, *105*(2), 454–458.

GAYDOS, T., R. PINDER, B. KOO, K. FAHEY, G. YARWOOD, and S. PANDIS (2007), Development and application of a three-dimensional aerosol chemical transport model, PMCAMx, *Atmos. Environ.*, *41*, 2594–2611.

GHAN, S. J., H. ABDUL-RAZZAK, A. NENES, Y. MING, X. LIU, M. OVCHINNIKOV, B. SHIPWAY, N. MESKHIDZE, J. XU, and X. SHI (2011), Droplet nucleation: Physically-based parameterizations and comparative evaluation, *J. Adv. Model. Earth Syst.*, *3*(10), M10,001.

GILES, M., and N. PIERCE (2000), An introduction to the adjoint approach to design, *Flow Turb. and Comb.*, *65*(3), 393–415.

GRELL, G., J. DUDHIA, and D. STAUFFER (1995), A Description of the Fifth-generation Penn State/NCAR Mesoscale Model: MM5, *NCAR Technical Note*.

GRIEWANK, A. (1989), On automatic differentiation, in *Mathematical Programming: Recent Developments and Applications*, edited by M. Iri and K. Tanabe, pp. 83–108, Kluwer Academic Publishers, Argonne National Laboratory.

GUENTHER, A., T. KARL, P. HARLEY, C. WIEDINMYER, P. I. PALMER, and C. GERON (2006), Estimates of global terrestrial isoprene emissions using MEGAN (Model of Emissions of Gases and Aerosols from Nature), *Atmos. Chem. Phys.*, *6*(11), 3181–3210.

HAKAMI, A., M. ARHAMI, and A. RUSSELL (2004a), Further Analysis of VOC Reactivity Metrics and Scales, *Report to Environmental Protection Agency*, (Final Report), 1–49.

HAKAMI, A., R. HARLEY, J. MILFORD, M. ODMAN, and A. RUSSELL (2004b), Regional, three-dimensional assessment of the ozone formation potential of organic compounds, *Atmos. Environ.*, *38*(1), 121–134.

HAKAMI, A., M. BERGIN, and A. RUSSELL (2004c), Ozone Formation Potential of Organic Compounds in the Eastern United States: A Comparison of Episodes, Inventories, and Domains, *Environ. Sci. Technol.*, *38*, 6748–6759.

HAKAMI, A., D. HENZE, J. SEINFELD, T. CHAI, Y. TANG, G. CARMICHAEL, and A. SANDU (2005), Adjoint inverse modeling of black carbon during the Asian Pacific Regional Aerosol Characterization Experiment, *J. Geophys. Res.*

HAKAMI, A., J. SEINFELD, T. CHAI, Y. TANG, G. CARMICHAEL, and A. SANDU (2006), Adjoint sensitivity analysis of ozone nonattainment over the continental United States, *Environ. Sci. Technol.*, *40*(12), 3855–3864.

HAKAMI, A., D. HENZE, J. SEINFELD, K. SINGH, and A. SANDU (2007), The Adjoint of CMAQ, *Environ. Sci. Technol.*

HALES, J. M. (2007), The Reactivity Research Working Group - A Chronological Overview and Evaluation, *Report to North American Research Strategy for Tropospheric Ozone*, p. 99.

HANNA, S., and R. YANG (2001), Evaluations of mesoscale models' simulations of near-surface winds, temperature gradients, and mixing depths, *J. Appl. Meteor.*, *40*(6), 1095–1104.

HANSEN, D. A., E. S. EDGERTON, B. E. HARTSELL, J. J. JANSEN, N. KANDASAMY, G. M. HIDY, and C. L. BLANCHARD (2003), The Southeastern Aerosol Research and Characterization Study: Part 1-Overview, *J. Air Waste Manag. Assoc.*, *53*(12), 1460–1471.

HARVIE, C. E., N. MØLLER, and J. H. WEARE (1984), The prediction of mineral solubilities in natural waters: The Na-K-Mg-Ca-H-Cl-$SO_4 - OH - HCO_3 - CO_3 - CO_2 - H_2Osystemtohighionicstrengthsat25\,^{\circ}$C, *Geochimica et Cosmochimica Acta*, *48*(4), 723–751.

HASCOËT, L., and V. PASCUAL (2004), TAPENADE 2.1 User's Guide, *Tech. rep.*, INRIA Sophia Antipolis, Sophia Antipolis Cedex.

HEINTZENBERG, J. (1989), Fine particles in the global troposphere: A review, *Tellus B*, *41B*(2), 149–160.

HENZE, D., J. SEINFELD, W. LIAO, A. SANDU, and G. CARMICHAEL (2004), Inverse modeling of aerosol dynamics: Condensational growth, *J. Geophys. Res.*, *109*, D14.

HENZE, D., A. HAKAMI, and J. SEINFELD (2007), Development of the adjoint of GEOS-Chem, *Atmos. Chem. Phys.*, *7*, 2413–2433.

HENZE, D., J. SEINFELD, and D. SHINDELL (2009), Inverse modeling and mapping US air quality influences of inorganic $PM_{2.5}$ precursor emissions using the adjoint of GEOS-Chem, *Atmos. Chem. Phys.*, *9*, 5877–5903.

HEUBERT, B., T. BATES, P. RUSSELL, G. SHI, Y. KIM, K. KAWAMURA, G. CARMICHAEL, and T. NAKAJIMA (2003), An overview of ACE-Asia: Strategies for quantifying the relationships between Asian aerosols and their climatic impacts, *J. Geophys. Res.*, *108*(D23), 8633.

HU, Y., M. TALAT ODMAN, and A. RUSSELL (2006), Mass conservation in the Community Multiscale Air Quality model, *Atmos. Environ.*, *40*(7), 1199–1204.

JACOBSON, M. (1999), Studying the effects of calcium and magnesium on size-distributed nitrate and ammonium with EQUISOLV II, *Atmos. Environ.*

JACOBSON, M., and A. TABAZADEH (1996), Simulating equilibrium within aerosols and nonequilibrium between gases and aerosols, *J. Geophys. Res.*

JIMENEZ, J. L., M. R. CANAGARATNA, N. M. DONAHUE, A. S. H. PREVOT, Q. ZHANG, J. H. KROLL, P. F. DECARLO, J. D. ALLAN, H. COE, N. L. NG, A. C. AIKEN, K. S. DOCHERTY, I. M. ULBRICH, A. P. GRIESHOP, A. L. ROBINSON, J. DUPLISSY, J. D. SMITH, K. R. WILSON, V. A. LANZ, C. HUEGLIN, Y. L. SUN, J. TIAN, A. LAAKSONEN, T. RAATIKAINEN, J. RAUTIAINEN, P. VAATTOVAARA, M. EHN, M. KULMALA, J. M. TOMLINSON, D. R. COLLINS, M. J. CUBISON, J. DUNLEA, J. A. HUFFMAN, T. B. ONASCH, M. R. ALFARRA, P. I. WILLIAMS, K. BOWER, Y. KONDO, J. SCHNEIDER, F. DREWNICK, S. BORRMANN, S. WEIMER, K. DEMERJIAN, D. SALCEDO, L. COTTRELL, R. GRIFFIN, A. TAKAMI, T. MIYOSHI, S. HATAKEYAMA,

A. SHIMONO, J. Y. SUN, Y. M. ZHANG, K. DZEPINA, J. R. KIMMEL, D. SUEPER, J. T. JAYNE, S. C. HERNDON, A. M. TRIMBORN, L. R. WILLIAMS, E. C. WOOD, A. M. MIDDLEBROOK, C. E. KOLB, U. BALTENSPERGER, and D. R. WORSNOP (2009), Evolution of Organic Aerosols in the Atmosphere, *Science*, *326*(5959), 1525–1529.

KAMINSKI, T., M. HEIMANN, and R. GIERING (1999), A coarse grid three-dimensional global inverse model of the atmospheric transport. 2. Inversion of the transport of CO_2 in the 1980s, *J. Geophys. Res.*, *104*(D15), 18,555–18,581.

KARYDIS, V. A., P. KUMAR, D. BARAHONA, I. N. SOKOLIK, and A. NENES (2011), On the effect of dust particles on global cloud condensation nuclei and cloud droplet number, *J. Geophys. Res.*, *116*(D23), D23,204.

KARYDIS, V. A., S. L. CAPPS, A. G. RUSSELL, and A. NENES (2012), Adjoint sensitivity of global cloud droplet number to aerosol and dynamical parameters, *Atmos. Chem. Phys.*, *12*(19), 9041–9055.

KELLY, J., P. BHAVE, C. NOLTE, U. SHANKAR, and K. FOLEY (2010), Simulating emission and chemical evolution of coarse sea-salt particles in the Community Multiscale Air Quality (CMAQ) model, *Geosci. Model Dev.*, *3*, 257–273.

KIM, Y. P., J. H. SEINFELD, and P. SAXENA (1993a), Atmospheric Gas-Aerosol Equilibrium I. Thermodynamic Model, *Aerosol Sci. Tech.*, *19*(2), 157–181.

KIM, Y. P., J. H. SEINFELD, and P. SAXENA (1993b), Atmospheric Gas-Aerosol Equilibrium II. Analysis of Common Approximations and Activity Coefficient Calculation Methods, *Aerosol Sci. Tech.*, *19*(2), 182–198.

KLIMONT, Z., and D. STREETS (2007), Emission inventories and projections for assessing hemispheric or intercontinental transport, in *Air Pollution Studies No. 16*, edited by T. Keating and A. Zuber, United Nations, Economic Commission for Europe, New York and Geneva.

KOCH, D., T. C. BOND, D. STREETS, and N. UNGER (2007), Linking future aerosol radiative forcing to shifts in source activities, *Geophys. Res. Lett.*, *34*(5).

KOO, B., A. DUNKER, and G. YARWOOD (2007), Implementing the Decoupled Direct Method for Sensitivity Analysis in a Particulate Matter Air Quality Model, *Environ. Sci. Technol.*, *41*(10), 2847–2854.

KOPACZ, M., D. J. JACOB, D. K. HENZE, C. L. HEALD, D. G. STREETS, and Q. ZHANG (2009), Comparison of adjoint and analytical Bayesian inversion methods for constraining Asian sources of carbon monoxide using satellite (MOPITT) measurements of CO columns, *J. Geophys. Res.*, *114*(D4), 1–10.

KOPACZ, M., D. L. MAUZERALL, J. WANG, E. M. LEIBENSPERGER, D. K. HENZE, and K. SINGH (2011), Origin and radiative forcing of black carbon transported to the Himalayas and Tibetan Plateau, *Atmos. Chem. Phys.*, *11*(6), 2837–2852.

KUHNS, H., E. M. KNIPPING, and J. M. VUKOVICH (2005), Development of a United States–Mexico Emissions Inventory for the Big Bend Regional Aerosol and Visibility Observational (BRAVO) Study, *Journal of the Air & Waste Management Association*, *55*(5), 677–692.

KUKKONEN, J., T. BALK, D. M. SCHULTZ, A. BAKLANOV, T. KLEIN, A. I. MIRANDA, A. MONTEIRO, M. HIRTL, V. TARVAINEN, M. BOY, V. H. PEUCH, A. POUPKOU, I. KIOUTSIOUKIS, S. FINARDI, M. SOFIEV, R. SOKHI, K. LEHTINEN, K. KARATZAS, R. SAN JOSÉ, M. ASTITHA, G. KALLOS, M. SCHAAP, E. REIMER, H. JAKOBS, and K. EBEN (2011), Operational, regional-scale, chemical weather forecasting models in Europe, *Atmos. Chem. Phys. Discuss.*, *11*(2), 5985–6162.

KUMAR, P., I. N. SOKOLIK, and A. NENES (2009), Parameterization of cloud droplet formation for global and regional models: including adsorption activation from insoluble CCN, *Atmos. Chem. Phys.*, *9*(7), 2517–2532.

LAMB, R., W. CHEN, and J. SEINFELD (1975), Numerico-Empirical Analyses of Atmospheric Diffusion Theories, *J. Atmosph. Sci.*, *32*(9), 1794–1807.

LANCE, S., A. NENES, and T. A. RISSMAN (2004), Chemical and dynamical effects on cloud droplet number: Implications for estimates of the aerosol indirect effect, *J. Geophys. Res.*, *109*(D22), D22,208–.

LANTOINE, G., R. RUSSELL, and T. DARGENT (2010), Using Multicomplex Variables for Automatic Computation of High-Order Derivatives, in *American Astronautical Society/American Institute of Aeronautics and Astronautics Space Flight Mechanics Meeting*, pp. 1–18, San Diego, California.

LEIBENSPERGER, E. M., L. MICKLEY, D. J. JACOB, W.-T. CHEN, J. H. SEINFELD, A. NENES, P. J. ADAMS, D. G. STREETS, N. KUMAR, and D. RIND (2012a), Climatic effects of 1950-2050 changes in US anthropogenic aerosols - Part 1: Aerosol trends and radiative forcing, *Atmos. Chem. Phys.*, *12*(7), 3333–3348.

LEIBENSPERGER, E. M., L. MICKLEY, D. J. JACOB, W.-T. CHEN, J. H. SEINFELD, A. NENES, P. J. ADAMS, D. G. STREETS, N. KUMAR, and D. RIND (2012b), Climatic effects of 1950-2050 changes in US anthropogenic aerosols - Part 2: Climate response, *Atmos. Chem. Phys.*, *12*(7), 3349–3362.

LUECKEN, D., and M. MEBUST (2008), Technical Challenges Involved in Implementation of VOC Reactivity-Based Control of Ozone, *Environ. Sci. Technol.*, (42), 1615–1622.

LYNESS, J., and C. MOLER (1967), Numerical differentiation of analytic functions, *SIAM J. Num. Anal.*, pp. 202–210.

MALM, W. C., J. F. SISLER, D. HUFFMAN, R. A. ELDRED, and T. A. CAHILL (1994), Spatial and seasonal trends in particle concentration and optical extinction in the United States, *J. Geophys. Res.*, *99*(D1), 1347–1370.

MANKTELOW, P. T., K. S. CARSLAW, G. W. MANN, and D. V. SPRACKLEN (2009), Variable CCN formation potential of regional sulfur emissions, *Atmos. Chem. Phys.*, *9*(10), 3253–3259.

MARCHUK, G. (1974), *Numerical solution of the problem of dynamics of atmosphere and ocean*, Gidrometeoizdat, Leningrad.

MARTIEN, P., and R. HARLEY (2006), Adjoint sensitivity analysis for a three-dimensional photochemical model: Application to Southern California, *Environ. Sci. Technol.*, *40*(13), 4200–4210.

MARTIEN, P. T., R. A. HARLEY, and D. G. CACUCI (2006), Adjoint Sensitivity Analysis for a Three-Dimensional Photochemical Model: Implementation and Method Comparison, *Environ. Sci. Technol.*, *40*(8), 2663–2670.

MCBRIDE, S. J., M. A. ORAVETZ, and A. G. RUSSELL (1997), Environmental Policy Analysis, Peer Reviewed: Cost–Benefit and Uncertainty Issues in Using Organic Reactivity to Regulate Urban Ozone, *Environ. Sci. Technol.*, *31*(5), 238A–244A.

MEGARITIS, A. G., C. FOUNTOUKIS, P. E. CHARALAMPIDIS, C. PILINIS, and S. N. PANDIS (2012), Response of fine particulate matter concentrations to changes of emissions and temperature in Europe, *Atmos. Chem. Phys. Discuss*, *12*(4), 8771–8822.

MENDOZA-DOMINGUEZ, A., and A. RUSSELL (2001), Estimation of emission adjustments from the application of four-dimensional data assimilation to photochemical air quality modeling, *Atmos. Environ.*, *35*, 2879–2894.

MENG, Z., and J. SEINFELD (1996), Time scales to achieve atmospheric gas-aerosol equilibrium for volatile species, *Atmos. Environ.*

MENUT, L., R. VAUTARD, M. BEEKMANN, and C. HONORÉ (2000), Sensitivity of photochemical pollution using the adjoint of a simplified chemistry-transport model, *J. Geophys. Res.*, *105*, 15.

METZGER, S., and J. LELIEVELD (2007), Reformulating atmospheric aerosol thermodynamics and hygroscopic growth into fog, haze and clouds, *Atmos. Chem. Phys.*, *7*(12), 3163–3193.

METZGER, S., N. MIHALOPOULOS, and J. LELIEVELD (2006), Importance of mineral cations and organics in gas-aerosol partitioning of reactive nitrogen compounds: case study based on MINOS results, *Atmos. Chem. Phys.*, *6*(9), 2549–2567.

MOLINA, L. T., S. MADRONICH, J. S. GAFFNEY, E. APEL, B. DE FOY, J. FAST, R. FERRARE, S. HERNDON, J. L. JIMENEZ, B. LAMB, A. R. OSORNIO-VARGAS, P. RUSSELL, J. J. SCHAUER, P. S. STEVENS, R. VOLKAMER, and M. ZAVALA (2010), An overview of the MILAGRO 2006 Campaign: Mexico City emissions and their transport and transformation, *Atmos. Chem. Phys.*, *10*(18), 8697–8760.

MOORE, R. H., V. A. KARYDIS, S. L. CAPPS, T. L. LATHEM, and A. NENES (2012), Droplet number prediction uncertainties from CCN: an integrated assessment using observations and a global adjoint model, *Atmos. Chem. Phys. Discuss*, *12*(8), 20,483–20,517.

MOYA, M., A. ANSARI, and S. N. PANDIS (2001), Partitioning of nitrate and ammonium between the gas and particulate phases during the 1997 IMADA-AVER study, *Atmos. Environ.*, (35), 1791–1804.

MOYA, M., S. N. PANDIS, and M. Z. JACOBSON (2002), Is the size distribution of urban aerosols determined by thermodynamic equilibrium?, *Atmos. Environ.*, *36*(14), 2349–2365.

MULLER, J., and T. STAVRAKOU (2005), Inversion of CO and NO_x emissions using the adjoint of the IMAGES model, *Atmos. Chem. Phys.*, *5*, 1157–1186.

NAPELENOK, S., D. COHAN, Y. HU, and A. RUSSELL (2006), Decoupled direct 3D sensitivity analysis for particulate matter (DDM-3D/PM), *Atmos. Environ.*, *40*(32), 6112–6121.

NENES, A., S. PANDIS, and C. PILINIS (1998), ISORROPIA: A New Thermodynamic Equilibrium Model for Multiphase Multicomponent Inorganic Aerosols, *Aquat. Geochem.*, *4*(1), 123–152.

NENES, A., S. PANDIS, and C. PILINIS (1999), Continued development and testing of a new thermodynamic aerosol module for urban and regional air quality models, *Atmos. Environ.*, *33*(10), 1553–1560.

NEUMAN, J., J. NOWAK, C. BROCK, M. TRAINER, F. FEHSENFELD, J. HOLLOWAY, G. HÜBLER, P. HUDSON, D. MURPHY, and D. NICKS JR (2003), Variability in ammonium nitrate formation and nitric acid depletion with altitude and location over California, *J. Geophys. Res.*, *108*(D17), 4557.

NOWAK, J., L. HUEY, A. RUSSELL, D. TIAN, J. NEUMAN, D. ORSINI, S. SJOSTEDT, A. SULLIVAN, D. TANNER, R. WEBER, A. NENES, E. EDGERTON, and F. FEHSENFELD (2006), Analysis of urban gas phase ammonia measurements from the 2002 Atlanta Aerosol Nucleation and Real-Time Characterization Experiment (ANARChE), *J. Geophys. Res.*, *111*(D17308).

OLIVIER, J. G. J., and J. J. M. BERDOWSKI (2001), Global emissions sources and sinks, in *The Climate System*, edited by J. Berdowski, R. Guicherit, and B. J. Heij, pp. 33–78, A. A. Balkema Publishers/Swets & Zeitlinger Publishers, Lisse, The Netherlands.

ORSINI, D., Y. MA, A. SULLIVAN, B. SIERAU, K. BAUMANN, and R. WEBER (2003), Refinements to the particle-into-liquid sampler (PILS) for ground and airborne measurements of water soluble aerosol composition, *Atmos. Environ.*, *37*.

PARK, R. J., D. JACOB, B. FIELD, R. YANTOSCA, and M. CHIN (2004), Natural and transboundary pollution influences on sulfate-nitrate-ammonium aerosols in the United States: Implications for policy, *J. Geophys. Res.*, *109*(D15204).

PILINIS, C., K. CAPALDO, A. NENES, and S. PANDIS (2000), MADM-A new multicomponent aerosol dynamics model, *Aerosol Sci. Tech.*

PINDER, R. W., P. J. ADAMS, and S. N. PANDIS (2007), Ammonia Emission Controls as a Cost-Effective Strategy for Reducing Atmospheric Particulate Matter in the Eastern United States, *Environ. Sci. Technol.*, *41*(2), 380–386.

PLEIM, J., and A. XIU (1995), Development and testing of a surface flux and planetary boundary layer model for application in mesoscale models, *J. Appl. Meteor.*, *34*(1), 16–32.

PYE, H., H. LIAO, S. WU, L. MICKLEY, D. JACOB, D. HENZE, and J. SEINFELD (2009), Effect of changes in climate and emissions on future sulfate-nitrate-ammonium aerosol levels in the United States, *J. Geophys. Res.*, *114*(D01205), 1–18.

RADKE, L. F., D. A. HEGG, J. H. LYONS, C. A. BROCK, P. V. HOBBS, R. WEISS, and R. RASMUSSEN (), Airborne measurements on smokes from biomass burning, in *Aerosols and Climate*, edited by P. V. Hobbs and M. P. McCormick, pp. 411–422, A. Deepak, Hampton, VA.

RESLER, J., K. EBEN, P. JURUS, and J. LICZKI (2010), Inverse modeling of emissions and their time profiles, *Atmos. Poll. Res.*, pp. 288–295.

RUSSELL, A., J. MILFORD, M. BERGIN, S. MCBRIDE, L. MCNAIR, Y. YANG, W. STOCKWELL, and B. CROES (1995), Urban ozone control and atmospheric reactivity of organic gases, *Science*, *269*(5223), 491–495.

SANDU, A., D. DAESCU, G. CARMICHAEL, and T. CHAI (2005a), Adjoint sensitivity analysis of regional air quality models, *J Comput. Phys.*, *204*(1), 222–252.

SANDU, A., W. LIAO, G. CARMICHAEL, D. HENZE, and J. SEINFELD (2005b), Inverse Modeling of Aerosol Dynamics Using Adjoints: Theoretical and Numerical Considerations, *Aerosol Sci. Tech.*, *39*(8), 677–694.

SASAKI, Y. (1958), An objective analysis based on the variational method., *J. Met. Soc. Jap.*, *36*, 77–88.

SAXENA, P., A. BELLE HUDISCHEWSKYJ, C. SEIGNEUR, and J. SEINFELD (1986), A comparative study of equilibrium approaches to the chemical characterization of secondary aerosols, *Atmos. Environ.*, *20*(7), 1471–1483.

SCHAAP, M., R. M. A. TIMMERMANS, M. ROEMER, G. A. C. BOERSEN, P. J. H. BUILTJES, F. J. SAUTER, G. J. M. VELDERS, and J. P. BECK (2008), The LOTOS-EUROS model: description, validation and latest developments, *Int. J. of Environ. Pollution*, *32*(2), 270–290.

SCHMIDT, H., C. DEROGNAT, R. VAUTARD, and M. BEEKMANN (2001), A comparison of simulated and observed ozone mixing ratios for the summer of 1998 in Western Europe, *Atmos. Environ.*, *35*.

SEINFELD, J. H., and S. N. PANDIS (2006a), *Atmospheric chemistry and physics*, from air pollution to climate change, Wiley-Interscience.

SEINFELD, J. H., and S. N. PANDIS (2006b), *Atmospheric chemistry and physics: from air pollution to climate change*, 2nd ed., John Wiley, New York.

SEINFELD, J. H., G. R. CARMICHAEL, R. ARIMOTO, W. C. CONANT, F. J. BRECHTEL, T. S. BATES, T. A. CAHILL, A. D. CLARKE, S. J. DOHERTY, P. J. FLATAU, B. J. HUEBERT, J. KIM, K. M. MARKOWICZ, P. K. QUINN, L. M. RUSSELL, P. B. RUSSELL, A. SHIMIZU, Y. SHINOZUKA, C. H. SONG, Y. TANG, I. UNO, A. M. VOGELMANN, R. J. WEBER, J.-H. WOO, and X. Y. ZHANG (2004), ACE-ASIA: Regional Climatic and Atmospheric Chemical Effects of Asian Dust and Pollution, *Bull. Amer. Met. Soc.*, *85*(3), 367–380.

SEKIYAMA, T., T. TANAKA, A. SHIMIZU, and T. MIYOSHI (2010), Data assimilation of CALIPSO aerosol observations, *Atmos. Chem. Phys.*

SHINDELL, D., J. F. LAMARQUE, N. UNGER, D. KOCH, G. FALUVEGI, S. BAUER, M. AMMANN, J. COFALA, and H. TEICH (2008), Climate forcing and air quality change due to regional emissions reductions by economic sector, *Atmos. Chem. Phys.*, *8*(23), 7101–7113.

SHINDELL, D. T., G. FALUVEGI, D. M. KOCH, G. A. SCHMIDT, N. UNGER, and S. E. BAUER (2009), Improved Attribution of Climate Forcing to Emissions, *Science*, *326*(5953), 716–718.

SOLOMON, P. A., W. CHAMEIDES, R. WEBER, A. MIDDLEBROOK, C. S. KIANG, A. G. RUSSELL, A. BUTLER, B. TURPIN, D. MIKEL, R. SCHEFFE, E. COWLING, E. EDGERTON, J. ST JOHN, J. JANSEN, P. MCMURRY, S. HERING, and T. BAHADORI (2003), Overview of the 1999 Atlanta Supersite Project, *J. Geophys. Res.*, *108*(D7), 8413.

SQUIRE, W., and G. TRAPP (1998), Using complex variables to estimate derivatives of real functions, *SIAM Rev.*, *40*(1), 110–112.

STELSON, A. W., S. K. FRIEDLANDER, and J. H. SEINFELD (1978), A note on the equilibrium relationship between ammonia and nitric acid and particulate ammonium nitrate, *Atmos. Environ.*, *13*(3), 369–371.

STEVENS, B., and G. FEINGOLD (2009), Untangling aerosol effects on clouds and precipitation in a buffered system, *Nature*, *461*(7264), 607–613.

STREETS, D. G., T. C. BOND, G. R. CARMICHAEL, S. D. FERNANDES, Q. FU, D. HE, Z. KLIMONT, S. M. NELSON, N. Y. TSAI, M. Q. WANG, J. H. WOO, and K. F. YARBER (2003), An inventory of gaseous and primary aerosol emissions in Asia in the year 2000, *J. Geophys. Res.*, *108*(D21), 8809.

TALAGRAND, O. (1981), On the mathematics of data assimilation, *Tellus*, (33), 321.

TALAGRAND, O., and P. COURTIER (1987), Variational assimilation of meteorological observations with the adjoint vorticity equation. 1. Theory, *Q J Roy Meteor Soc*, *113*(478), 1311–1328.

TSIMPIDI, A. P., V. A. KARYDIS, and S. N. PANDIS (2007), Response of Inorganic Fine Particulate Matter to Emission Changes of Sulfur Dioxide and Ammonia: The Eastern United States as a Case Study, *Journal of the Air & Waste Management Association*, *57*(12), 1489–1498.

TSIMPIDI, A. P., V. A. KARYDIS, and S. N. PANDIS (2008), Response of fine particulate matter to emission changes of oxides of nitrogen and anthropogenic volatile organic compounds in the eastern United States, *Journal of the Air & Waste Management Association*, *58*(11), 1463–1473.

TURNER, A. J., D. K. HENZE, R. V. MARTIN, and A. HAKAMI (2012), The spatial extent of source influences on modeled column concentrations of short-lived species, *Geophys. Res. Lett.*, *39*(12), L12,806–.

TWOMEY, S. (1974), Pollution and the planetary albedo, *Atmos. Environ.*, *8*, 1251–1256.

TWOMEY, S. (1991), Aerosols, clouds and radiation, *Atmospheric Environment Part A General Topics*, *25*(11), 2435–2442.

UNO, I., K. YUMIMOTO, A. SHIMIZU, Y. HARA, N. SUGIMOTO, Z. WANG, Z. LIU, and D. M. WINKER (2008), 3D structure of Asian dust transport revealed by CALIPSO lidar and a 4DVAR dust model, *Geophys. Res. Lett.*, *35*(6), L06,803.

US ENVIRONMENTAL PROTECTION AGENCY (2004), Air Quality Criteria for Particulate Matter, *National Center for Environmental Assessment - RTP Office, Office of Research and Development*, *EPA/600/P-99/002aF*.

VAN DER WERF, G. R., J. T. RANDERSON, L. GIGLIO, G. J. COLLATZ, P. S. KASIBHATLA, and A. F. ARELLANO, JR. (2006), Interannual variability in global biomass burning emissions from 1997 to 2004, *Atmos. Chem. Phys.*, *6*(11), 3423–3441.

VAYENAS, D., S. TAKAHAMA, C. DAVIDSON, and S. PANDIS (2005), Simulation of the thermodynamics and removal processes in the sulfate-ammonia-nitric acid system during winter: Implications for PM2.5 control strategies, *J. Geophys. Res.*, *110*, –.

VOGEL, B., H. VOGEL, D. BÄUMER, M. BANGERT, K. LUNDGREN, R. RINKE, and T. STANELLE (2009), The comprehensive model system COSMO-ART- Radiative impact of aerosol on the state of the atmosphere on the regional scale, *Atmos. Environ.*, *9*, 8661–8680.

VUKIĆEVIĆ, T., and P. HESS (2000), Analysis of tropospheric transport in the Pacific Basin using the adjoint technique, *J. Geophys. Res.*, *105*(D6), 7213–7230.

WANG, L., J. MILFORD, and W. CARTER (2002), Uncertainty analysis of chamber-derived incremental reactivity estimates for n-butyl acetate and 2-butoxy ethanol, *Atmos. Environ.*, *36*(1), 115–135.

WANG, L., T. THOMPSON, E. C. MCDONALD-BULLER, A. WEBB, and D. T. ALLEN (2007), Photochemical modeling of emissions trading of highly reactive volatile organic compounds in Houston, Texas. 1. Reactivity based trading and potential for ozone hot spot formation, *Environ. Sci. Technol.*, *41*(7), 2095–2102.

WEST, J., C. PILINIS, A. NENES, and S. PANDIS (1998), Marginal direct climate forcing by atmospheric aerosols, *Atmos. Environ.*, *32*, 2531–2542.

WEST, J., A. ANSARI, and S. PANDIS (1999), Marginal PM2.5: Nonlinear aerosol mass response to sulfate reductions in the Eastern United States, *J. Air Waste Manag. Assoc.*, *49*(12), 1415–1424.

XIU, A., and J. PLEIM (2001), Development of a land surface model. Part I: Application in a mesoscale meteorological model, *J. Appl. Meteor.*, *40*(2), 192–209.

YANG, Y., J. WILKINSON, and A. RUSSELL (1997), Fast, direct sensitivity analysis of multidimensional photochemical models, *Environ. Sci. Technol.*, *31*(10), 2859–2868.

YUMIMOTO, K., I. UNO, N. SUGIMOTO, A. SHIMIZU, and S. SATAKE (2007), Adjoint inverse modeling of dust emission and transport over East Asia, *Geophys. Res. Lett.*, *34*(8).

YUMIMOTO, K., I. UNO, N. SUGIMOTO, A. SHIMIZU, Z. LIU, and D. WINKER (2008), Adjoint inversion modeling of Asian dust emission using lidar observations, *Atmos. Chem. Phys.*

ZALESKI, R. (2008), Personal communication.

ZAVERI, R., R. EASTER, and L. PETERS (2005), A computationally efficient multicomponent equilibrium solver for aerosols (MESA), *J. Geophys. Res.*, *110*(D24), D24,203.

ZHANG, L., E. CONSTANTINESCU, A. SANDU, Y. TANG, T. CHAI, G. CARMICHAEL, D. BYUN, and E. OLAGUER (2008), An adjoint sensitivity analysis and 4D-Var data assimilation study of Texas air quality, *Atmos. Environ.*, *42*(23), 5787–5804.

ZHANG, L., D. J. JACOB, E. M. KNIPPING, N. KUMAR, J. W. MUNGER, C. C. CAROUGE, A. VAN DONKELAAR, Y. X. WANG, and D. CHEN (2012a), Nitrogen deposition to the United States: distribution, sources, and processes, *Atmos. Chem. Phys.*, *12*(10), 4539–4554.

ZHANG, W., S. L. CAPPS, Y. HU, A. NENES, S. L. NAPELENOK, and A. G. RUSSELL (2012b), Development of the high-order decoupled direct method in three dimensions for particulate matter: enabling advanced sensitivity analysis in air quality models, *Geosci. Model Dev.*, *5*, 355–368.

VITA

Shannon Capps was born in Knoxville, Tennessee, USA, to Lee and Pat Capps with older brother Adam. She studied chemical engineering at Vanderbilt University and learned to conduct computer modeling research under the guidance of Clare McCabe. The opportunity to work with NOAA scientists, particularly Greg Frost, to address societally-relevant scientific questions in 2006 led to consideration of a career in policy-relevant atmospheric science. During her studies at Georgia Tech, Shannon enjoyed the opportunities to study the Bible with Fellowship of Christian Graduate Students, run with Runnin Wreck, and experience life with Atlanta Westside Presbyterian Church. She also appreciated training she received in teaching through Victor Breedveld and the Center for Enhancement of Teaching and Learning.

Advanced Sensitivity Analysis Techniques for Atmospheric Chemistry Models: Development and Application

Shannon L. Capps

103 Pages

Directed by Professor Athanasios Nenes

Trace gases and aerosols, or suspended liquid and solid material in the atmosphere, have significant climatological and societal impacts; consequently, accurate representation of their contribution to atmospheric composition is vital to predicting climate change and informing policy actions. Sensitivity analysis allows scientists and environmental decision makers alike to ascertain the role a specific component of the very complex system that is the atmosphere of the Earth. Anthropogenic and natural emissions of gases and aerosol are transported by winds and interact with sunlight, allowing significant transformation before these species reach the end of their atmospheric life on land or in water. The adjoint-based sensitivity method assesses the relative importance of each emissions source to selected results of interest, including aerosol and cloud droplet concentration. In this work, the adjoint of a comprehensive inorganic aerosol thermodynamic equilibrium model was produced to improve the representativeness of regional and global chemical transport modeling. Furthermore, a global chemical transport model adjoint equipped with the adjoint of a cloud droplet activation parameterization was used to explore the footprint of emissions contributing to current and potential future cloud droplet concentrations, which impact the radiative balance of the earth. In future work, these sensitivity relationships can be exploited in optimization frameworks for assimilation of observations of the system, such as satellite-based or in situ measurements of aerosol or precursor trace gas concentrations.